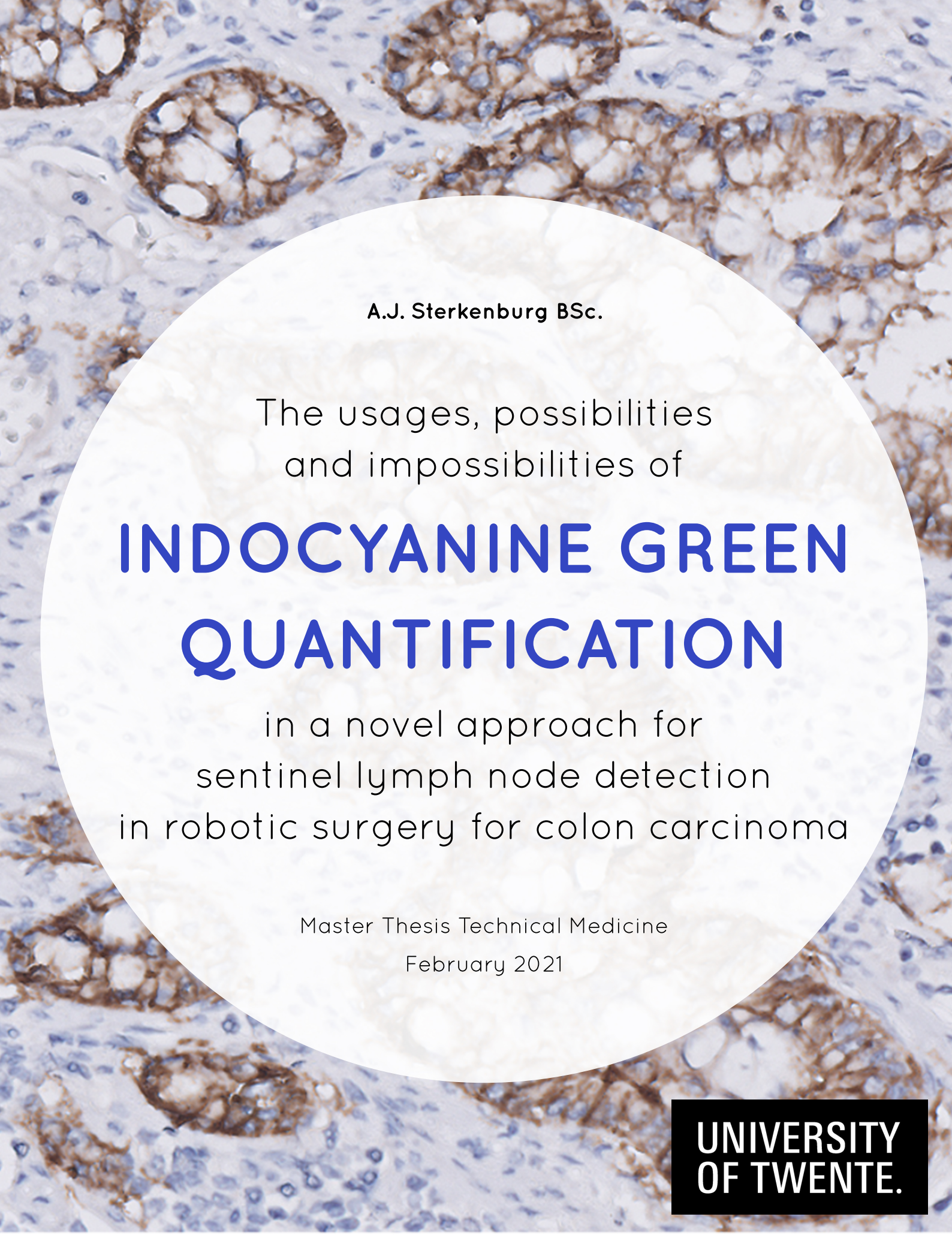

A.J. Sterkenburg BSc.

The usages, possibilities
and impossibilities of

INDOCYANINE GREEN QUANTIFICATION

in a novel approach for
sentinel lymph node detection
in robotic surgery for colon carcinoma

Master Thesis Technical Medicine
February 2021

UNIVERSITY OF TWENTE.

meander MEDISCH CENTRUM
OMIG
umcg
SURGICAL ROBOTICS LABORATORY

Graduation committee:

Chairman:
Prof. Dr. S. Misra
Surgical Robotics Laboratory
Faculty of Engineering and Technology
University of Twente, Enschede

Medical supervisor:
Prof. Dr. E.C.J. Consten
Department of Surgery
Meander Medical Center, Amersfoort
University Medical Center, Groningen

Process supervisor:
R.J. Haarman MSc
Technical Medicine
Faculty of Sience and Technology
University of Twente, Enschede

Medical supervisor:
Prof. Dr. W.B. Nagengast
Department of Gastroenterology
University Medical Center Groningen

External member:
T. Boers MSc
Multi-Modality Medical Imaging
Faculty of Engineering and Technology
University of Twente, Enschede

Daily technical supervisor:
C.M. Heunis MSc
Surgical Robotics Laboratory
Faculty of Engineering and Technology
University of Twente, Enschede

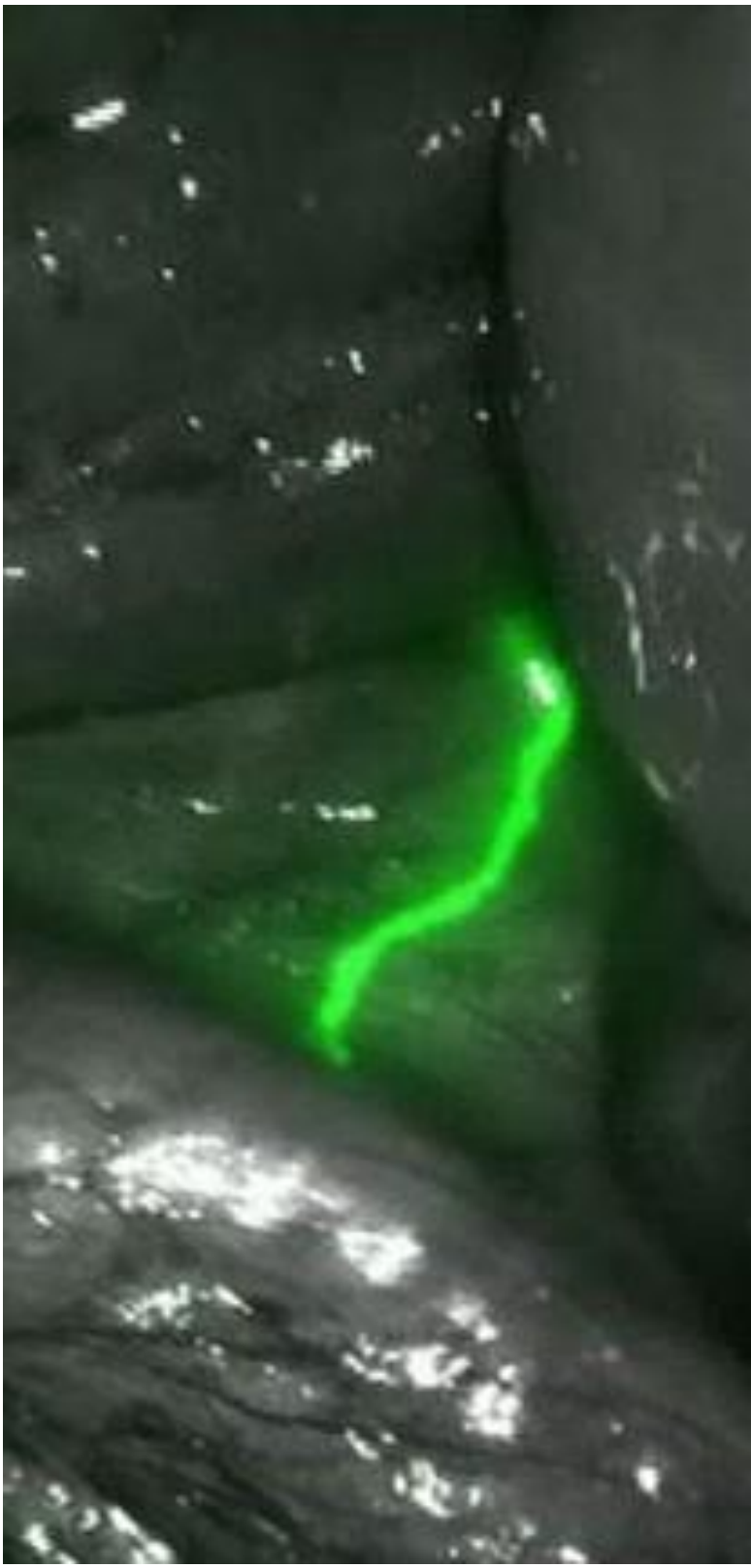

Abstract

Introduction & Background

Colon carcinoma (CC) is the cancer type with the second highest morbidity in the Netherlands and its prevalence will only rise due to screening programs and an ageing population. To prevent mortality due to understaging, a hemicolectomy is performed but this increases the postoperative mortality and morbidity risk. The sentinel lymph node (SLN) procedure can form a solution because it functions as a triage procedure and avoids surgery which is done to prevent micrometastases.
The research question in this master thesis is "What are the possibilities of using a specific near-infrared (NIR) tracer in detecting the sentinel lymph node and making a prognosis in early-stage colon cancer?" Three subgoals are used to provide an answer to this question:

a Evaluate a promising biomarker for the identification of tumour cells in lymph nodes.

b Set up an indocyanine green (ICG) quantification study in patients to explore the possibilities of quantifying the fluorescence intensity.

c Set up an ICG quantification phantom study to explore the different variables influencing the intensity on screen.

(a) A CD44v6 targeted biomarker

The usefulness of a CD44v6 targeted biomarker for the identification of early-stage CC cells was assessed. Tissue of patients treated for all stages of CC was included and stained using the CD44v6 targeted biomarker. 59 Slices of tissue of 21 different patients were included. The stained slices were scored on membrane staining using the H-score. The sensitivity and specificity were calculated, and appropriate statistical tests were used to define any significant differences in staining.
A sensitivity of 0.98 and a specificity of 1 was found. The Mann-Whitney test showed a significant difference between tumour tissue and tumour deposit, no other significant differences were found. The two-tailed Wilcoxon test showed a non-significant difference within a patient.
The high sensitivity and specificity of this biomarker, and the non-significant difference of H-scores within one patient make CD44v6 a promising marker for the identification of CC cells in tumour and lymph node metastases. However, the sample size was limited, and a follow-up study with a higher sample size is required to confirm the results.

(b) An ICG quantification study in patients

Ultimately, CD44v6 is combined with an NIR dye to identify the SLN *in vivo* and quantification of this fluorescence signal should be investigated. Therefore, the aim was to construct a reliable segmentation and quantification method of the SLN in operative footage.
Patients who received surgery to treat CC with NIR SLN identification using ICG were included. The lymph nodes were segmented in the operative footage based on thresholding in the HSV colour space.
Two patients were included, a segmentation was performed, and the average intensity of the ICG in the lymph nodes was calculated.
The segmentation and quantification method constructed is reliable, therewith providing possibilities for CC cell identification using a specific NIR tracer. A limitation is a non-standardised measurement making comparison between patients impossible since the pixel intensity is influenced by camera distance and orientation. Currently, research is continuing into standardisation possibilities.

(c) A fluorescence intensity phantom study

Fluorescence intensity depends on many operator, patient, and system dependent variables and is therefore easily under- or overestimated. The aim was to design a phantom study to explore the effect of distance, orientation, concentration, and field of view (FOV) on the fluorescence intensity when using the Firefly Xi.
The phantom consisted of Eppendorf tubes filled with different concentrations of ICG diluted in PBS and 2% intralipid to induce scattering. Three types of measurements were performed: (1) dynamical measurements, (2) FOV measurements, and (3) static measurements. Segmentation was applied by thresholding in the HSV colour space or in the grey value image.
Both measurements 1 and 2 confirmed a non-uniformity of the fluorescence intensity within the FOV, where the highest intensity was found in the middle. The static measurements showed a difference in intensity when applying different distances and angles. A significant negative linear correlation to the pixel intensity was found considering distance to the camera and a significant non-linear correlation was found for orientation. Concerning concentration, a non-significant non-linear correlation was found.
This study was limited by the instability of ICG, the influence of ambient light, and a lack of preciseness considering the distances and orientations. All of these are present in a clinical setting. Therefore, based on these results, surgeons can be made aware of the influence of operator-dependent variables. Furthermore, the found correlations can contribute to a correction model enabling clinical interpretation of fluorescence intensity and enhancing the novel approach for SLN identification.

Conclusion

This study described the possibilities of using a specific NIR tracer in a novel approach for SLN detection in early-stage CC during robotic surgery. Although the clinical use depends on future research, the results in this master thesis path the way to intraoperative identification of CC cells and possibly decision making and prognosis based on the fluorescence intensity.

Preface

Het heeft even geduurd maar na zevenenhalf jaar is het zover en ga ik afstuderen. Mijn laatste jaar heeft in het teken gestaan van treinen naar Groningen om fantomen te maken, rennen naar OK om tussen operaties door mijn fantomen te meten, aanvragen van de zoveelste set weefsel om weer te treinen naar Groningen om het weefsel te bespreken, veel naar patiënten beelden kijken om de juiste tactiek te kiezen, natuurlijk een pandemie, maar vooral schrijven, schrijven en nog eens schrijven. In januari 2020 begon ik met afstuderen bij de chirurgie in het Meander Medisch centrum in Amersfoort nadat ik in het universitair medisch centrum Groningen een M2 stage had afgerond binnen hetzelfde onderwerp. Er lag voor mij geen uitgestippeld plan klaar, maar uiteindelijk is er wel een onderzoek uit voort gekomen waar ik een heleboel van heb kunnen leren.

Ik zou graag mijn commissie bedanken voor deze mogelijkheden. Prof. Misra en Christoff, die altijd klaar stonden voor mijn vragen. Prof. Dr. Consten, die ondanks de vaak volle klinische en wetenschappelijke agenda altijd tijd kon maken voor een grote cappuccino en een goed gesprek. Prof. Dr. Nagengast, die ondanks de afstand in kilometers of de afstand door de maatregelen altijd makkelijk en snel te bereiken was en enthousiast was over mijn ideeën. Rian, die ik anderhalf jaar geleden heb leren kennen via beeld vanuit West-Afrika en waarvan ik nu ook weer afscheid neem via beeld, maar die mij desondanks veel heeft uitgedaagd en veel over mijzelf heeft geleerd. En natuurlijk Tim Boers voor zijn aanwezigheid bij mijn colloquium.

Daarnaast wil ik graag Iris bedanken die ik altijd mocht overladen met WhatsApp berichtjes en mailtjes (ook als dat er meerdere per dag waren), die altijd binnen een mum van tijd antwoord gaf en die altijd klaarstond om voor de zoveelste keer mijn thesis door te lezen of om over mijn (of haar) toekomst te praten. Verder wil ik natuurlijk alle TG'ers en PhD'ers die voorbij zijn gekomen, of waar ik aan voorbij ben gekomen, in het Meander bedanken voor het leren drinken van koffie, de plank minuutjes na de pauze en het warme welkom dat ik kreeg ondanks dat dat maar twee maanden heeft geduurd. In het bijzonder wil ik Daan, Inge en Eva benoemen die ook een gedeelte aan denkwerk in mijn thesis hebben zitten. En natuurlijk wil ik iedereen in het Meander en in het UMCG, die heeft bijgedragen aan het mogelijk maken van dit onderzoek en mijn stage, bedanken.

Ook wil ik een 'shout out' doen naar mijn dispuut, Quenouille. Zonder deze ambitieuze, wereldwijze, confronterende, kritische, alcohol drinkende en theeleutende groep vrouwen had ik nooit de grenzen van mijn kunnen en ambities opgezocht tijdens mijn studententijd in Enschede.

En natuurlijk Nadia, mijn oudste vriendinnetje en surrogaat zusje die mij elke keer even helemaal uit mijn bubbel trok in de hare en mijn prachtige voorblad ontwierp.

Tot slot wil ik graag mijn ouders bedanken voor hun steun en vooral vertrouwen. Het was soms lastig uit te leggen wat ik aan het doen was, en vooral waarom, maar ook al lag mijn studie een jaar stil omdat ik 'mezelf wilde ontwikkelen (met bier) tijdens een bestuursjaar' of 'de gezondheidszorg in Afrika wilde ontdekken'. Het vertrouwen bleef, het zou wel goed komen. En dat doet het, nu, eindelijk!

Als allerlaatste wil ik Wietse bedanken, die mij er telkens aan herinnert dat het ook goed komt als het niet goed komt en net niet goed genoeg ook goed genoeg is, maar die er door zijn motiverende en nuchtere woorden toch voor zorgt dat ik het uiterste uit mezelf blijf halen.

Heel veel plezier met het lezen van dit werk.

Andrea Sterkenburg

Table of Contents

α	orientation.
β	concentration of ICG.
CC	colon carcinoma.
CT	computed tomography.
d	camera distance.
DMSO	dimethyl sulfoxide.
FCS	fetal calf serum.
FOV	field of view.
GI	gastrointestinal.
HE	haematoxylin and eosin.
HSV	hue, value and saturation.
ICG	indocyanine green.
IHC	immunohistochemistry.
MRI	magnetic resonance imaging.
mse	mean squared error.
N-	a lymph node without metastasis.
N+	a lymph node with metastasis.
NIR	near-infrared.
PBS	phosphate-buffered saline.
RGB	red, green and blue.
ROI	region of interest.
SLN	sentinel lymph node.
T	tumour tissue.
TD	tumour deposit.
uint8	unsigned eight bit integer.
UMCG	University Medical Centre Groningen.

List of Figures

List of Tables

CHAPTER 1

Introduction

Colon cancer or colon carcinoma (CC) accounted for almost 4000 deaths in 2017 and 10.000 newly diagnosed cases in 2018 in the Netherlands. [1] Moreover, it is the cancer type with the second highest morbidity in the country. [1–3] A national screening programme has started in 2014 in the Netherlands including all inhabitants aged 55–75. [3] The expectation is that the prevalence of CC will only rise in the coming years due to this programme and the growing and ageing population. [4] This rise of prevalence calls for optimisation of diagnosis and treatment as early diagnosis and treatment increase prognosis of patients with CC and prevent spread of the disease to lymph nodes. [3]

Malignant lymph nodes need to be identified and resected to prevent distant metastasis in the future. However, in early stages of the disease, uncertainty concerning undetected malignant lymph nodes can be a problem. [5] By definition, early-stage CC is node negative and patients will not receive adjuvant chemotherapy, which prevents distant metastasis in the future, after surgical treatment. Still, a 5-year survival of only 75% to 90% is found in these cases. [5] In addition, 20% will develop distant metastases within five years. [6, 7] It has been suggested that these numbers are caused by unidentified (micro)metastases during the initial histological analysis of the harvested lymph nodes. This is referred to as understaging. [5] These (micro)metastases can cause recurrence of the disease. Current preoperative imaging modalities such as computed tomography (CT) and magnetic resonance imaging (MRI) are unable to take away this uncertainty due to their limited resolution ranging from 0.8 mm to 1 cm, which is too large for detection of micrometastasis. [8, 9] Moreover, one of the main challenges in surgical oncology is the intraoperative detection of preoperatively detected cancer lesions as the surgeon depends on visual inspection and palpation only to identify any malignant lesions. [5, 10, 11] To prevent mortality due to understaging and missed micrometastases, and therewith a non-sufficient treatment, a hemicolectomy is performed. This decreases the possibilities of remaining micrometastases and the recurrence of the disease. However, it increases the morbidity and mortality risk due to the procedure. [5, 10, 12, 13]

More advanced pathological techniques, referred to as ultrastaging techniques, can be used to histologically examine tissue and prevent understaging. Ultrastaging can lead to upstaging, when micrometastasis or isolated tumour cells are found even though the patient had a negative lymph node status after regular pathological examination. In literature, a 15% - 18% upstaging is mentioned. Upstaging all these patients could result in a higher disease free survival because

of adequate treatment. [6, 14] Although ultrastaging is more accurate and can lead to a higher 5-year survival rate, these techniques are not used in everyday practice since it is labour- and cost-intensive. [7, 15–18]

A sentinel lymph node (SLN) biopsy could form a solution to increase the 5-year survival percentages mentioned above and can function as a triage procedure. A lymph node biopsy can provide information about the stage of the disease and its clinical use was first described by Gould in 1960. [19] In 1977, Cabanas showed the existence of an SLN in penile cancer and confirmed this to be the first draining lymph node of a tumour. In clinically non-suspicious nodes, it was often the only lymph node affected. [20] The technique is already successfully used in breast and skin cancer. In breast cancer, it has been shown that targeted removal of the SLN leads to lower rates of recurrence of the disease. [21] The SLN is resected, and if no metastasis is found it can be said, with high certainty, that no metastases are present elsewhere in the body. [5, 20] To further enhance the treatment, ultrastaging can be used to stage the SLN. Applying this technique mainly on the SLN instead of all lymph nodes will reduce the workload, increase the cost-efficiency of the procedure and reduce morbidity associated with a bowel resection and larger lymph node dissection. [17]

In a systematic review by Van der Pas *et al.* a sensitivity of 76% was found for the SLN identification in colorectal cancer using a tracer. [5] A sub study with eight high quality studies, which included ultrastaging, showed a sensitivity of 0.9 in CC, which is similar to the sensitivity achieved in breast cancer. Nevertheless, ultrastaging causes extra workload for the pathologists and large prospective studies are needed to establish the prognostic significance and consequences for adjuvant therapy. *In vivo* SLN identification could improve results compared to *ex vivo* identification as this might alter the lymph flow pattern. Additionally, large tumours in a later stage of the disease can alter the lymph flow patterns by pressure of the tumour on the lymphatic vessels. The dye or tracer will take the route of lesser resistance and end up in a non-SLN. Furthermore, Van der Pas *et al.* stated that the use of indocyanine green (ICG), a near-infrared (NIR) dye, could improve SLN identification. [5] To improve SLN detection even more, ICG could be combined with a specific biomarker. This combination would create a specific NIR tracer, lighting up when tumour cells are present. Therewith, preventing the need for a large bowel resection.

Aim of this master thesis

Based on the theoretical framework, the research question for this thesis is: *"What are the possibilities of using a specific NIR tracer in detecting the sentinel lymph node and making a prognosis in early-stage colon cancer?"*. The objectives for this master thesis are described below. Chapter 2 of this thesis describes the essential literature and knowledge to understand the research. Chapter 3, 4, and 5 show the methods and results for objectives 1, 2, and 3. Chapter 6 provides the general conclusion and the future outlook.

The Objectives

1. *Evaluate a promising biomarker for the identification of tumour cells in lymph nodes.* Molecular imaging improves the optical discrimination between malignant and non-malignant cells by targeting proteins overexpressed in dysplastic or malignant cells. In 2017, Hartmans *et al.* investigated biomarkers applicable for colorectal cancer. Using functional genomic mRNA, CD44v6 was found to be an attractive target in colorectal cancer. [22] Prior to this research, a pilot study was performed using a CD44v6 targeted biomarker in IHC. The results were not considered satisfactory yet. Still, based on literature and discussions with experts, it was decided to continue the research. The results of using CD44v6 as a marker for early-stage CC are evaluated and reported in this thesis.

2. *Set up an ICG quantification study in patients to explore the possibilities of quantifying the fluorescence intensity.*
   In the future, it would be useful if a biomarker and a fluorescent marker like ICG can be combined to create a specific *in vivo* marker. This provides information about the presence of cancer cells in the lymph nodes. Next to this, it might be possible to relate the fluorescence intensity to the number of cancer cells or the size of the metastasis in the lymph nodes. Maybe the fluorescence intensity could even be related to the outcome or prognosis of the patient. To use this, more information is needed about the segmentation and quantification of the fluorescence intensity in lymph nodes, which has shown to be important in different literature. [9, 23] In this master thesis, an example for segmentation and quantification is given in two patients using image processing.

3. *Set up an ICG quantification phantom study to explore the different variables influencing the intensity on screen.*
   The intensity of the fluorescence depends on many aspects. For example, the type of camera, the distance to the region of interest or patient dependent factors. [24] To investigate how distance to the camera, concentration of the fluorophore and the orientation of the camera influence the intensity, a phantom study was set up. The results of this phantom study may be used in future research to show the influences of the different aspects.

CHAPTER 2

Background

In this chapter, an overview of the relevant literature is provided. An expansion on the introduction regarding CC and prior research into the SLN method will be given in the first four sections. The fifth section will expand on light-tissue interactions and in the sixth section an explanation on fluorescence and additionally, previous research into fluorescence quantification is given.

2.1 The anatomy of the gastrointestinal tract and the lymph nodes

The colon is part of the gastrointestinal (GI) tract (Figure 2.1). The GI tract starts at the mouth, is followed by the oesophagus and the stomach, and continues into the small intestine and the colon. In the colon, water is resorbed and eventually faecal matter is expelled through the rectum. [25] The colon roughly consists of four layers (Figure 2.2). Seen from the interior, the mucosa is found surrounding the lumen, followed by the submucosa, the muscularis externa, and the serosa. [26]

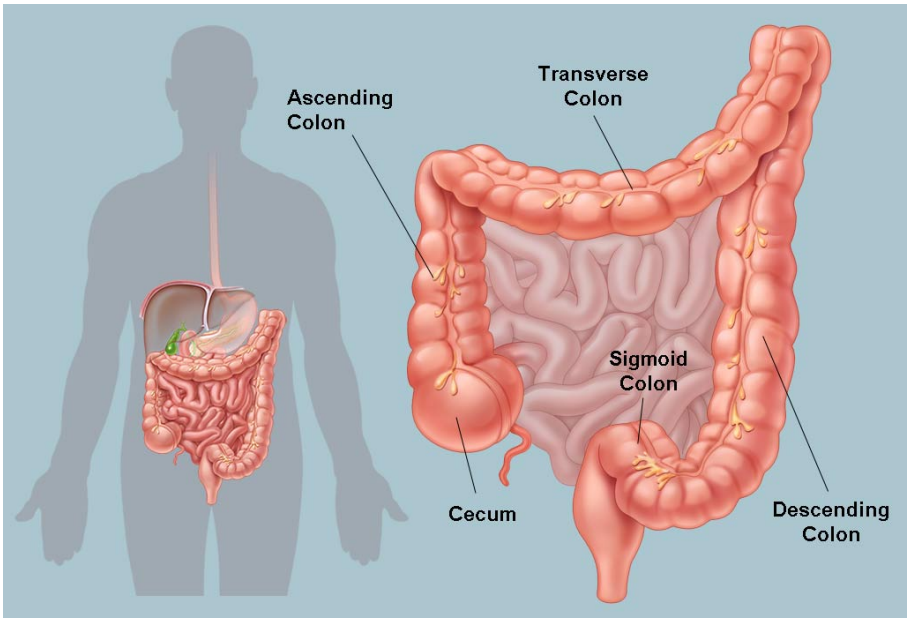

FIGURE 2.1: Anatomy of the GI tract
The last part of the small intestine, known as ileum, continues into the colon, the cecum is the first part of the colon. The rectum stores the faeces until it leaves the body through the anus. [27]

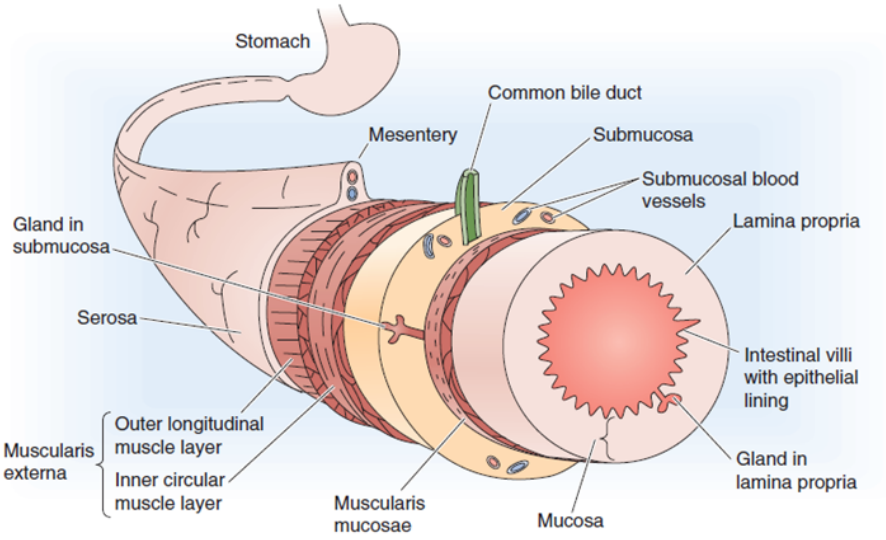

FIGURE 2.2: The layers in the colon wall and the surrounding tissue and glands
The mucosa, submucosa with glands and blood vessels, the muscularis externa and the serosa are shown. Also some glands and the mesentery surrounding the colon are included in this figure. [28]

Lymph vessels and nodes are found throughout the whole body and form one network, referred to as the lymphatic system, which transports fluids through the body. Figure 2.3 provides an interpretation of how this looks like surrounding the colon. The lymph vessels are lined by endothelium and surrounded by a smooth muscle framework. When blood circulates through the body, fluids and proteins leak out. This bloodless fluid is then collected by the lymphatic vessels and returned into the venous circulation. Besides collecting this fluid, the lymphatic system also plays a part in the immune response by transporting white blood cells. [26] The involvement of the lymphatic system in the spreading of cancer has long been recognized.

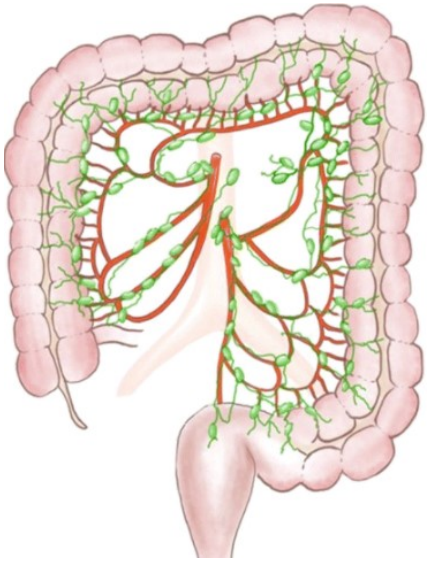

FIGURE 2.3: The lymph nodes surrounding the colon [29]

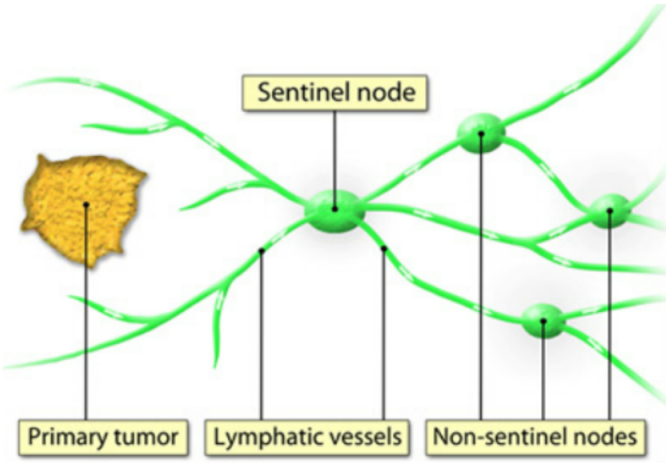

FIGURE 2.4: A schematic representation of the SLN [23]

When cancer cells are found in a lymph node this is referred to as a positive lymph node status and the SLN is considered to be the first lymph node (Figure 2.4). A negative or positive lymph node status is an important parameter to determine the stage of the disease and decide on the treatment. [30]

2.2 Diagnosis of colon carcinoma

Cancer on itself is a neoplastic condition which results from genetic changes. These changes control the proliferation, maturation, and metastatic behaviour of the cells and happen through random replication errors, faulty DNA repair, or exposure to carcinogens. Several regulatory circuits are altered during this tumour progression. In CC, these affections can be caused by a genetic factor, meaning there is an increased risk if a first degree relative has had the disease or a precursor of the disease. [31] Next to familial causes, lifestyle can have an influence on the risk for CC, for example, a diet with a shortage of fruit, vegetables, and whole grains, obesity, a lack of physical activity, smoking, and alcohol use. [32] Furthermore inflammatory bowel diseases such as ulcerative colitis and Crohn's disease increase the risk. [4, 33] The anatomic precursor of CC is an adenomatous polyp, a benign pathological growth, from the mucosa. [31]

Patients diagnosed with CC can be either asymptomatic or symptomatic. Usually, asymptomatic patients are diagnosed through the national screening programme, and symptomatic patients present themselves with abdominal pain, change in bowel habits, and rectal bleeding. All of which are common complaints in any gastrointestinal disease. Therefore, additional medical examination is needed. The gold standard for diagnosis is colonoscopy with biopsies, taken from suspicious lesions for histopathological conformation. Other diagnostic methods are CT or MRI to gather information about the anatomy. [3, 34]

2.2.1 Staging in colon carcinoma

After diagnosis with a colonoscopy and if necessary imaging with MRI or CT, the tumour can be classified according to the TNM classification (Table 2.1). T defines the growth of the tumour (Figure 2.5); N describes the infiltration of the lymph nodes and M describes metastasis to different organs. Based on this classification, which might be revised after surgery, the cancer can be staged (Table 2.2) and a treatment plan set up. [3] Due to the screening programme

for large bowel cancer, improvement of diagnostic technology, and a growing public awareness, diagnosis is increasingly done in earlier stages of the disease, stage I and stage II. [8, 9]

TABLE 2.1: TNM classification

T	T_1	The tumour is restricted to the submucosa.
	T_2	The tumour has grown into the muscularis propria.
	T_3	The tumour has grown into the serosa.
	T_4	The tumour has penetrated through the serosa and peritoneal surface.
N	N_0	No tumour cells in lymph nodes.
	N_1	Tumour cells are found in up to three regional lymph nodes.
	N_2	Tumour cells are found in four or more regional lymph nodes.
M	M_0	No metastasis is found in distant organs.
	M_1	Metastasis is found in distant organs.

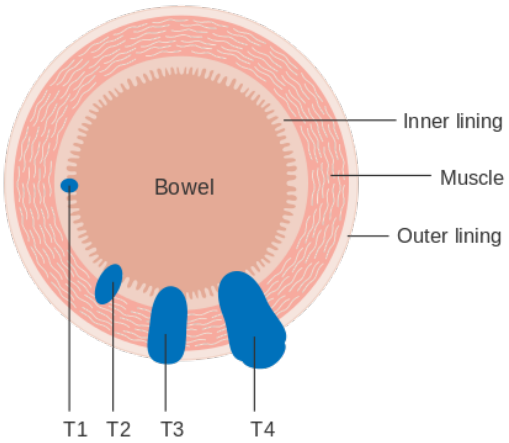

FIGURE 2.5: T classifications in CC
The submucosa is represented in this image by the 'inner lining', the muscularis propria by the 'muscle', and the serosa by the 'outer lining'. [35]

TABLE 2.2: Staging in CC using TNM classification

Stage I	$T_{1\text{-}2}N_0M_0$
Stage II	$T_{3\text{-}4}N_0M_0$
Stage III	$T_{1\text{-}4}N_{1\text{-}2}M_0$
Stage IV	$T_{1\text{-}4}N_{1\text{-}2}M_1$

2.2.2 Pathology in colon carcinoma

Using single-section examination and haematoxylin and eosin (HE) staining, the lymph nodes and tumour resected during surgery are manually assessed by the pathologist for tumour staging. The outcome of this histopathological examination is the most important indication for adjuvant chemotherapy. [36] As mentioned in chapter 1, patients with stage I and II CC can highly benefit from optimal pathological examination, referred to as ultrastaging, to indicate possible micrometastases. [36] Ultrastaging may involve serial slicing in which the pathologist will carefully dissect the tissue, stain it with HE, and additionally use IHC stains targeted at specific biomarkers or reversed transcriptase polymerase chain reaction to identify micrometastases. [6, 14, 22] Although ultrastaging is more accurate, these techniques are not used in everyday practice when analysing all the lymph nodes after a segmental resection, since it is labour intensive and costly. [15–18]

2.3 Treatment in colon carcinoma

The type of treatment depends on the stage of the disease. In case of benign or early-stage disease, a polypectomy (endoscopic resection) will suffice and a large surgical en-bloc resection is unnecessary traumatic. For any other stage, surgical resection in the form of a hemicolectomy is necessary to prevent spread and recurrence of the disease. During surgical resection, the bowel and the associated mesentery will be excised up to the level of the origin of the tumours vascular supply and all the including lymph nodes. [3, 5, 37] Furthermore, chemotherapy can be indicated to prevent lymphatic or distant metastases. [3, 37] After surgery and possible chemotherapy, patients will have a standard follow-up as stated by the national guideline. [3] This may include a scheduled CT-scan and carcino-embryonal antigen blood check for up until five years. Figure 2.6 shows the complete diagnosis and treatment in a flowchart.

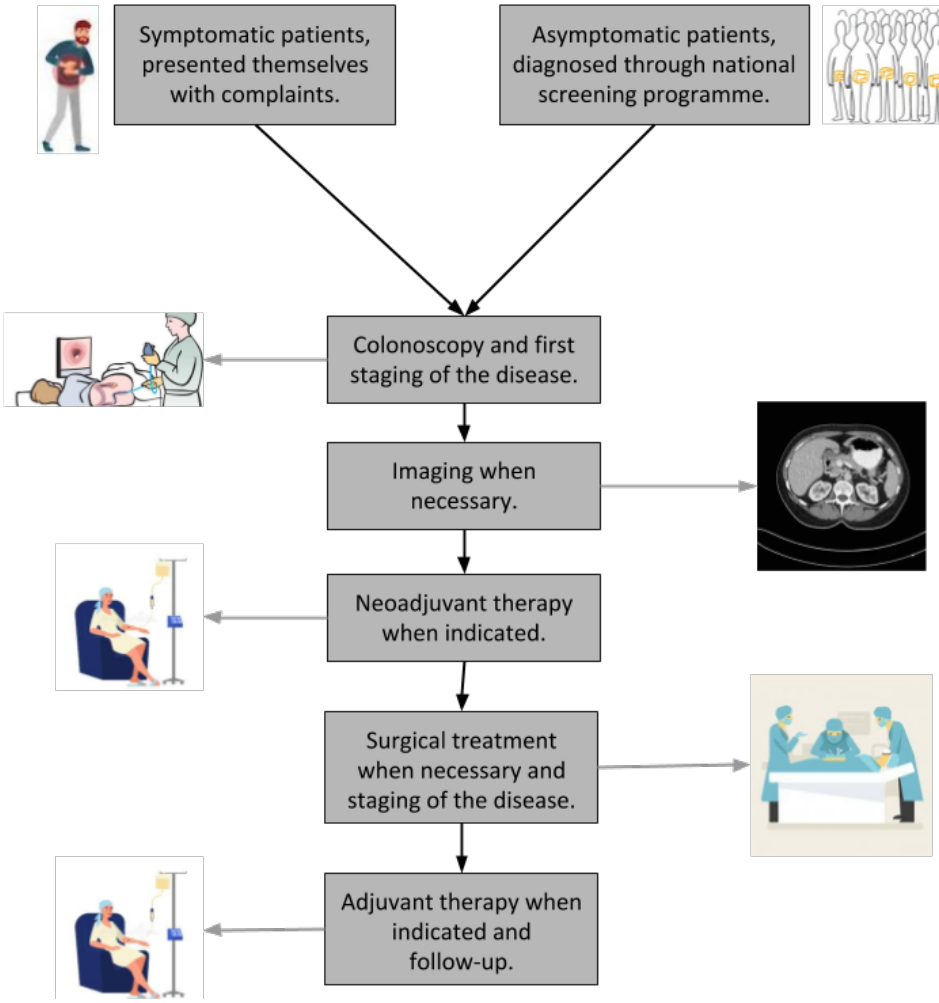

FIGURE 2.6: Process from diagnosis to treatment in CC
This flowchart shows the process from patient presentation to follow-up. (Neo)adjuvant therapy is chemotherapy. (Sources images [38–43])

2.4 Previous research into sentinel lymph node biopsy

In 1960, Gould [19] was the first to describe the principle of the SLN, and Cabanas [20] was the first in 1977 to describe a routine approach in cancer using the SLN biopsy in penile cancer. Ever since, SLN biopsies are routinely performed in breast and skin cancer leading to lower recurrence rates. [5] To clinically identify the SLN, a tracer can be used. Tracers are injected

peritumoural and are either (NIR) dyes, radioisotopes, biomarkers or a combination of the substances. [44] Until now, tracers are the major limitation of identifying the SLN during surgery, mainly because of their poor visualization. [37] Dyes are known to travel fast which is inconvenient for this purpose since the SLN is the first lymph node to be seen. Next to this, the dye-guided method provides poor tissue contrast since it is difficult to detect in adipose mesenteric tissue. Furthermore, using a radioactive tracer can result in signal interference when the SLN is located close the tumour and it is challenging to image the lymph node and lymph vessels intraoperatively. [37, 45] Lastly, a biomarker, on its own, cannot be visualized intraoperatively. [46]

The concept of the SLN biopsy in CC has been explored previously. In 2001 Wood *et al.* showed that lymphatic mapping of SLN draining in primary colorectal cancer can be performed accurately. [47] A few years later, in 2007, a multicenter study showed a 89% sensitivity and a negative predictive value of 93% of SLN identification in CC. [14] Different feasibility studies were done, using ICG as a tracer during minimal invasive surgery. Shortcomings mentioned are: (1) drainage into adjacent lymph vessels instead of draining into the SLN due to incorrect placement of the needle and obstruction [36], (2) an alternative route of lymph flow due to obliteration or in-growth of the lymph vessel by a large tumour [36], (3) 'skip metastases', metastases skipping the SLN which is found in 1 - 3% of the cases [48, 49] (4) SLN mapping is challenged by multidirectional lymphatic flow found in the GI tract [50]. To overcome the last shortcoming as much as possible it is advised to inject the tracer submucosally instead of subserosally. [45] Despite the drawback described in several studies, Dogan *et al.* conclude in a literature review from 2019, routine SLN biopsy will improve the quality of life of the patients with early-stage CC. [44]

2.5 Light

To understand fluorescence, it is important to understand light-tissue interactions. Light can be described in two ways: either with the quantum or the classical theory. The classical theory is used to define the dynamics of light propagation mathematically and the quantum theory is used when necessary, for example to account for absorption or luminescence. [51]

In the classical theory, light is considered to be an oscillating electromagnetic field with continuous energy and a certain wavelength. This wavelength defines the colour in the area visible to humans: 100 nm to 400 nm which is also called the optical window. Most biological tissue shows strong optical scattering in this region and is therefore referred to as a turbid media. [51, 52] Nevertheless, there are more wavelengths, as seen in Figure 2.7. An important area in this research is the NIR area, which provides wavelengths which excite ICG as will be explained in section 2.6. The quantum theory describes light waves as packets of energy referred to as photons. The energy is proportional to the frequency of the electromagnetic wave and the energy can be exchanged between light and matter. [51]

2.5.1 The structure of an atom

To understand light-tissue interactions it is important to understand the structure of an atom. An atom is the smallest division in which the chemical identity of an element is preserved. It is composed of a positively charged nucleus with protons and neutrons and an extranuclear cloud of negatively charged electrons, as can be seen in Figure 2.8. When the number of electrons and protons are equal an atom is electrically neutral. The electrons circle around the nucleus at fixed distances in electron shells. In the innermost shell the electrons have the lowest energy. Each shell has room for a fixed even amount of electrons which are paired together in orbitals. [53]

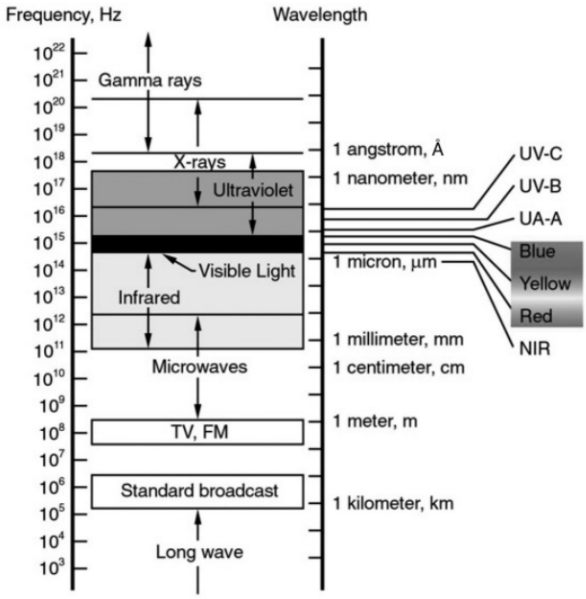

FIGURE 2.7: The electromagnetic spectrum
At the left of the image the frequencies are found and at the right the wavelengths. [51]

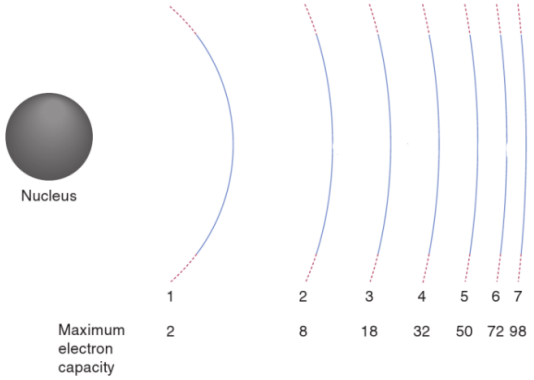

FIGURE 2.8: The electron shells
The electron shells and their maximum electron capacity. [53]

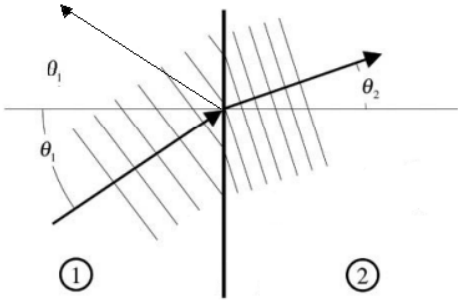

FIGURE 2.9: Light refraction
A light wave propagating through material 1 encounters a boundary with material 2. θ_1 is the angle of incidence which is different from θ_2, the refraction angle. On the left of the image the reflection wave is also shown. The reflection angle is the same as the angle of incidence.Adopted from [51]

2.5.2 Light tissue interactions

Four light-tissue interactions are known; refraction, reflection, scattering, and absorption. Refraction, the fourth one, happens when a light wave propagates through a material with a certain refraction index and encounters a boundary of a second material with a different refraction index. The path of the light is then redirected as can be seen in Figure 2.9. A part of the incident light wave gets reflected instead of refracted. How much of the light wave gets reflected or refracted depends on the refractive indices, the angle of incidence and the polarization of the incoming wave. The refractive index also defines the speed of light in the tissue. [51]

The other three those interactions are shown in Figure 2.10. [51] When there is only a localized concentration of a different material within a material, scattering will occur. A medium has a

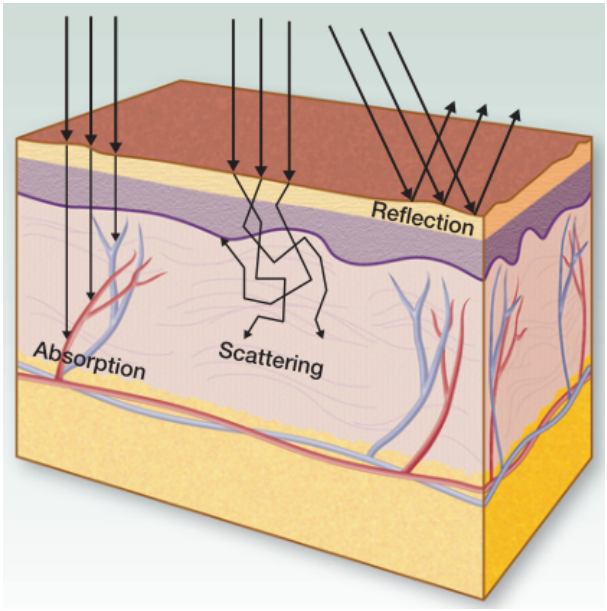

FIGURE 2.10: Light-tissue interactions
This figure shows absorption, scattering and reflection, three possible events that can happen when a ray of light travels through tissue. [54]

scatter coefficient defining the density and the distance of the path of scattering photons. [51] This coefficient depends on the wavelength of the incoming light. The direction of the scattering is determined by the phase function g, a number between 1 and -1. $g = 1$ denotes purely forward scattering and $g = -1$ backward scattering. $g = 0$ results in isotropic scattering, meaning the scattering occurs evenly in all directions. Most biological tissues have $g > 0.7$, meaning the scattering occurs in forward direction for the larger part. [52]

Absorption is when a photon is extracted from light travelling through tissue. All tissue components can absorb photons. The most relevant absorbers are lipids, water, and (de)oxyhemoglobin. [54] Absorption triggers a shift from one energy level to another which is referred to as transition. The penetration depth of light depends on how strongly the light is absorbed. The probability of photon absorption in a medium per unit path length is given by the absorption coefficient. When transition happens from a lower state to a higher state this is excitation. A certain amount of photon energy has to be absorbed to allow transition. The other way around, the drop from a higher energy level to a lower level, is called decay. This results in a release of energy equal to the difference between the two energy levels. Decay may result in warming up the surrounding tissue but it may also give rise to emission of a photon which may result in luminescence, often it is a combination of the two. Luminescence can be further broken down into fluorescence, prompt emission (nanoseconds), and phosphorescence, delayed emission (milliseconds and longer). Fluorescence is a more common phenomenon in tissue, phosphorescence is often involved in photodynamic therapy. [51]

2.6 Fluorescence

Fluorescence is in theory an ideal modality to improve surgical procedures. It can be directly related to the surgeon's vision and it can reveal surgical markers otherwise invisible to the naked eye, like tumour delineation or sentinel lymph node identification. Interpretation of fluorescence is compromised due to a nonlinear relationship between the measured intensity and actual fluorescence concentration due to the effect of the tissue's optical properties. Highly

vascularized tumours, for example, may show darker on screen than their surroundings due to high absorption of light by the blood even if they contain larger amounts of the fluorophore. Likewise, a semi-transparent lymph node may appear brighter than its surroundings while having the same concentration of fluorophore. The intensity also depends non-linearly on the depth of the fluorescence activity. A superficial fluorescent lesion will therefore appear brighter than an identical lesion located deeper. [55] The information provided is therefore not quantitative and relies on subjective assessments of the fluorescence intensity. [56] Fluorescence happens after absorption and is caused by an electron transition from the excited state to the ground state of molecule. [57] Organic molecules mostly contain an even number of electrons paired together in one orbital. The ground state of a molecule has no net electron spin, since electrons are always paired and have spins in opposite direction (also known as a singlet state). When a molecule gets excited this results in the promotion of one electron from the highest occupied orbital to another orbital. This can result in an uneven distribution of electrons among the orbitals, resulting in a different net electron spin, as shown in Figure 2.11. [58]

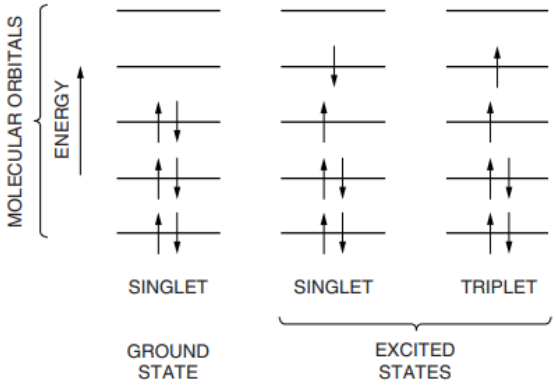

FIGURE 2.11: The spin arrangements in molecular orbitals
A schematic diagram of the spin arrangements in molecular orbitals for the ground state and the excited stages. The lines represent the different orbitals and each arrow represents an electron, the direction of the arrow indicates the spin of the electron. [58]

Fluorescence systems for *in vivo* diagnostics have an excitation light which is guided to the tissue. [57] The excitation light excites the tissue and induces fluorescence emission which can be illustrated using a Jablonski diagram (Figure 2.12). [58] The excitation light and fluorescence emission are of different wavelengths, which is called the stokes shift. [54]

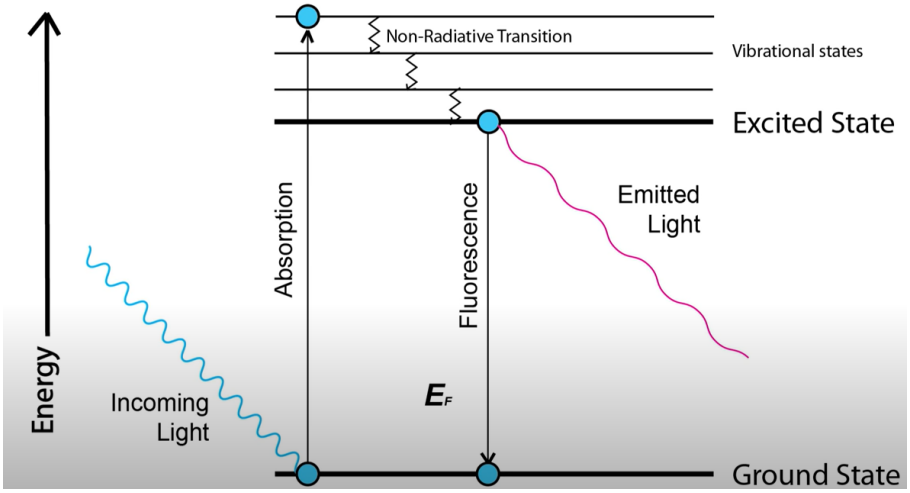

FIGURE 2.12: A Jablonski diagram
When a ray of light excites the molecule in the ground state, at the left of the image, energy is absorbed, and an electron moves to a higher orbital. After a vibrational state the electron loses energy and light with a fluorescence wave length.

Since fluorescence is in the NIR region it cannot be seen by the naked eye and therefore needs to be captured by a NIR camera. A camera sensitive to fluorescence photons captures the fluorescence emission, Figure 2.13 shows a simplification of such a camera. After emission, the fluorescence photons will also be influenced by scattering and absorption in the tissue, and reflection and refraction at the surface influencing the number of photons and their wavelength reaching the camera. Using a high-pass and low-pass filter, photons with the excitation wavelengths are blocked. By using a beam splitter (Figure 2.14), it is possible to show the white light image and the fluorescence image simultaneously using an overlay (Figure 2.15), which generates usable intraoperative footage. [24, 54]

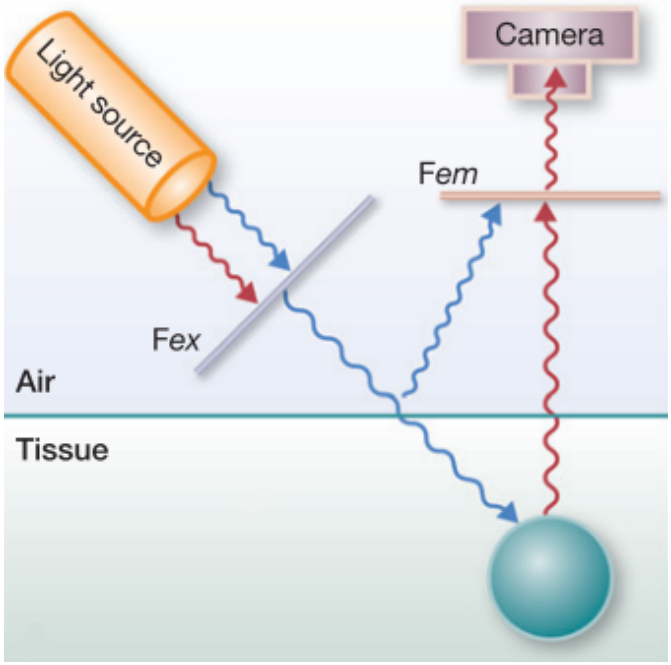

FIGURE 2.13: A simple display of fluorescence imaging
Using the filter 'Fex' (excitation) a light wave with the appropriate excitation wavelength is directed at the tissue. This excitation light wave travels through the tissue, is absorbed by the atom which emits light with a different wavelength. A small portion of the emitted light will exit the tissue and can be detected by the camera. The filter 'Fem' (emission) is placed in front of the camera to ensure only the emitted light passes on to the lens of the camera. [54]

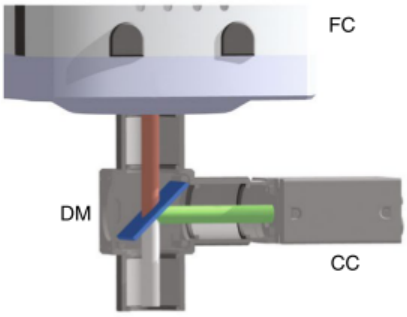

FIGURE 2.14: A beam splitter
A close up view of the optical path of the visible light (the green path) which is directed to the colour camera (CC) and the NIR light (the brown path) which is directed to the fluorescence camera (FC). The dichroic mirror (DM) splits the beam. [24]

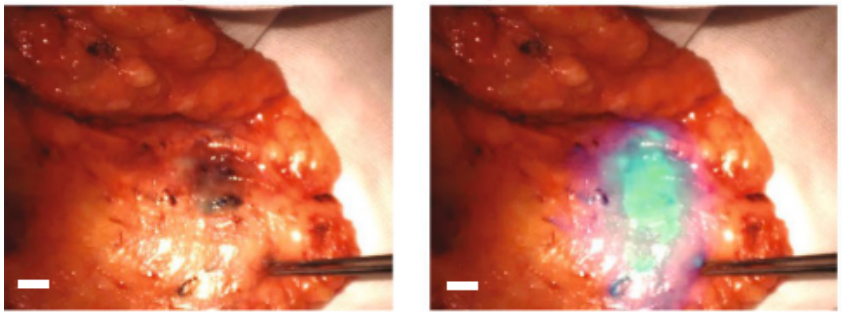

FIGURE 2.15: Hybrid imaging
Intraoperative white light image of breast tissue. The left image shows the regular white light image and the right image shows an overlay with fluorescence. [24]

2.6.1 Previous research into quantification of fluorescence

Many factors influence the fluorescence intensity seen on screen, nevertheless the quantification of fluorescence intensity is an interesting subject because of its potentials. [24] When chemically coupling fluorescent dyes to a biomarker to create a specific tracer to recognize a target protein on a CC cell, CC cells can be visualized and identified intraoperatively. [56, 59] Nevertheless, fluorescent dyes are often used as a nonspecific tracer to light up vascular structures. An aim of fluorescence imaging is representing the distribution and concentration of the fluorescent tracer. This implies that there should be a linear relationship between the amount of tracer and the

signal strength, and that the intensity recorded, solely depends on the concentration of the tracer. In reality, many parameters affect the registered intensity. White light images are based on photons reflecting at the tissue surface whereas fluorescence photons are generated within the tissue therefore, optical properties have a large influence on the registered intensity. [24] Besides optical properties, operator variables such as camera to surface distance, the camera angle or the automatic corrections, may influence the intensity as well. Therefore, the degree of fluorescence can easily be under- or overestimated. [60]

Sensitivity is an important evaluation parameter of a camera system. Typically, targeted fluorescent tracers are found in low concentrations and low sensitive cameras might miss these low concentrations. [24] Koch *et al.* summarised variable and invariable (usually not changed within a measurement) parameters influencing the intensity of the registered fluorescence (Table 2.3). [24]

Table 2.3: Parameters affecting the registered fluorescence intensity [24]

Parameter	**Influence on the resulting image**
Invariable parameters	
Camera sensitivity	The worse this parameter, the larger the required dose of the fluorescent agent.
Resolution	Defines the minimum lesion visible on the white light images.
Dynamic range	The ability to differentiate between different concentrations of the fluorescent agent.
Dark current	Electronic leakage at the receptor can lead to saturation effects. [59]
Frame capture speed	The quality of the video.
Spectral coverage	Whether or not the used fluorescent agent emits light within the wavelengths the camera can record.
Filters, crosstalk, and ambient light	Reduces the sensitivity and increases the background noise and image artefacts.
Illumination intensity	The lower this parameter the larger the required dose of the fluorescent agent.
Illumination homogeneity	Causes shadowing effects at curved surfaces and variation between similar lesions therefore influences possible quantification.
Variable parameters	
Distance from the region of interest	Variations in the intensity registered.
Field of view	Changes the focus.
Depth of the focus	Can reduce the resolution by changing the distance or tissue elevation.
Variation of optical properties	Variation in fluorescence signal and agent distribution.
Autofluorescence	Reduces the sensitivity and may lead to false positives.
Lesion depth	Attenuation of the fluorescence signal and loss of resolution.

All these aspects influencing the intensity on screen contributed to the fact that there is an absence of established guidelines and standards for fluorescence imaging and interpretation. Therefore, statistical analysis and clinical performance of tracers reported are often study specific instead of tracer specific. Because of this, the use of specific tracers is often approved in combination with a certain camera and an objective interpretation is impossible. [24]

2.6.2 Indocyanine green

ICG, the fluorescent dye used in this master thesis, has been approved for clinical use in 1956 to monitor cardiocirculatory and liver function. Since then, the usefulness of the dye has spread to many other fields of medicine. ICG is eliminated by the liver and is therefore a safe and repeatable measure for perfusion rate. [61] ICG emits wavelengths that penetrate deeper into living tissue compared to visible light. Therefore, ICG or other NIR dyes would better visualize the SLN in the adipose mesocolon compared to regular dye. The excitation wavelength of ICG varies between 780 nm to 805 nm and the emission varies between 820 nm to 835 nm, the extinction coefficient is $4 \times 10^4 \,\mathrm{M\,cm^{-1}}$. [61, 62] In colorectal surgery, ICG is often used to subjectively assess the perfusion in anastomoses after a segmental bowel resection. But this method lacks predictive accuracy. [63] Next to this, it is important to remember that ICG is often used as a non-specific tracer and is therefore injected in quantities of tens of milligrams. Targeted agents, on the other hand, are usually given in concentrations about five to six orders of magnitude lower, reducing the sensitivity and influencing the possibilities for quantification. [24]

CHAPTER 3

A CD44v6 targeted biomarker

To discriminate between healthy cells and cancer cells molecular imaging, based on biomarkers, can be useful. The term 'biomarkers' was introduced to indicate a measurable and quantifiable biological parameter, like enzymes or hormones. Biomarkers can be located at cell membranes, in the extracellular matrix or the cytoplasm and can be overexpressed in pathological situations. [46, 64] Overexpressed biomarkers can be different in every type of cancer. [22, 64, 65] In 2017, Hartmans *et al.* [22] investigated biomarkers overexpressed in colorectal cancer, using functional genomic mRNA. They found CD44 to be an attractive target in colorectal cancer. CD44 refers to a large family of immunologically related cell-surface proteoglycan and glycoproteins and includes several isoforms. CD44s is the most common form and through alternative splicing CD44v2 through CD44v10 are formed. [66] They used CD44 epithelial splice variant v6 (CD44v6), a membrane protein, for target fluorescence imaging. [22] CD44v6 is more outspoken in early stages of CC, is related to a high incidence of distant metastasis and invasion of colorectal cancer and showed good imaging results in mice. [22, 67, 68] The aim of this chapter is to investigate the effectiveness of a CD44v6 targeted biomarker for the identification of early stage CC cells using IHC.

3.1 Methods

All included patients were treated for CC at the University Medical Centre Groningen (UMCG). Preference was given to early stage tumour and pathologically confirmed lymph node metastasis. Of each patient tumour tissue (T) and a lymph node with metastasis (N+) was selected. If an N+ was not available a tumour deposit (TD) was selected which is an isolated packet of cancer cells close to the primary tumour. Additional tissue was selected when available, like an adenomatous polyp and a lymph node without metastasis (N-). T and N+ were included to evaluate the correlation within a patient. N- was included to look into the specificity. An adenomatous polyp, a precursor of a tumor, was included out of curiosity since it could give an indication of the staining in early stage disease. Unfortunately, not all types of tissue were included for each patient due to limited availability.

3.1.1 Immunohistochemical staining

Two tissue slices of 4 µm were sliced from each formalin-fixed paraffin-embedded archival specimen. The slices were stained with the CD44v6 targeted biomarker (Abcam ab254174) and the gold standard: HE. Using HE staining, the CC cells can be identified with high sensitivity and specificity. First, the staining protocol was optimised. The optimisation was done using tissue from two different patients. One patient was recently treated for T_4 CC in the UMCG and tissue was obtained during surgery. The second patient recently underwent an endoscopic mucosal resection to treat dysplasia or very early stage CC in the UMCG and tissue was therefore obtained endoscopically. A negative and positive control in the form of healthy colon tissue and CC tissue were used. The tissue used for optimisation was not included in the eventual research.

Two factors were altered during optimization: (1) the CD44v6 targeted biomarker in a dilution of 1:50, 1:100 or 1:200, and (2) the buffer used for antigen retrieval: citrate buffer (pH=6.0), ethylenediaminetetraacetic acid buffer (pH=8.0) Tris-buffered saline (pH=9.0), and Tris-ethylenediaminetetraacetic acid buffer (pH=9.0). The optimal staining protocol with the CD44v6-targeted biomarker in a dilution of 1:200 and the Tris-buffered saline/ ethylenediaminetetraacetic acid as antigen retrieval was chosen together with an experienced pathologist based on a clear membrane staining and weak background staining. The complete protocol can be found in Appendix I.

3.1.2 Scoring and analysis

The stained slices were visually scored on membranous expression by an experienced pathologist and two students. The eventual score was based on the score given by the experienced pathologist but if the other scores deviated largely the score was reconsidered. Biomarker expression was scored on intensity (0 = none, 1+ = slight, 2+ = moderate, 3+ = strong) and percentage of this intensity in the tumour cells. Using formula 3.1 the H-score was calculated. The different scores are shown in Figure 3.1.

$$\begin{aligned}\text{H-score} = 0 \times \%\ \text{tumour cells with score } 0 + 1 \times \%\ \text{tumour cells with} \\ \text{score } 1 + 2 \times\ \%\ \text{tumour cells with score } 2 + 3 \times \%\ \text{tumour cells with score } 3\end{aligned} \quad (3.1)$$

After scoring the results were analysed using box-whisker plots, several descriptive statistics, and statistical tests. To define the difference between the means of different groups, different statistical tests were used, the Kruskal-Wallis test for non-paired, non-normally distributed, non-parametric data and three groups, the Mann-Whitney test for non-parametric non-paired data and two groups, and the Wilcoxon matched pairs test for paired non-parametric data. Differences in mean were considered statistically significant at a p-value <0.05. The scores between different tissue, treatment, and T-stage were compared and the scores within one patient were analyzed. These analyses were done using Microsoft Excel (version 2010, Microsoft, Redmond, Washington, USA) and Prism (version 9, GraphPad, San Diego, California, USA)

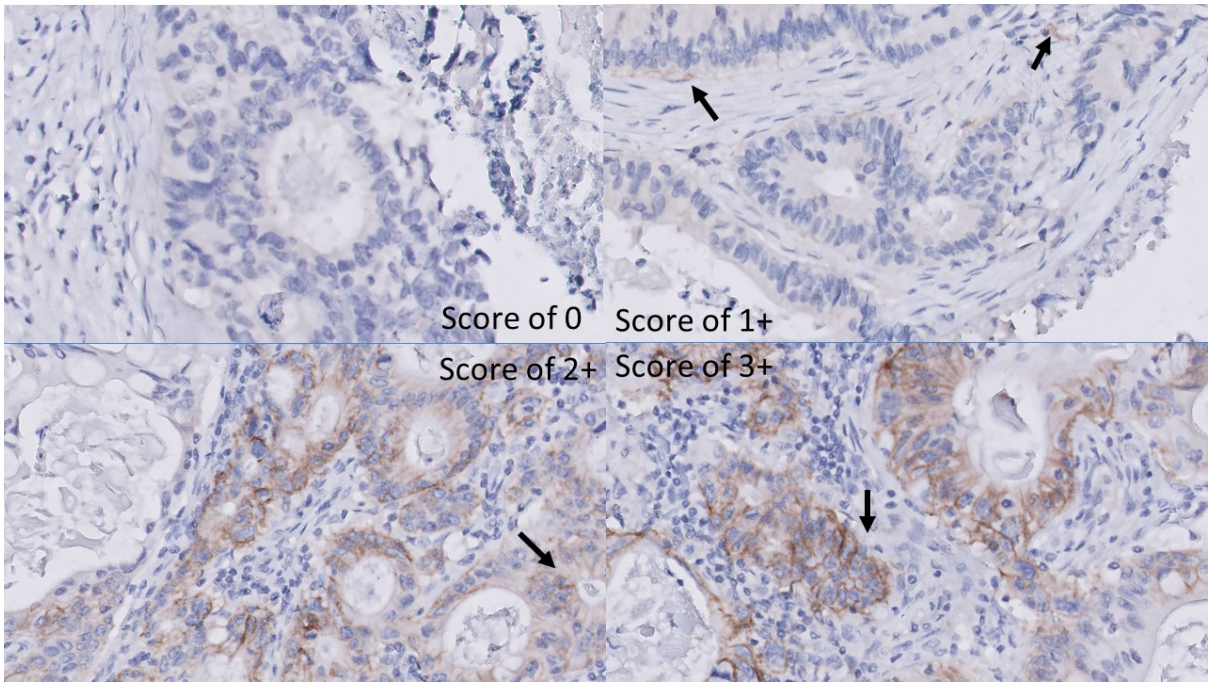

FIGURE 3.1: Examples of the different scores
This figure shows examples of the different scores that were given. The arrows indicate the best examples.

3.2 Results

Table 3.1 shows the included 21 patients and Table 3.2 shows the included tissue. From three patients an extra tumor slice was added to enlarge the T-group. The mean H-score was 106.8 with a standard deviation of 88.95, the complete results of the H-score can be found in Appendix II in Table A1. Figure 3.2 shows an example of strongly stained tumour cells. The polyp was not included for further analysis.

TABLE 3.1: Demographics of included patients

Characteristics		**Patients (n=21)**
Tumour stage	T_2	2
	T_3	7
	T_4	12
Neoadjuvant treatment	No	8
	Yes	13

TABLE 3.2: Types of included tissue

Tissue type (n=59)	**n**
T	24
N-	9
N+	19
TD	5
Polyp	1

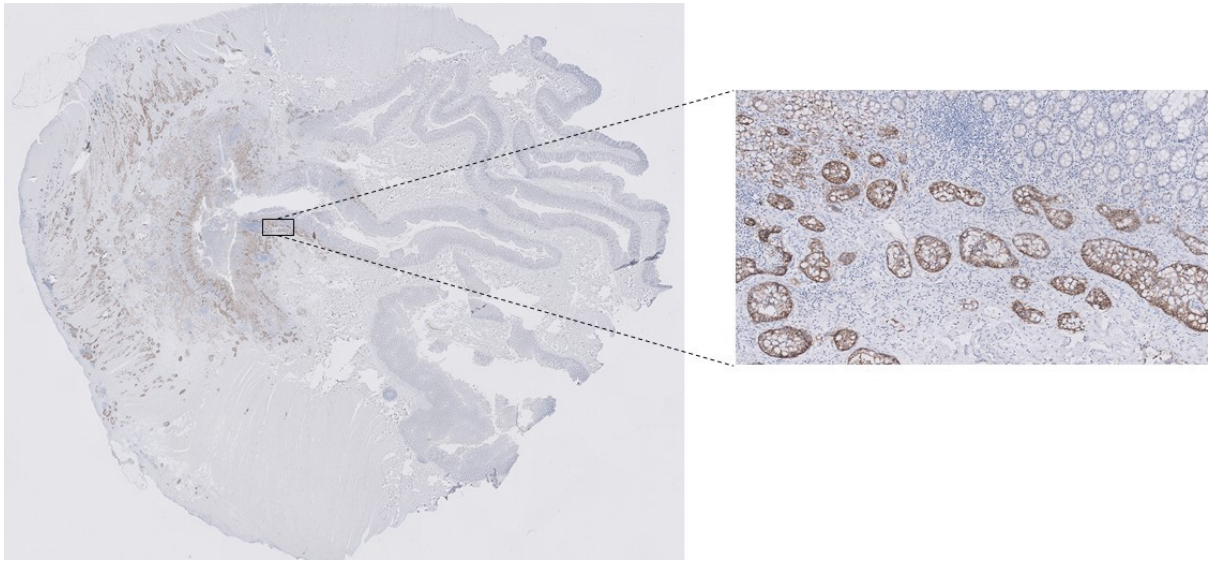

FIGURE 3.2: An example of a strong CD44v6 staining in CC tissue
The scale bar at the large image equals 5 mm *and the scale bar at the zoomed image equals* 100 µm

3.2.1 Sensitivity and specificity

Both a sensitivity and specificity were calculated based on the resulting H-scores. Only one slice with CC cells (TD tissue) had an H-score of 0 which would result in a sensitivity of 0.98. However, the sensitivity of the biomarker also depends on the eventual detection sensitivity when combined with a NIR tracer. Therefore, a truncation value was based on descriptive statistics in a subgroup consisting of T, N+ and, TD tissue. The mean in this group was 126.0 with a standard deviation of 84.70, the median was 105.0, and the lower 25% percentile was 55.00. Based on this percentile the truncation value was set at an H-score of 55.00. This resulted in the sensitivities provided in Table 3.3. In tissue without CC cells, the N- tissue, no staining was seen resulting in an H-score of 0. This means no false positives were found and the specificity is 1.

TABLE 3.3: The sensitivity in different tissue groups

Sensitivity all tissue	0.792
Sensitivity in T	0.826
Sensitivity in N+	0.842
Sensitivity in TD	0.4

Figure 3.3 shows the scores in the different tissues. Figure 3.4 shows the distribution of the H-score results. This histogram and the normality test Shapiro-Wilk with a resulting P-value of 0.0136 confirm the alternative hypothesis that the data is not normally distributed which influenced the tests chosen for statistical analysis.

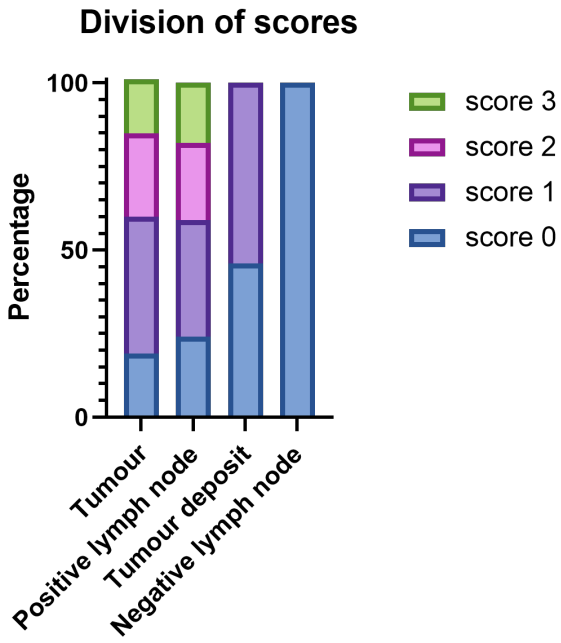

FIGURE 3.3: H-scores in different tissue

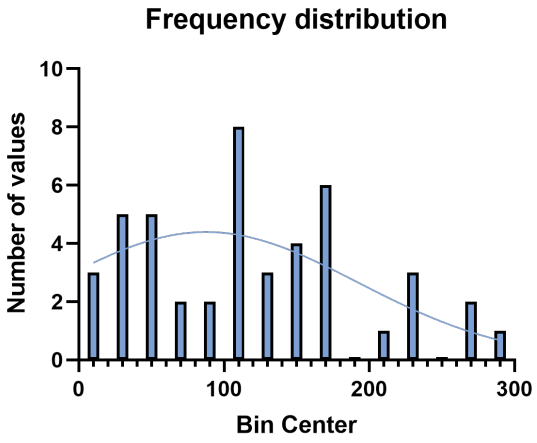

FIGURE 3.4: Histogram showing the distribution of the H-scores

3.2.2 Statistical tests

Figure 3.5 and Table 3.4 show the H-scores in the different tissues. The Kruskal-Wallis test was used to test whether the medians of the H-scores significantly differed between the tissue types. This resulted in a P-value of 0.0923 with an H of 4.765 confirming the null hypothesis, that the medians do not differ significantly.

Furthermore, the H-scores of T and N+, and T and TD were compared using a Mann-Whitney test. When comparing T and N+ the P-value was 0.9855 with a U of 227 confirming the null hypothesis that the medians do not differ significantly. When comparing T and TD however, a P-value of 0.0385 with a U of 24.50 was found, confirming the alternative hypothesis that the medians do differ significantly.

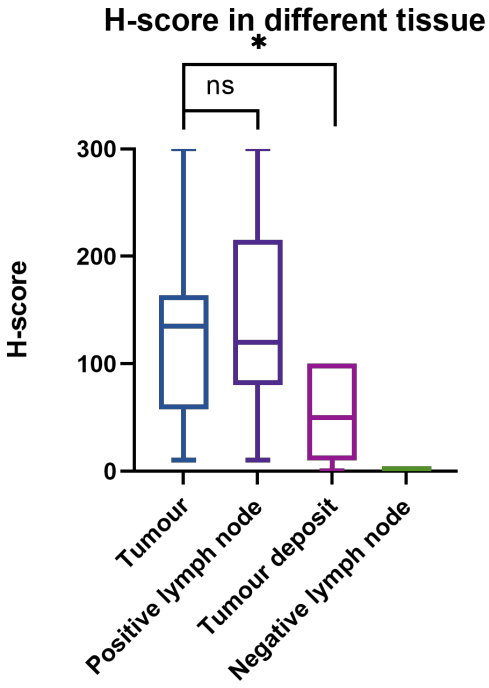

FIGURE 3.5: Distribution of H-score in different tissue types

TABLE 3.4: The descriptive statistics of the H-score in different tissue

T	mean H-score: 132.7 standard deviation: 86.53 median: 135.0
N+	mean H-score: 136.6 standard deviation: 84.18 median: 120.0
TD	mean H-score: 54.00 standard deviation: 45.61 median: 50.00
N-	mean H-score: 0.00 standard deviation: 0.00 median: 0.00

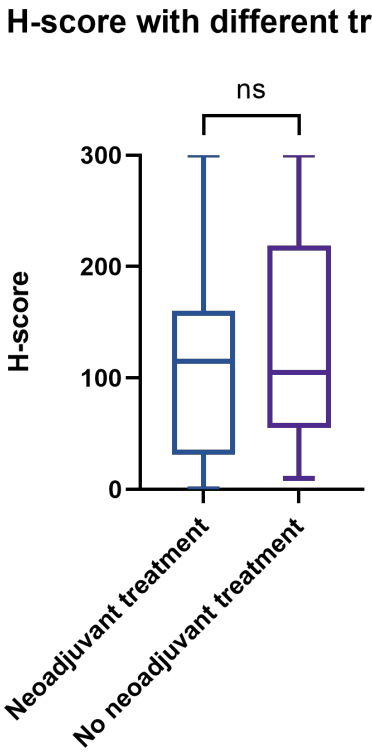

FIGURE 3.6: Distribution of H-score in neoadjuvant treatment and no neoadjuvant treatment

TABLE 3.5: The descriptive statistics of the H-score in different treatment

Neoadjuvant treatment	mean H-score: 111.6 standard deviation: 77.58 median: 115.0
No neoadjuvant treamtent	mean H-score: 133.3 standard deviation: 88.33 median: 105.0

Figure 3.6 and Table 3.5 show the results of H-score in different treatment. To test whether or not the medians of the H-scores in the two groups differed significantly the Mann-Whitney

test was performed. This resulted in a P-value of 0.5687 with a U of 229.5 confirming the null hypothesis, that the medians do not differ significantly.

Figure 3.7 and Table 3.6 show the H-scores in the different T-stages. To test whether or not the medians of the H-scores in the three groups differed significantly the Kruskal-Wallis test was performed. This resulted in a P-value of 0.2588 with an H of 2.704 confirming the null hypothesis, that the medians do not differ significantly.

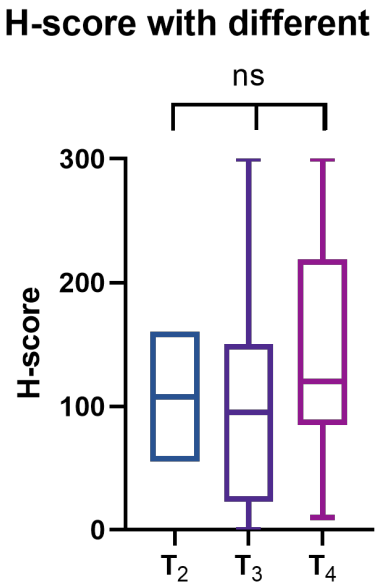

FIGURE 3.7: Distribution of H-score in different T-stages
This box and whisker plot shows the distribution of the H-score in different T-stages.

TABLE 3.6: The descriptive statistics of the H-score in different T-stages

T_2	mean H-score: 107.5 standard deviation: 60.62 median: 107.5
T_3	mean H-score: 102.5 standard deviation: 87.65 median: 95.00
T_4	mean H-score: 142.1 standard deviation: 84.64 median: 120.0

Eventually the agreement of the H-scores within one patient and for different tissue was also tested. Figure 3.8 shows the agreement between the H-scores and Table 3.7 shows the descriptive statistics of the two groups. When more than one T, N+ or TD slice was included for a patient, the one giving the smallest difference in H-score was chosen. Furthermore, one patient was excluded from this analysis since only T tissue was stained due to absence of N+ or TD. To test the agreement between the two groups the two-tailed Wilcoxon test was performed. This resulted in P-value of 0.2078 and a r of 0.7509. Therefore, the null hypothesis can be confirmed with an effective pairing, and there is no reason to assume the medians of the groups differ.

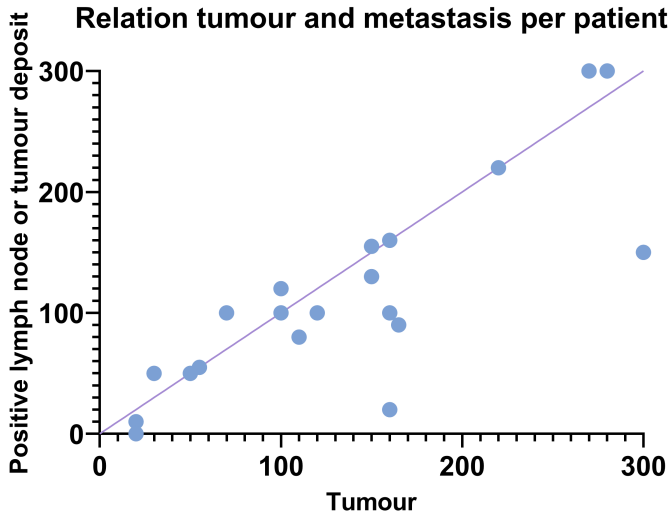

FIGURE 3.8: The agreement of the H-score within a patient
Each dot represents a patient and the H-score of the primary tumor and the 'metastasis', the N+ or TD. The closer to the purple line the more they agree.

TABLE 3.7: The H-score in tumour and in the metastases group

T	mean H-score: 134.5 standard deviation: 84.46 median: 135.00
N+ and TD	mean H-score: 114.5 standard deviation: 83.55 median: 100.0

3.2.3 Other results

Additional analysis showed not only CC cells are stained with a CD44v6 staining but also dysplastic tissue (precursor of cancer) surrounding the tumour (Figure 3.9) and in the polyp (Figure 3.10). In some slices the CD44v6 staining is also seen in stroma around the tumour cells (Figure 3.11). Other tissue that showed a strong CD44v6 staining was healthy ileum (Figure 3.12), and healthy squamous epithelium (Figure 3.13). Furthermore, the staining is very heterogeneous (Figure 3.14) which can also be seen in the deviation in the H-scores. Moreover, due to necrosis, only a minimal number of tumour cells are left in some lymph nodes which might not provide a representative image of a lymph node in early stage disease (Figure 3.15).

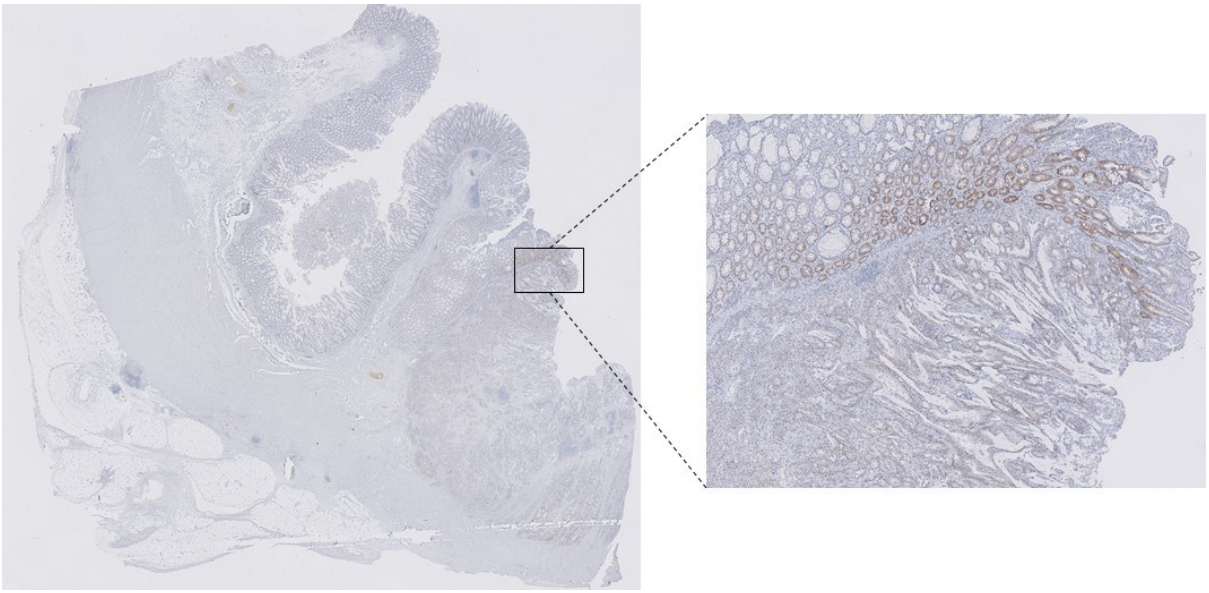

FIGURE 3.9: Staining in dysplastic tissue
This figure shows part of a tumour surrounded by dysplastic crypts. The dysplastic crypts show a 3+ score whereas the tumour tissue shows a 1+/2+ staining. The scale bar at the large image equals 5 mm *and the scale bar at the zoomed image equals* 200 µm

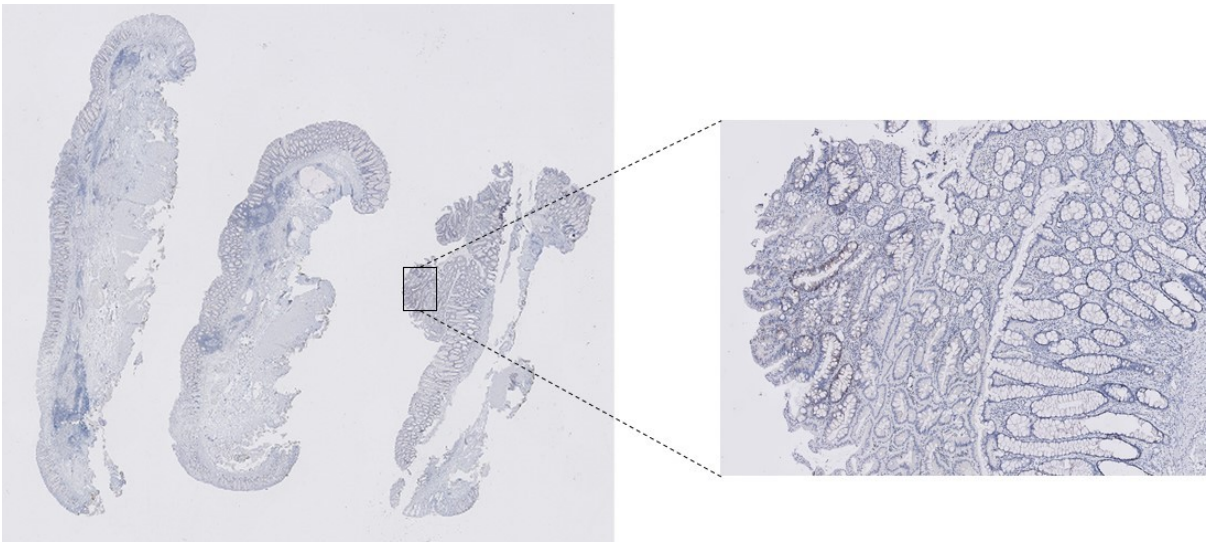

FIGURE 3.10: Staining in a polyp
This figure shows a polyp, dyplastic tissue, and a 1+ and 2+ score is seen. The scale bar at the large image equals 5 mm *and the scale bar at the zoomed image equals* 200 µm

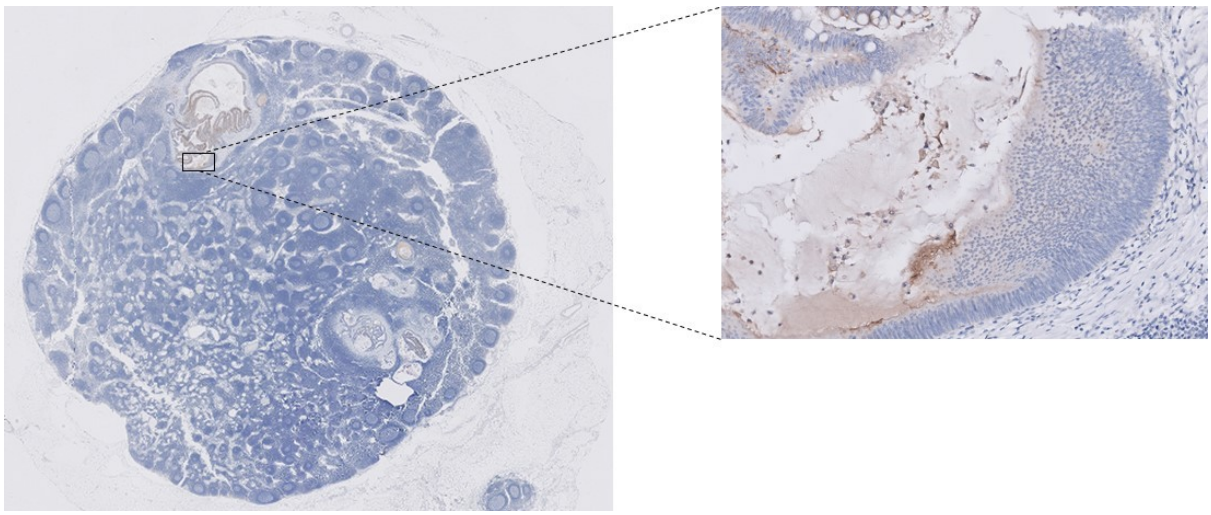

FIGURE 3.11: Staining in tumour stroma
This figure shows CC cells in a lymph node. Surrounding the cells, some stroma is stained as well. The scale bar at the large image equals 5 mm *and the scale bar at the zoomed image equals* 50 µm

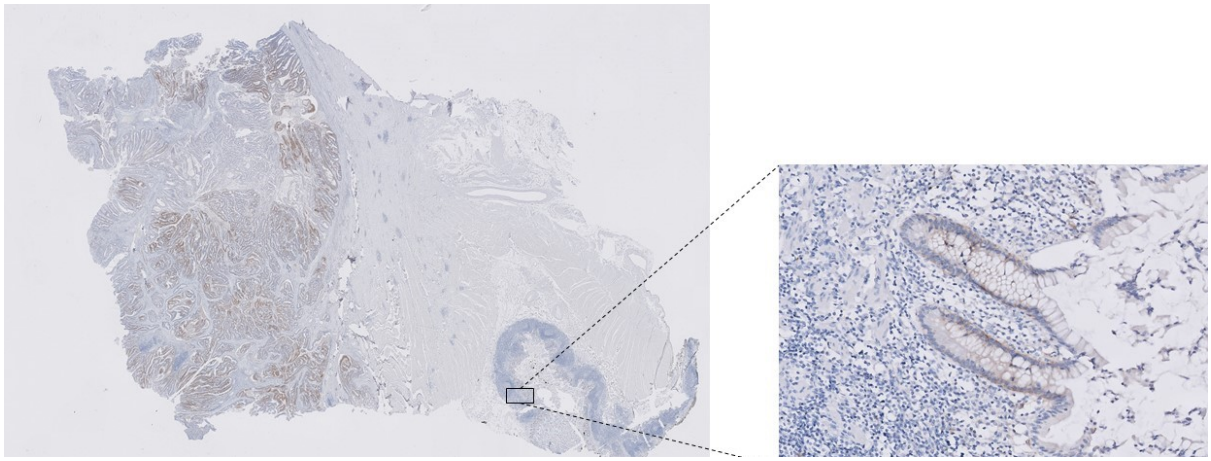

FIGURE 3.12: Staining in the ileum
This figure shows strongly stained tumour cells on the left and moderate stained ileum cells on the right. The scale bar at the large image equals 5 mm *and the scale bar at the zoomed image equals* 50 µm

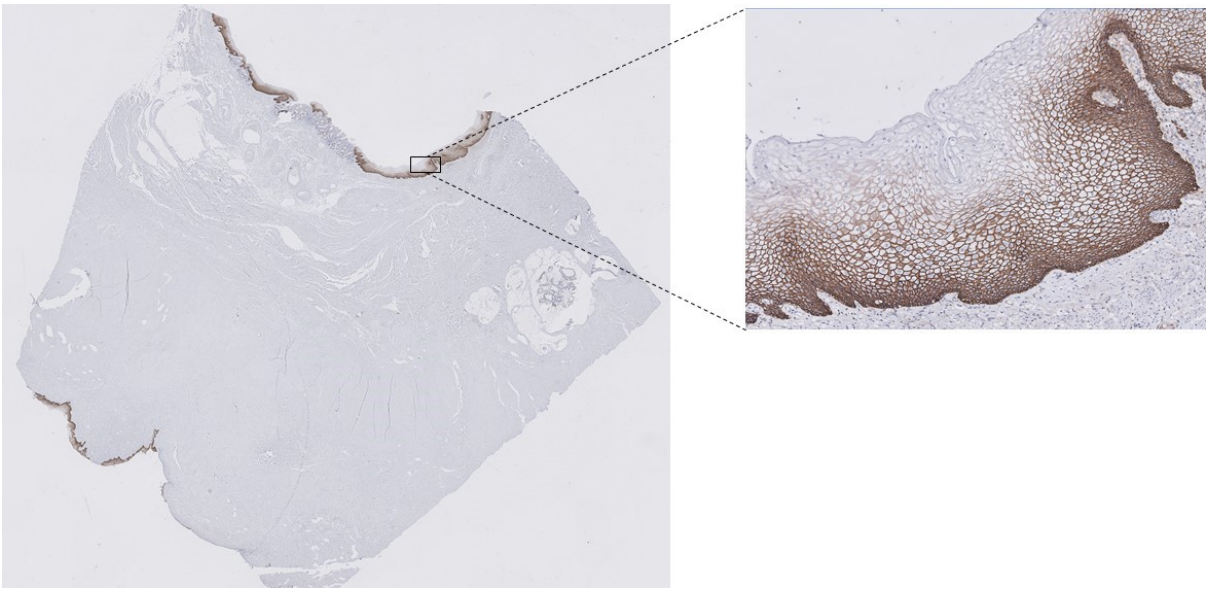

FIGURE 3.13: Staining in squamous epithelium
This figure shows strongly stained squamous epithelium near the anus. A small TD can be seen in the middle right of the image. The scale bar at the large image equals 5 mm *and the scale bar at the zoomed image equals* 100 µm

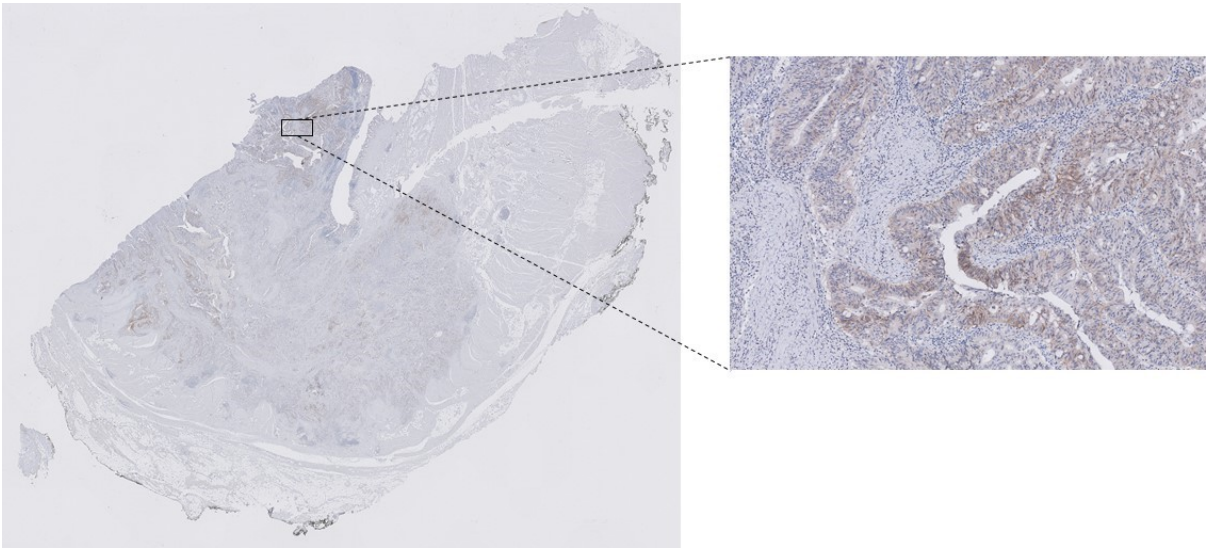

FIGURE 3.14: Heterogeneous staining
This figure shows strongly stained cells in the middle, moderately stained cells at the right, and weak stained cells at the left resulting in a heterogeneous staining. The scale bar at the large image equals 5 mm *and the scale bar at the zoomed image equals* 100 µm

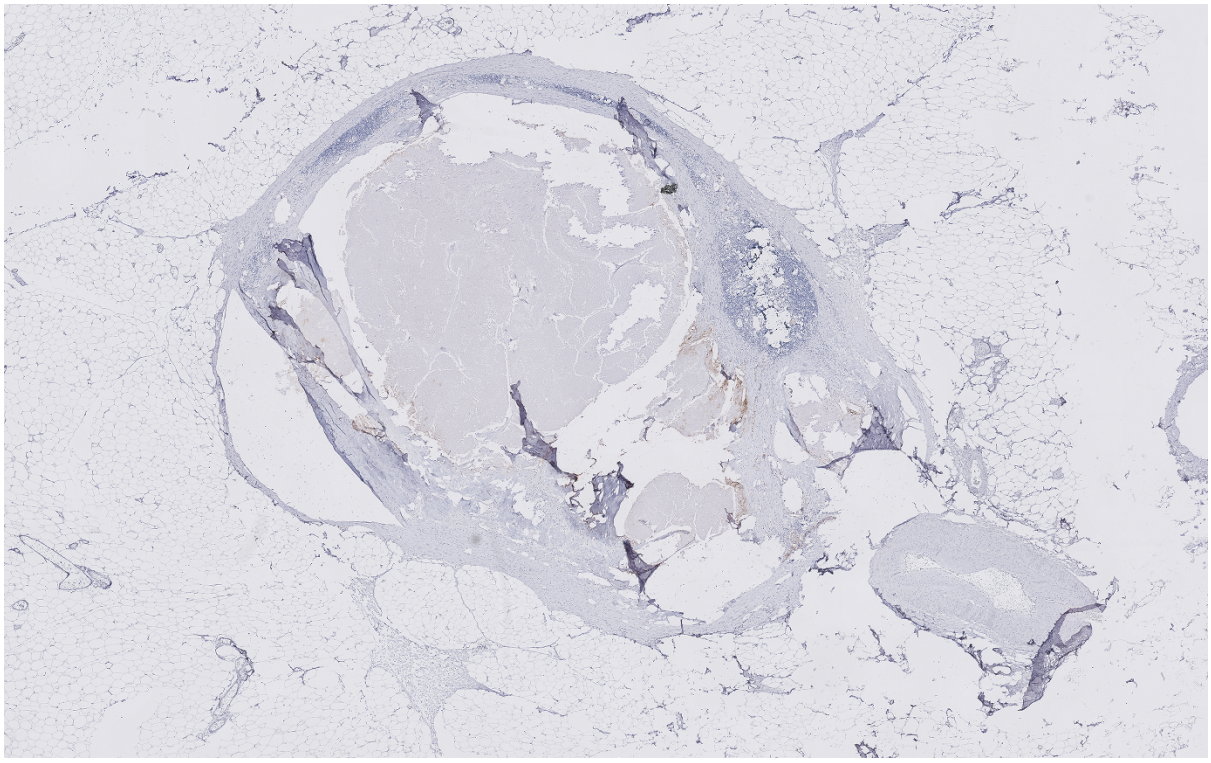

FIGURE 3.15: Lymph node with necrosis
The scale bar at the large image equals 1 mm.

3.3 Discussion

The aim of this study was to research the effectiveness of a CD44v6 targeted biomarker for the identification of early stage CC cells using IHC. An optimized staining protocol was found and T, N+, N-, and TD tissue of 21 patients was included. The results showed a high sensitivity and specificity for the use of a CD44v6 targeted biomarker in *ex vivo* identification of CC cells. Moreover, a strong correlation between the staining in T and N+ or TD within a patient was found despite the large standard deviation (84.70) in this group. Therefore, CD44v6 is a promising biomarker for *in vivo* identification of CC cells. However, TD showed a lower sensitivity, and a much lower mean H-score than T and N+, and the Mann-Whitney test showed a significant difference between the medians of the T group and the TD group. The origin of TD can be from tumour tissue growing along lymphatic or vascular structures or nerves, some of them might even be a lymph node metastases in which the pre-existing lymph node is not recognizable anymore. [69] Since both situations suggest a more advanced tumour stage it is hypothesized the H-score in TD is lower because CD44v6 expression is less outspoken in advanced stages of CC. [67] Between any other groups, no significant differences were found based on the available sample size. The H-score in all tissue groups showed a high standard deviation of 88.95, which can be explained by the large deviation in the scoring due to low scores in negative lymph nodes and high scores in positive tissue.

CD44v6 is an adhesion molecule, involved in cell-to-cell or cell-to-matrix adhesion. [70] The relation between CD44v6 and distant metastasis was first shown in pancreatic cancer which enabled to prove the higher metastatic potential, an increased resistance to anti-cancer therapy and poor survival. [67] The CD44v6 expression in CC cells has since often been researched and the expression is not restricted to solely metastatic tumors. [70] In literature both cytoplasmatic and membrane CD44v6 expression is mentioned in CC. In early stage of the disease, membrane expression of CD44v6 is more outspoken compared to later stages of the disease. [22, 70] Since the

main focus in this research was early-stage disease, membrane staining was used for scoring. In this study no cytoplasmic staining was seen without membrane staining. Moreover, some slices showed stroma staining which can be explained by the presence of CD44 isoforms in serum. [71] To demonstrate the feasibility of CD44v6 targeted imaging Hartmans *et al.* performed a study in mice where cancer cells were successfully fluorescently visualised pathing the way for clinical use of a tumour-specific tracer. [22] More tracers like these are created, for example Boonstra *et al.* also visualised CC cells in mouse, using an NIR tracer based on the carcinoembryonic antigen. [72]

3.3.1 Limitations

The sample size of this study was limited. A follow-up study with a higher sample size preferably including more T_1 and T_2 tissue since staining would be used for SLN detection in early stage disease. A different balance between early and late stage disease could increase the H-score mostly since it is known CD44v6 is more expressed in early-stage disease and there might be less necrosis in lymph nodes. [70, 73] Based on the results, the specificity of this biomarker is good. Still, in a next staining also normal healthy colon tissue will need to be stained to confirm this specificity.

Heterogeneous staining was found between and within patients which can clearly be seen in Figure 3.3 and Figure 3.14. A heterogeneous staining of CD44v6 in the primary tumor is also found in literature and explained by for example uneven distribution of malignant cells or localisation of the CD44v6 protein. Nevertheless, a less heterogeneous staining is mentioned in N+ tissue but this is not confirmed with the data found in this research since the standard deviation was comparable to T. [74] Despite positive results found in this study, this may cause difficulty in future applications since this heterogeneous H-scores may lead to difficulty in detection. If this biomarker is used for *in vivo* identification the question is whether equipment will be sensitive enough to detect these heterogeneous and possible lower H-scores. The eventual sensitivity of a CD44v6 targeted biomarker will therefore mainly depend on the sensitivity of the equipment. Moreover, Figure 3.9 and Figure 3.10 show staining in the surrounding tissue as well. Even though this might not form a problem for identification since it is tissue surrounding the tumour, it will influence the eventual tumour to background ratio. A worse tumour to background ratio decreases the sensitivity of the eventual tracer *in vivo*. Also staining in the ileum (3.12) and squamous epithelium (3.13) does not have to be a problem since this is usually not imaged when performing a hemicolectomy.

3.3.2 Clinical interpretation

The sensitivity in T and N+ is promising using a strict truncation value at an H-score of 55.00. The sensitivity is important considering the intended clinical use of identifying CC cells in a SLN and possibly basing any clinical decisions on the results found using this biomarker. The high specificity found, means no healthy lymph node is wrongly identified as a lymph node with metastasis. When N+ are identified the patient will receive adjuvant chemotherapy, therefore to prevent any unnecessary treatment the specificity is also important. [3]

Moreover, a positive relation between CD44v6-positive cells and the differentiation of the tumour exists. [75] The invasiveness of CC cells is determined by their degree of differentiation; poorly differentiated cells are more invasive. Therefore, the CD44v6 expression can also form a prognostic factor in CC. A lower CD44v6 expression therefore implies more invasive CC cells. [67] It is important however, to keep in mind that the percentage of CD44v6-positive CC cells is slightly higher in the right colon than the left, which might influence the result in a clinical setting. [76]

Furthermore, the results in this study within one patient were similar, based on the results of the Wilcoxon matched pair test, implying a tumour and corresponding lymph node within a

patient will show the same expression of CD44v6. In a clinical setting this would mean, when T can be identified using a CD44v6 targeted biomarker, so can N+. Moreover, the positive staining in the poly suggests a function for a CD44v6-targeted tracer in early-stage disease when a polypectomy suffices.

3.3.3 Future perspectives

Since the results of this study show a very high specificity and a satisfactory sensitivity a next step would be to create an *in vivo* marker. The use of this marker will enable intraoperative identification of CC cells and therewith hopefully micrometastasis in the lymph nodes. Furthermore, postoperative imaging of the tracer can help recognizing tumour borders and positive lymph nodes and potentially even make pathological analysis abundant. [72] This development may prevent a large surgical resection of the colon and the accompanied morbidity and mortality. Moreover, this CD44v6 targeted tracer is expected to increase the 5-year survival rate since the micrometastases are identified and macrometastasis is prevented. Such an *in vivo* marker could be made by combining the CD44v6 biomarker to a fluorophore. A first step in this process could be to test such a marker on tissue *ex vivo*. Ideally, the CD44v6 biomarker will be combined with a fluorescent marker which can be localized by the camera used in a surgical robot or during laparoscopy to enable minimal invasive surgery. The use of fluorescence in robot surgery has been researched already in different settings and has shown positive results in several studies. [9,77,78] The combined CD44v6-fluorophore marker could lead to a tumour-specific tracer usable for *in vivo* SLN identification.

3.4 Conclusion

Overall the results in this study showed that a CD44v6 targeted tracer is a promising marker to reliably identify CC cells with a high sensitivity and a specificity of 1. Thus pathing the way for more research and the creation of a tumour-specific tracer for *in vivo* SLN detection in colon carcinoma and therewith prognosis and clinical decision making. Nevertheless, the dataset needs to be enlarged using early-stage tumour tissue to confirm usability of this biomarker specifically in early-stage disease. Furthermore, to create a tumour specific fluorescent *in vivo* tracder, more research is needed into an applicable fluorophore and the sensitivity of the equipment.

CHAPTER 4

An ICG quantification study in patients

Currently, non-specific and receptor targeted fluorophores are being used for various clinical purposes. ICG is used in GI surgery to subjectively assess perfusion in anastomoses and specific receptor targeted fluorophores can be used for intraoperative tumor visualization. [62] This imaging modality provides the surgeon real-time visualization of the anatomical structures intraoperatively.

ICG can therefore also be used in SLN identification. A SLN biopsy with ultrastaging can contribute to an improvement of 5-year survival of patients with early-stage CC. [79] Based on prior research described in chapter 2 a novel approach for the SLN biopsy in CC is set up in the Meander Medical Center, Amersfoort which is currently researched for feasibility. During a hemicolectomy, a colonoscopy is performed while intra-abdominal access is reached with laparoscopy (Figure 4.1). The colonoscopy provides the possibility to submucosally and peritumoural inject ICG. After which the surgeon can identify the SLNs. Once the SLNs are visualized, they are resected and the specimen is sent to pathology for ultrastaging. [79] This is followed by a standard of care hemicolectomy to resect the tumour. To enlarge the sensitivity and specificity for SLN identification in CC using ICG, the ICG could be combined with a specific biomarker as described in Chapter 3.

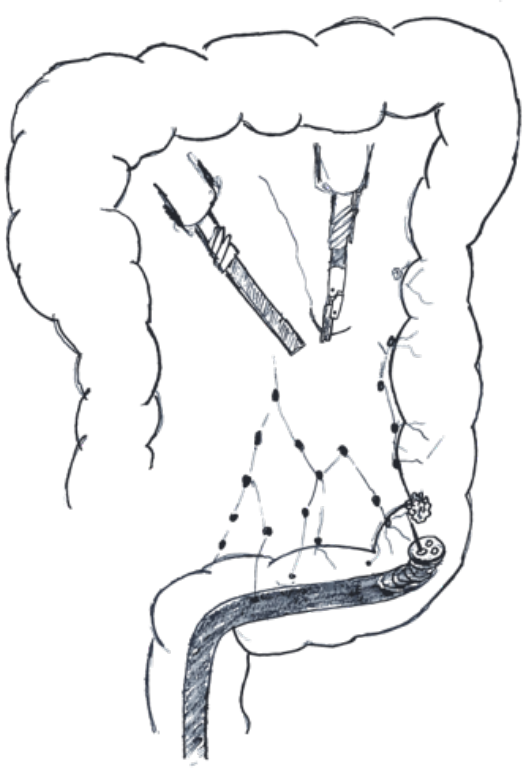

FIGURE 4.1: The novel SLN procedure
The tumour is reached using an endoscope operated by the gastroenterologist and the lymph nodes are visualized using the laparoscopic camera operated by the surgeon.

However, a drawback of this use of ICG is the subjective evaluation of the fluorescence intensity, mostly based on the visual interpretation of the clinician, making it impossible to compare between patients or base any objective clinical decisions. [63, 80] Small changes in the fluorescence intensity can be difficult to detect by visual observation. [81] Therefore an objective evaluation could be a solution. The aim of this research was to construct a reliable segmentation and objective quantification method of the SLN in operative footage.

4.1 Methods

Patients who received CC surgery based on the novel approach for SLN identification were included between September and November 2020 in the Meander Medical Center. The patients were eighteen years or older and CC was pathologically confirmed. The exclusion criteria were distant metastasis, gross lymph node involvement or pre-operative suspicion of a T3-T4 tumour. The here described research was done together with two other students.

4.1.1 Data analysis

The surgery was recorded using RVC Clinical Assistant (RVC Medical IT B.V., Amersfoort, The Netherlands) connected to the Da Vinci surgical robot. The fluorescent signal was captured using the Firefly of the Da Vinci Xi surgical robot from Intuitive (Sunnyvale, California, USA) which was calibrated for the use of ICG with an excitation wavelength of 805 nm, visualization at

700 nm to 815 nm and a laser light as excitation source. [82,83] This endoscope has a chip-on-a-tip arrangement with the camera located inside the the body. [84]

The basic way of representing a digital image is in rows of pixels resulting in 2D images. Each pixel has a particular value representing a colour or grey intensity enabling image processing. [85] Image processing is also possible in videos since this is simply many of these images, referred to as frames, shown in a fast and logical order. Preprocessing of the videos was performed using Video Editor (Microsoft, Redmond, USA) with no loss of resolution, to trim the videos with only ICG. Every tenth frame of a patient was included resulting in three frames per second. The image processing was done using Python version 3.8 (Python Software Foundation, Beaverton, USA). Segmentation was done in the hue, value and saturation (HSV) colour space (Figure 4.2). [86, 87] The often used red, green and blue (RGB) colour space, where colours are defined only by the percentage of red, green, and blue, can be highly influenced by reflection. In the RGB colour space, illumination cannot be separated from the pixel values whereas, this is possible in the HSV colour space by using V and S. Segmentation using the HSV colour space will therefore provide better results in this research. [88]

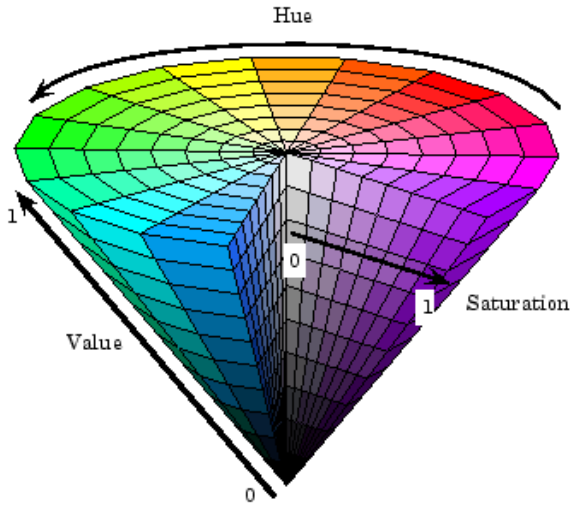

FIGURE 4.2: HSV colour space
The H corresponds to the colour on the wheel defined as an angle in the range $0 - 2\pi$. When H increases the colour changes from red to orange and eventually returns to red. The S indicates the amount of saturation. 0 corresponds to shades of grey whereas 1 resembles fully saturated colours with no white. The V corresponds to the brightness of the colour, the brighter the colour the closer to 1. [86]

Eventually, segmentation was performed using thresholding, creating a binary mask. Pixels within the region of interest (ROI) (fluorescent area) have values of 1 and outside of the ROI have values of 0. The thresholds were based on 3D scatter plots showing the color distribution within a frame and were determined individually and manually for each patient. The green pixels corresponding to the ICG were localised. Reflection of light is automatically ruled out since this falls out of the threshold range. By imposing the binary mask on the original image, the ROI is segmented. Using morphological operations the mask is optimised. Eventually, the pixel intensity was measured in a gray value image.

4.2 Results

For this research two patients were included. Their characteristics can be found in Table 4.1 the body mass index is categorised by the standards of the World Health Organization [89], and the ASA classification is based on the American Society of Anesthesiologists [90]. The TNM stadium is the preoperative stadium.

TABLE 4.1: Patients characteristics

	Gender	**Age group**	**body mass index**	**ASA classification**	**TNM stadium**
Patient 1	Male	60-69	Pre-obesity	II	T_1N_0
Patient 2	Male	80-89	normal weight	III	T_2N_0

The segmentation was based on 3D scatter plots of the pixel intensities within a frame, an example of a frame and the corresponding 3D scatter plot can be found in figures 4.4 and 4.3. The eventual segmentation of a lymph vessel and lymph node in patient 1 are shown in Figures 4.5, 4.6, 4.7 and 4.8. A mean intensity over time for the SLN and lymph vessel was calculated on a scale from $0 - 1$ and can be found in Table 4.2.

FIGURE 4.3: Frame of patient 2 used for 3D scatter plot

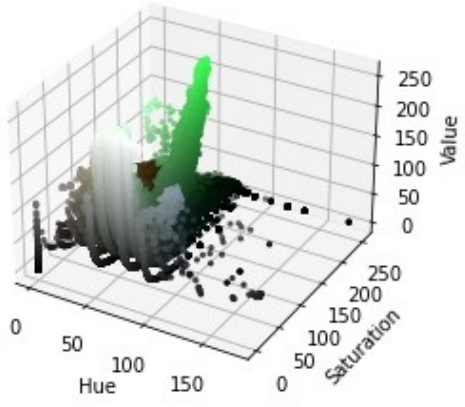

FIGURE 4.4: 3D scatter plot in the HSV colour space
This plot is based on a frame from patient 2. The green pixels are grouped together and can therefore easily be segmented.

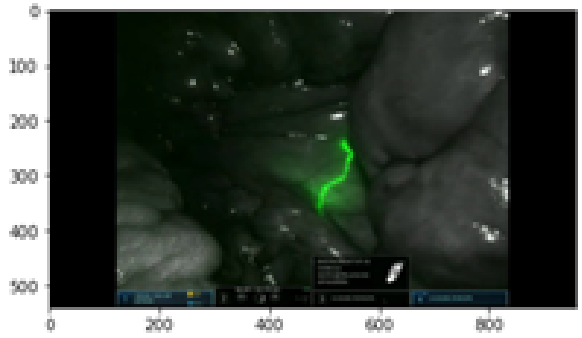

FIGURE 4.5: Imaging of lymph vessel using ICG in patient 1

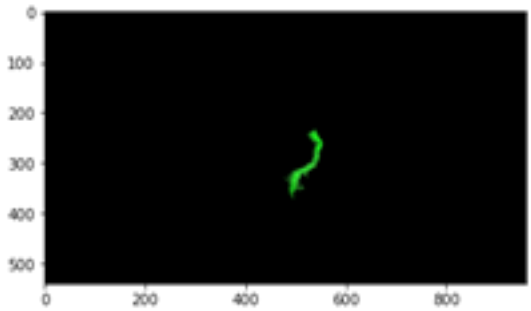

FIGURE 4.6: The lymph vessel segmented in patient 1

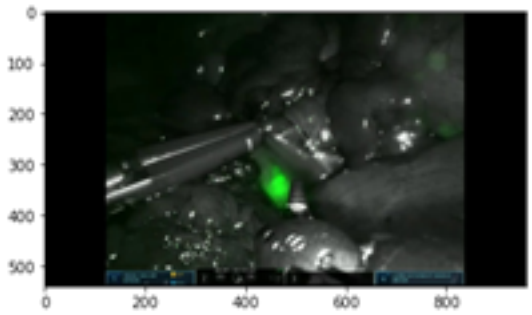

FIGURE 4.7: Imaging of lymph node using ICG in patient 1

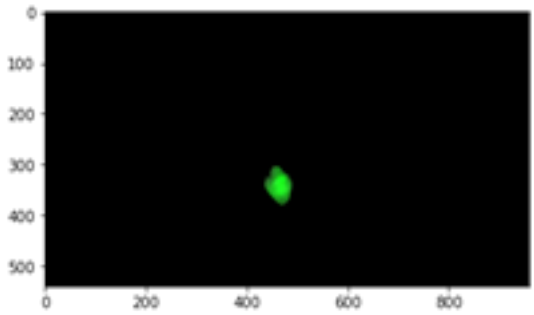

FIGURE 4.8: The lymph node segmented in patient 1

TABLE 4.2: The mean fluorescence intensity in the lymph nodes

	Mean pixel intensity - node (AU)
Patient 1	0.4039
Patient 2	0.4561

4.3 Discussion

In this study, a reliable segmentation and quantification method was set up for SLN identification using ICG therewith providing possibilities for CC cell identification using a specific NIR tracer based on CD44v6 as described in chapter 3. Fluorescence imaging is increasingly used to estimate, for example, bowel perfusion but difficult to interpret objectively making comparison between patients difficult and the here described method shows no exception. [63, 80, 91] Simultaneously to the research described here, Inge van den Berg and I, did research into patient characteristics influencing the pixel intensity in bowel perfusion. [81] The same method as described in this research was used, except patients included were patients undergoing anastomosis surgery. Multiple linear regression was performed to analyse the correlation of patient characteristics and the mean intensity. Intensity curves were created and an increase was seen over time which can be explained by the inflow of blood. Nevertheless, variations seen after this increase are most likely explained by movements of the camera which is in line with this research and literature. [92] A literature review by Van den Bos *et al.* also mentions patient specific factors that influence the measured fluorescence intensity one of them was BMI.Therefore they advise to use a weight-adjusted dosage especially in overweight patients. [92] In 2015, Protyniak *et al.* performed a study using the absolute fluorescence intensity recorded by the camera system, which was compared to a reference intensity in for example the small bowel. Even though other variables such as distance or angle were not mentioned in this research, it is believed to be an objective manner to quantify the ICG but mostly assesses the blood flow. [63]

In 2018, Koch *et al.* looked into standardization of the parameters in Table 2.3 and reversion to correct for the effects of those same parameters. Despite positive findings, accounting for the parameters and therewith comparison between different camera's, is a complex process. Real-time measurements and fast processing methods to correct the raw fluorescence images are required. Above all, many of the quantification studies performed at this moment concentrate on anastomoses assessment. They look into, for example, the intensity of the fluorescence over time. [80, 91, 93] However, in this research lymph vessels are imaged for SLN mapping and the time to reach the maximum fluorescence intensity is considered as irrelevant.

4.3.1 Limitations

A large limitation in this research was the impossibility of comparing the patients which is, among others, caused by a non-standardised measurement. The pixel intensity is influenced by camera distance and orientation, meaning for as long as there is no correction or standardisation, objective quantification and clinical decision making cannot be done. Next to this, fluorescence is influenced by exposure time. A longer exposure time increases the fluorescence signal but may also increase the noise. [94] The exposure time in the Firefly Xi is set automatically therefore this might change with every frame making the intensities unreliable. In addition, ICG might not be the most optimal tracer for SLN biopsy since it has a small hydrodynamic diameter which permits flow through the SLN to further lymph nodes. The combination of ICG and human serum albumin prevents fast and easy passage to next lymph nodes. [37]

When applying the novel SLN procedure as described in this chapter, there are some clinical aspects decreasing the success rate of SLN identification. These are inadequate concentrations of ICG, the Indian ink injected preoperatively to identify the tumour and inflammation around the tumour from this injection, large tumour size, drainage to adjacent lymphatic vessels, and the use of a rigid needle. [36, 78] In addition, the fluorescence penetration depth of ICG is only up to about 1.5 cm, which might make the SLN identification even more difficult when situated deeper in the tissue. [95] Nevertheless, the lymph nodes in the mesenterium are usually located superficial and up until now no difficulties were experienced in detecting a lymph node during the feasibility study in the Meander Medical Center. A solution to this limited penetration depth could be a combination with a gamma emitting tracer, such as Tc99m-nanocolloid, for intraoperative guidance. [96] This also provides the opportunity to make preoperative scans to make localisation easier.

4.3.2 Clincal implementation & future perspectives

In a clinical setting, when real-time quantification is possible and ICG or another fluorophore is combined with a sensitive and specific biomarker, like CD44v6, intraoperative staging and prognosis of the disease based on the described segmentation and quantification might be possible. Nevertheless, it is known that the pixel intensity is influenced by a lot of factors as shown in Table 2.3 and by the research by Inge van den Berg, therefore making comparison between patients difficult. [24] A standardisation or correction is necessary to be able to base any clinical decisions on the absolute pixel intensity. Possibilities for standardisation could be a standardised camera position by using a sterile dark coloured ruler. Chapter 5 of this thesis, the phantom study, makes a beginning with a correction analysis. Another option would be to calculate the distance using triangulation which could be possible using the Da Vinci surgical robot since it uses a stereo endoscope. Moreover, several studies have set up trials using fiber-optic spectroscopy *in vivo* to quantify the fluorescence. [97] Using spectroscopy, the fluorescent signal can be accurately quantified by correcting for tissue properties such as absorption and scattering. [98, 99]

Furthermore, when the intensity can be assessed objectively and a sensitive and specific biomarker is used to identify CC cells, a next step would be to correlate the clinical outcome to the intensity found in the SLN. Additionally, object to background ratio can be calculated. A low value for this ratio implies that the camera needs to have a high sensitivity. [96] Nerup *et al.* also performed a quantification study in bowel perfusion where they considered the background intensity. The eventual intensity was then corrected using the background intensity to account for any background signal that the camera might have picked up. [80] Moreover, the research of Inge van den Berg suggested to look into more patient specific characteristics which may influence the optical properties. [81] Currently, research is continuing and looking into the correlation with comorbidities, time between injection and first fluorescence, blood pressure, and the possibilities for standardisation. Moreover, manually setting a threshold in each patient is not feasible for future application, which is also why automatic thresholding is currently researched.

4.4 Conclusion

This research described a segmentation and quantification method for SLN identification using ICG. Segmentation based on thresholding in the HSV colour space allows quantification of the fluorescence intensity in the identified SLN and can be used to enhance the novel approach for SLN identification in CC. Clinical interpretation of the fluorescence intensity depends on future research into correction and standardisation of the fluorescence intensity measurements and influencing variables.

CHAPTER 5

A fluorescence intensity phantom study

As previously described in paragraph 2.6.1 and showed in chapter 4, the fluorescence intensity on screen depends on many variables and the degree of fluorescence is easily over- or underestimated. [24, 60] During surgery some of the most basic variables are a changing distance, orientation and field of view (FOV). Fluorescence can be detected with different NIR camera's, such as the Firefly of the Da Vinci Xi surgical robot. The new approach for SLN identification in CC, which is fully described in chapter 4, is initially set up using the Firefly Xi. Therefore, the Firefly Xi will be used as NIR camera in this research. The Firefly Xi only provides two modes: white light and processed fluorescence imaging. [84] Figure 5.1 shows the excitation spectrum of the white light and the NIR light used in the Firefly Xi.

Earlier publications about fluorescence phantoms, quantification, and influencing variables are widely available for example distance is known to influence the intensity based on the inverse-square law for a point source. [100] Nevertheless, studies concerning the use of the Firefly, ICG, and the fluorescence intensity on screen are very scarce. [62, 84, 96, 101–104]

It is important to know how the variables influence the fluorescence intensity to be able to compare different patients and outcomes but mainly to base solid objective clinical decisions on the fluorescence intensity. [11, 91] Which is one of the reasons Koch *et al.* suggest to create a standard phantom to enable comparison of cameras. [24] Almarhaby *et al.* [96] described a phantom study evaluating a novel camera system. Lypmh node phantoms to simulate metastases and tissue-like layers were used to evaluate the detection capability. Phantoms they used were made of acrylic glass with wells in different diameters and filled up with a fluorophore in different concentrations to simulate lymph nodes. A signal to noise ratio was found for each concentration of ICG and peaked at 10 µM. In this partial aim of this master thesis a phantom study based on the research by Almarhaby *et al.* [96] was set up to explore how distance, orientation, concentration, and FOV influence the fluorescence intensity on screen and the possibilities for correction of these variables when using the Firefly Xi. Based on expert opinion, the hypothesis was that the software would apply adaptive intensity, normalize the intensity in such a way that the signal to background ratio is as high as possible, since this improves the detection possibilities. However, it makes comparison between patients, or in this case phantoms, difficult. [82]

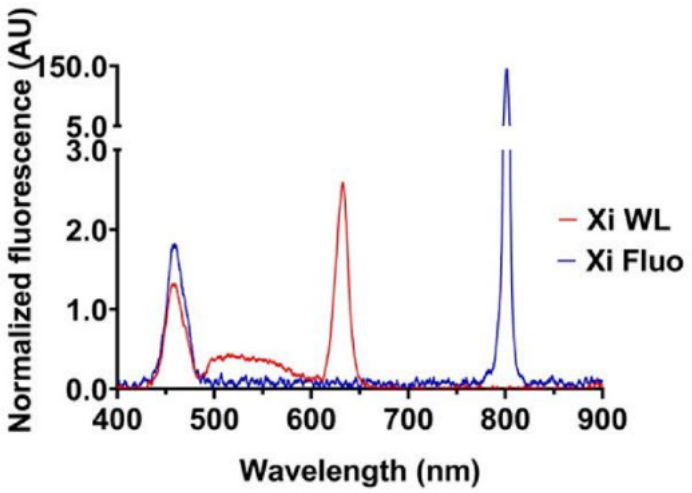

FIGURE 5.1: The spectral properties of the Firefly Xi
White light mode (WL) in red and the Fluorescence mode (Fluo) in blue. The blue line shows a clear excitation peak at the excitation wave length of ICG [84]

5.1 Methods

To create a usable phantom, several approaches were tried. Firstly, a hand painted black matt 96-well plate was used, painted to minimise reflection. ICG (VERDYE, Diagnostic Green GmbH, Ascheim-Dornach, Germany) was diluted in a natrium chloride solution in concentrations including the optimal concentration of 10 µM. This phantom will be further referred to as phantom 1. A second set of phantoms was made using agar-agar (3%) to create more scattering and absorption. [96] Different forms of objects, solvents, and concentrations were used. The solvents were phosphate-buffered saline (PBS), dimethyl sulfoxide (DMSO) a clear liquid, methanol known to induce fluorescence, and fetal calf serum (FCS) since ICG is known to bind to plasma proteins which induce fluorescence. [105] These phantoms will be further referred to as phantoms 2. A third set of phantoms consisted of Eppendorf tubes filled with different concentrations of ICG diluted in PBS, intralipid known to induce scattering similar to human tissue, and Indian ink simulating absorption similar to human blood. [102] These phantoms will be further referred to as phantoms 3.

5.1.1 Measurements

The variables investigated in this study were the orientation (α) in degrees (°), the camera distance (d) in cm, the concentration of ICG (β) in µM, and the difference in pixel intensity within the FOV. This was done using three different measurements:

1. A dynamical measurement, where the phantom was moved through the FOV from left to right with an unknown pace.

2. FOV measurements, where the phantom was positioned statically in sixteen different parts of the FOV.

3. Static measurements where the height was altered using black matt painted wooden blocks of 1.5 cm and the orientation using black matt painted wedges of 8° (Figure 5.2 and 5.3). These measurements also enable investigation of the inverse-sqaure law and if the Firefly Xi follows this law.

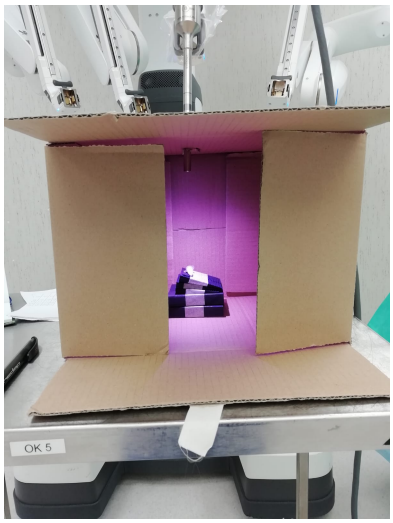

FIGURE 5.2: A close-up of the setup
The blocks and wedges can clearly be seen in this example.

FIGURE 5.3: A close-up of the setup, orientation of the phantom

FIGURE 5.4: The experimental setup
The box was used to minimize the influence of the ambient light. The third arm of the Da Vinci robot was used to ensure a stable camera position.

A photograph of the phantom taken using the Firefly Xi with a 30°endoscope, was downloaded as a $u \times v \times w$ matrix with $u = 1080$, $v = 1920$, and $w = 3$ in unsigned eight bit integer (uint8) and RGB colour space through RVC Clinical Assistant and not directly from the Da Vinci. The eventual setup during data acquisition can be seen in Figure 5.4. To minimise the influence of the 30°angle of the endoscope, the endoscope was positioned in such a way that the angle was as close to 0° as possible.

5.1.2 Analysis

MATLAB 2019b (The MathWorks, Natick, Massachusetts, USA) was used to process the data. First, a ROI was selected in each image or video frame through segmentation after which an average pixel intensity was calculated in this ROI. Two manners were used for segmentation. In measurements 1 and 2 a white background and software induced objects (Figure 5.6) made that the segmentation was most successful in HSV colour space. The process can be seen in Figure 5.5. The mask used for segmentation in measurements 1 and 2 is described in Algorithm 1 and 2, the values for segmentation are based on the report by Inge van den Berg. [81]

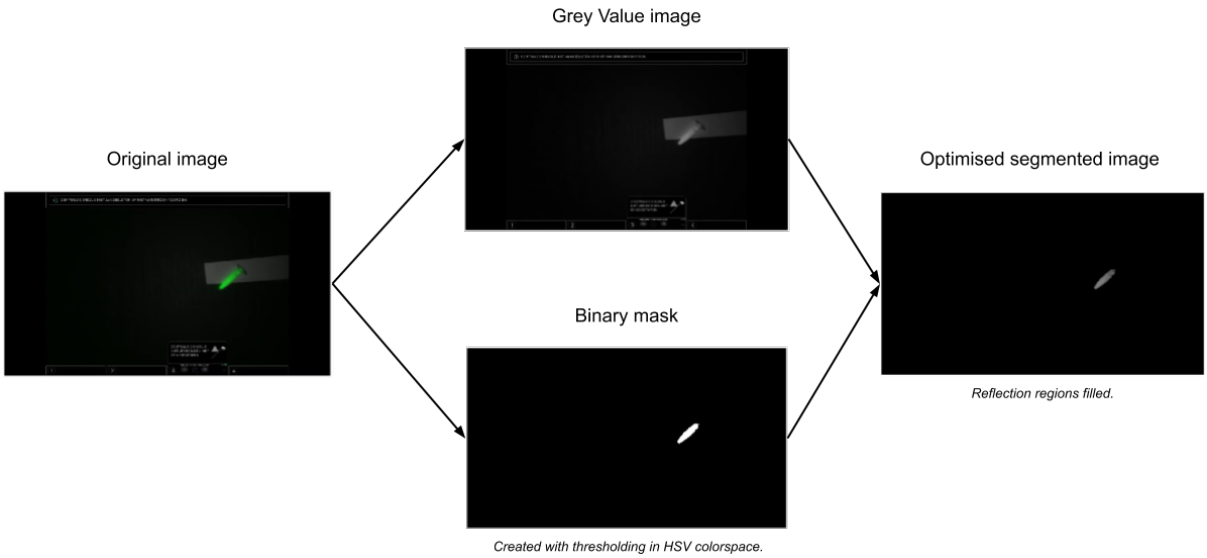

FIGURE 5.5: Flowchart for ROI selection in measurement 1 and 2
This flowchart shows the process of the ROI selection in the images or movie frames of the dynamic and FOV measurements. This is done with segmentation by thresholding in an HSV image and multiplying the grey value image with the binary mask to create the segmentation.

FIGURE 5.6: Resulting image of measurement 2
This image is an example of an image taken during measurement 2 and shows the objects added by the software. The ROI is found at the top of the image and shows collision with one of these objects.

Algorithm 1 Creating the HSV image (**k**(u',v',w')) [106]

Input: $\mathbf{F}(u, v, w) \rightarrow$ *RGB-image of the phantom, a 2D matrix stored in uint8, with* $u = 1080, v = 1920,$ *and* $w = 3$.

Output: $\mathbf{K}(u', v', w') \rightarrow$ *HSV image of the phantom, a 2D matrix stored in double precision.*

initialization:

1: *Rescaled image* $\mathbf{G}(u, v, w) \leftarrow$ *Rescale indices in* $\mathbf{F}$ *from* $1 - 256$ *to* $0 - 1$.

2: $C_{max_{u,v}} \leftarrow max(\mathbf{L}_{1...u,1...v,1}; \mathbf{L}_{1...u,1...v,2}; \mathbf{L}_{1...u,1...v,3})$

3: $C_{min_{u,v}} \leftarrow min(\mathbf{L}_{1...u,1...v,1}; \mathbf{L}_{1...u,1...v,2}; \mathbf{L}_{1...u,1...v,3})$

4: $\Delta_{u,v} \leftarrow C_{max_{u,v}} - C_{min_{u,v}}$

5: **for** $\mathbf{K}(u', v', 1)$

if $\Delta = 0$ **then** $\mathbf{K}(u', v', 1) \rightarrow 0°$

elseif $C_{max_{u,v}} = \mathbf{G}(u, v, 1)$ **then** $\mathbf{K}(u', v', 1) \rightarrow 60° \times (\frac{\mathbf{G}(u,v,2) - \mathbf{G}(u,v,3)}{\Delta} mod 6)$

elseif $C_{max_{u,v}} = \mathbf{G}(u, v, 2)$ **then** $\mathbf{K}(u', v', 1) \rightarrow 60° \times (\frac{\mathbf{G}(u,v,3) - \mathbf{G}(u,v,2)}{\Delta} + 2)$

elseif $C_{max_{u,v}} = \mathbf{G}(u, v, 3)$ **then** $\mathbf{K}(u', v', 1) \rightarrow 60° \times (\frac{\mathbf{G}(u,v,3) - \mathbf{G}(u,v,2)}{\Delta} + 4)$

end

6: **for** $\mathbf{K}(u', v', 2)$

if $C_{max_{u,v}} = 0$ **then** $\mathbf{K}(u', v', 1) \rightarrow 0$

if $C_{max_{u,v} \neq 0}$ **then** $\mathbf{K}(u', v', 1) \rightarrow \frac{\Delta}{C_{max}}$

7: $\mathbf{K}(u', v', 3) \rightarrow C_{max_{u,v}}$

End

Algorithm 2 Creating a binary mask (**H**(u,v)) using HSV colour space.

Input: $\mathbf{K}(u, v, w) \rightarrow$ *HSV-image of the phantom, a 2D matrix stored in double precision with* $u = 1080, v = 1920,$ *and* $w = 3$

Output: $\mathbf{H}(u, v) \rightarrow$ *Binary mask, a 2D logical matrix.*

initialization:

1: $\mathbf{H}(u, v) \leftarrow$ *Hue* > 0.25 *and Saturation* > 0.2 *and Value* > 0.11 *in* $\mathbf{K}$.

End

Segmentation in measurement 3 can be seen in Figure 5.7 and was done as follows: the selected image or frame was changed to a double precision grey scale image. Algorithm 3 explains the image acquisition framework. ROIs were created on these images using a binary mask by employing Otsu's method [107] for automatic image thresholding in a grey value image for the static measurements (Algorithm 4). The mask was optimized using a morphological operation to remove connected components with a small number of pixels. The influence of light reflection was minimized by deleting the top 1% non-zero elements in a matrix. The deleted pixels were filled using region filling where the algorithm smoothly interpolates inward starting at the pixel values on the boundary of the specified region.

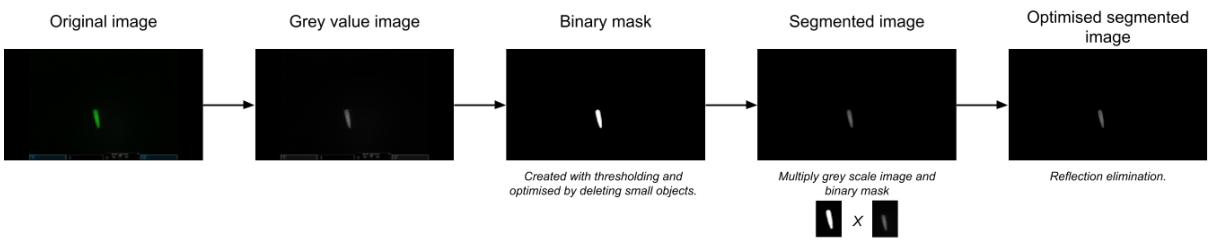

FIGURE 5.7: Flowchart for ROI selection in measurement 3
This flowchart shows the process of the ROI selection in the static measurements images. This is done with segmentation by thresholding in a gray value image.

Algorithm 3 Creating the grayscale image (**I**(u',v'))

Input: $\mathbf{F}(u, v, w) \rightarrow$ *RGB-image of the phantom, a 2D matrix stored in uint8, with* $u = 1080, v = 1920,$ *and* $w = 3$.
Output: $\mathbf{I}(u', v') \rightarrow$ *Grayscale image of the phantom, a 2D matrix stored in double precision.*
initialization:

1: *Rescaled image* $\mathbf{G}(u, v, w) \leftarrow$ *Rescale indices in* $\mathbf{F}$ *from* $1 - 256$ *to* $0 - 1$.
2: $\mathbf{K}(u', v', w') \leftarrow$ *Convert RGB-image* ($\mathbf{F}$) *to HSV-image.*
3: $\mathbf{I}(u', v') \rightarrow$ *Eliminate hue and saturation in* $\mathbf{K}$ *and stored in* ***I****(u',v')*

End

Algorithm 4 Creating a binary mask (**H**(u,v)) using (**I**(u',v'))

Input: $\mathbf{I}(u', v') \rightarrow$ *Grayscale image of the phantom, a 2D matrix stored double precision with* $u = 1080$ *and* $v = 1920$.
$N = 2073600$ *the total number of pixels.*
p *a pixel value within a range of* $0 - 1$.
T *an adaptive threshold to divide pixels in two logical groups based on* p.
Output: $\mathbf{H}(u, v) \rightarrow$ *Binary mask, a 2D logical matrix.*
initialization:

1: $C_1[n_{p_{min}}, ..., n_T]$ *and* $C_2[n_{T+(1 \div N)}, ..., n_{p_{max}}] \leftarrow$ *Divide N in two classes based on pixel value (p) and threshold (T)*
2: $\overline{n_{1,2}} \rightarrow$ *Calculate mean in* C_1 *and* C_2.
3: $\sigma^2_{C_1}, \sigma^2_{C_2} \rightarrow$ *Calculate variance of both classes* $\sqrt{\Sigma_{i=1}^{N_{C_{1,2}}}(n_i + \overline{n_{1,2}})^2/(N_{C_{1,2}} - 1)}$
4: $\omega \rightarrow \sigma^2_{C_1} + \sigma^2_{C_2}$, *calculate intra-class variance, in pixel intensity of the two classes.*
5: $T_{opt} \leftarrow$ *Repeat (1), (2), (3) and (4) until a minimal value of* ω *is found and a corresponding value for T.*
6: $\mathbf{H}(u, v) \rightarrow$ *Group pixels in two logical classes* $C_1[n_{p_{min}}, ..., n_{T_{opt}}]$ *and* $C_2[n_{T_{opt}+(1 \div N)}, ..., n_{p_{max}}]$

End

Once these ROIs were selected, the average pixel values per ROI were calculated (Algorithm 5). The absolute pixel value in an ROI was used as the fluorescence intensity in that frame. Since the aim of this research was to look into the change of intensity and not the sensitivity of the camera, the signal to noise ratio, contrast to noise ratio or any other similar variables were not taken into account. Using the found intensities in the static measurements, the Pearson correlation coefficient was calculated for d, β, and α to investigate a linear relationship between the variables and the fluorescence intensity.

Algorithm 5 Select ROIs and calculate average pixel value.

Input: $\mathbf{H}(u, v) \rightarrow$ *Binary mask, a 2D logical matrix with* $u = 1080$ *and* $v = 1920$.
$\mathbf{I}(u, v) \rightarrow$ *Grayscale image of the phantom, a 2D matrix stored in double precision.*
$\mathbf{J}(u, v) \leftarrow$ *Grayscale image of the phantom with all pixels outside of ROI at a value of* 0*, a 2D matrix stored in double precision.* **Output:** $\gamma_{roi} \rightarrow$ *Average pixel value per ROI*
initialization:

1: $\mathbf{J}(u, v) \leftarrow \mathbf{H}_{1...u,1...v} \times \mathbf{I}_{1...u,1...v} = \mathbf{J}_{1...u,1...v}$
2: $\gamma_{roi} \rightarrow$ *for* $1 : u$ *and* $1 : v$ *calculate average in* $\mathbf{J}_{u,v}$

End

5.2 Results

Figure 5.8 shows phantom 1 photographed using the Firefly Xi. Due to reflection and invisibility of the ICG this phantom was not used for measurements. Figure 5.9 and 5.10 show a selection of phantoms 2 in white light and in NIR light. Figure 5.11 and 5.12 show no fluorescence which is why phantoms 2 were also not used for measurements.

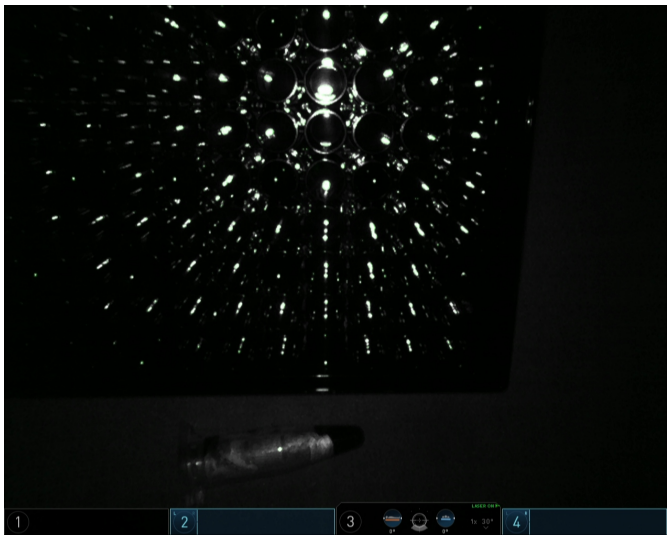

FIGURE 5.8: Phantom 1 using 96-well plate
The first phantom that was created. Due to the solvent and the reflection this phantom was not usable.

TABLE 5.1: The different concentrations used in Phantom 1

Solution	Concentration
Solution 1	2.5 µM
Solution 2	5.1 µM
Solution 3	10.2 µM
Solution 4	20.3 µM
Solution 5	40.7 µM
Solution 6	81.4 µM
Solution 7	161.8 µM
Solution 8	323.0 µM
Solution 9	646.0 µM
Solution 10	1292.0 µM

FIGURE 5.9: Phantoms 2: Spherical agar-agar phantom in white light
The ICG was dissolved in PBS and buried 2.4 cm *below the surface of the phantom.*

FIGURE 5.10: Phantoms 2: Rectangular agar-agar phantom in white light
The ICG was dissolved in DMSO and buried 1.4 cm *below the surface of the phantom. Different concentrations were buried in this phantom. From left to right and top to bottom this was: pure dissolvent,* 807.5 µM, 201.9 µM, 50.5 µM, 12.6 µM *and* 3.2 µM.

FIGURE 5.11: Phantoms 2: Spherical agar-agar phantom using the Firefly Xi
No fluorescence is seen.

FIGURE 5.12: Phantoms 2: Rectangular agar-agar phantom using the Firefly Xi
This figure shows the rectangular phantom with ICG dissolved in DMSO using the NIR light of the Firefly Xi. No fluorescence is seen only some reflection.

5.2.1 Phantoms used for measurements

Figure 5.13 and 5.14 show an example of phantoms 3 (with ICG, PBS, 2% intralipid and 0.1% or 0.2% Indian ink) which was eventually used for the measurements. Within this group only the phantoms without Indian ink were used since no fluorescence was seen using the ones with Indian ink. Table 5.2 shows the different concentrations, distances, and orientations used. This combination of variables led to sixteen different configurations per concentration and eighty measurements in total.

FIGURE 5.13: Phantoms 3: The eventual phantom
This figure shows the eventual phantom and the five different concentrations of ICG used for the measurements.

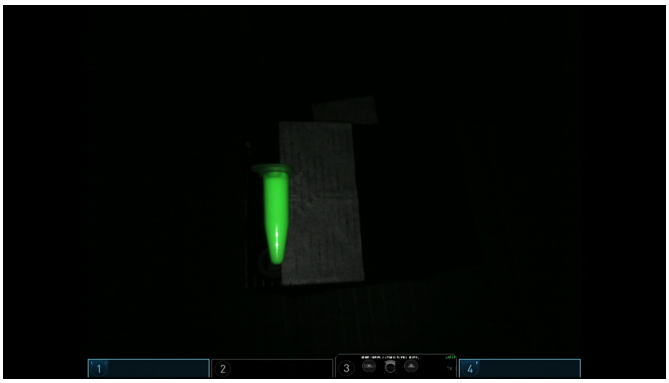

FIGURE 5.14: Image of phantoms 3 with Firefly Xi
This figure shows an example of the eventual phantom, phantoms 3, using the Firefly Xi. This image shows the highest concentration of ICG at d= 0 and a = 0°. A clear fluorescence signal is seen.

TABLE 5.2: The different variables used for measurements
This Table shows the values that were chosen for the different variables.

Solution number	Concentrations used (β in µM)
Solution 1	32.30
Solution 2	16.15
Solution 3	8.07
Solution 4	4.04
Solution 5	2.02

Distances from the camera (d in cm)
17.7
16.2
14.7
13.2

Orientations compared to base (α in °)
0
8
16
32

5.2.2 Dynamic measurements and the field of view

Figure 5.15 shows the results of the pixel intensity in measurement 1 which was done three times using solution 2. A change in intensity is seen throughout the FOV. At each frame, the intensity was measured with a frame rate of thirty frames per second.

Figure 5.16 shows the results of the pixel intensity in the FOV measurements in a contour plot. These measurements were also done using solution 2. The FOV was divided in sixteen rectangles from left to right and top to bottom. The measurements were performed at the approximate middle of the rectangle and the values in the corners of each rectangle were interpolated.

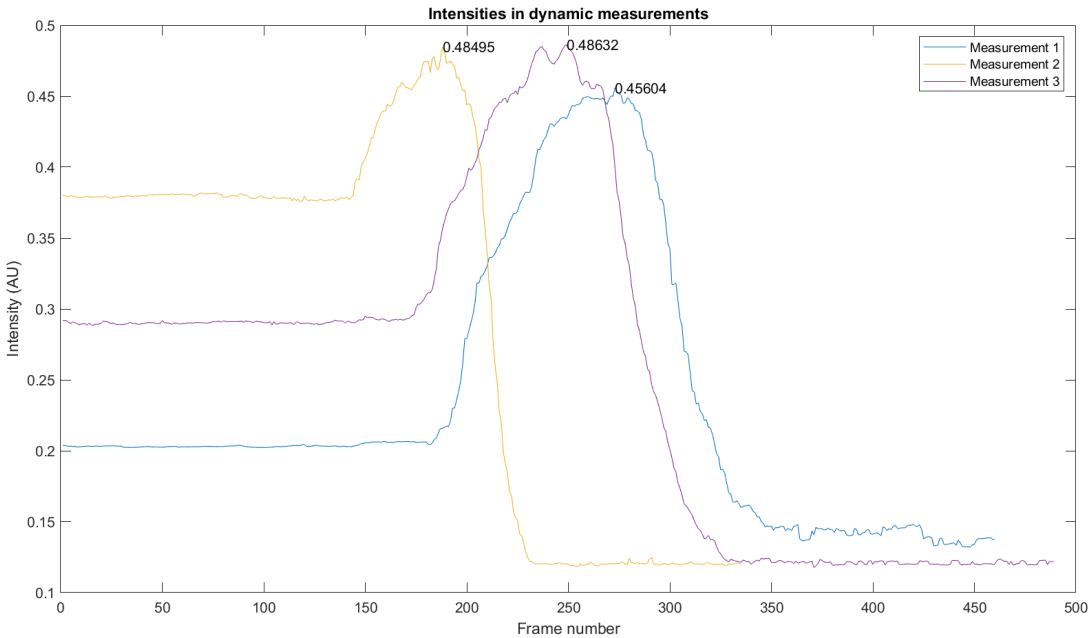

FIGURE 5.15: Results dynamic measurements
This figure shows the intensity in measurement 1 per frame when the phantom is moved from left to right in the FOV

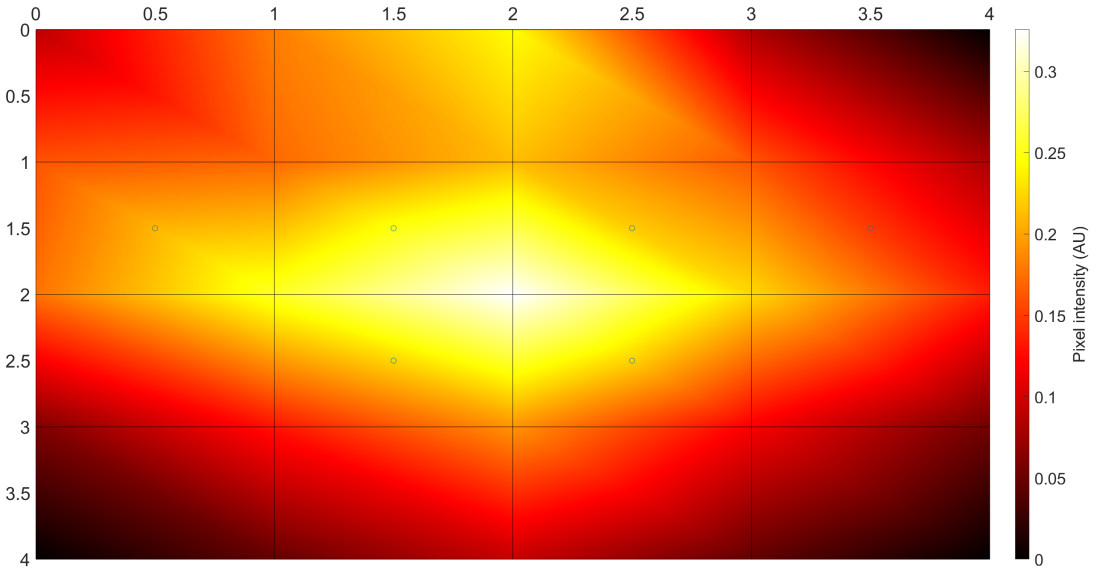

FIGURE 5.16: Contour plot of the pixel intensities in different parts of the FOV
The values in the middle of each square have been measured, the values surrounding this middle point are interpolated.

5.2.3 Static measurements

An overview of all the intensities and resulting figures is provided in Appendix III. One solution (solution 1) is taken as an example in this results section. Figure 5.17 and 5.18 show the pixel intensity on screen for solution 1 at different distances and orientations. A difference in intensity can clearly be seen in both figures. The figures for other concentrations show similar results and can be found in Appendix III. Based on the intensities found, the inverse-square law was applied at a 0° orientation. The intensity measured at the furthest distance (17.7cm) was used as the basis and each calculation was done using that intensity. Table 5.3 shows the results of those calculations including the difference in percentage. Concerning solution 1, the difference between estimated and measured pixel intensity is small, however, the differences found in the other solutions are larger even up to 32%, but mostly around 10%.

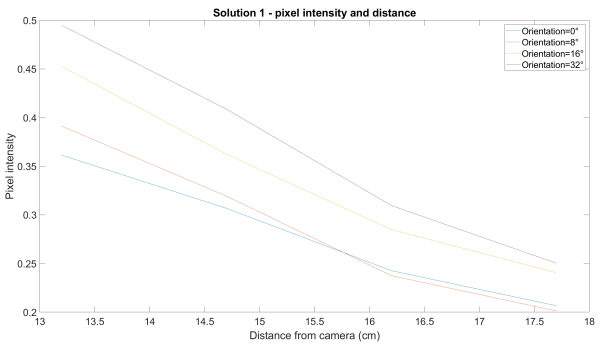

FIGURE 5.17: The pixel intensity using solution 1
For different orientations at different distances from the camera.

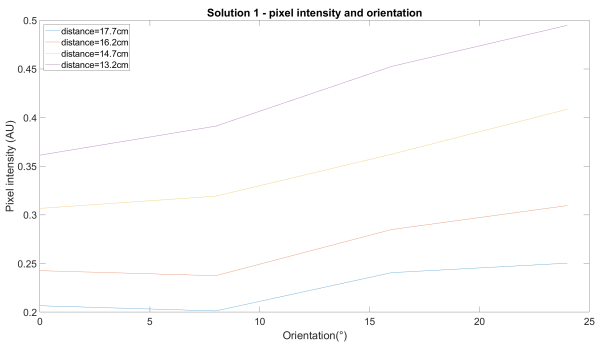

FIGURE 5.18: The pixel intensity using solution 1
For different distances from the camera at different orientations

TABLE 5.3: The inverse-square law applied for the intensities found for solution 1

	Measured pixel intensity (AU)	**Estimated pixel intensity (AU)**	**Difference (%)**
Distance = 17.7cm	0.2066	-	-
Distance = 16.2cm	0.2427	0.2466	-1.638
Distance = 14.7cm	0.3067	0.2995	2.330
Distance = 13.2cm	0.3614	0.3715	-2.783

Figure 5.19 shows the pixel intensity of the different solutions at different distances allowing comparison between the different concentrations. Interesting to see is that solution 3 shows the highest intensity closely followed by solution 2 and 4 where as solution 1 and 7 show similar intensities but lower than the other three. The figures for the other distances and orientations can be found in Appendix III and show similar results.

Figure 5.20 shows the result of a linear fitting at different distances based on the results found for solution 1 with an orientation of 0°. The mean squared error (mse) of this fitting is 0.00011748. The linear fittings for other concentrations and for different orientations can be found in Appendix III. The mse of other these configurations can be found in Table 5.4. In two out of five cases the mse found for the distance is lower than that of the orientation suggesting overall the orientation shows a better fitting. Nevertheless, when looking at the corresponding figures the 95% confidence intervals are similar or in the case of solution 5 even larger. Therewith, when looking at the mse's of solution 5, these are higher than the other solutions, suggesting a worse linear fitting.

Eventually, based on all of the results found, a correlation matrix was constructed and the Pearson correlation coefficient was calculated. The results are found Table 5.5. The correlation coefficient shows a significant p-value for the distance and the orientation not for the concentration.

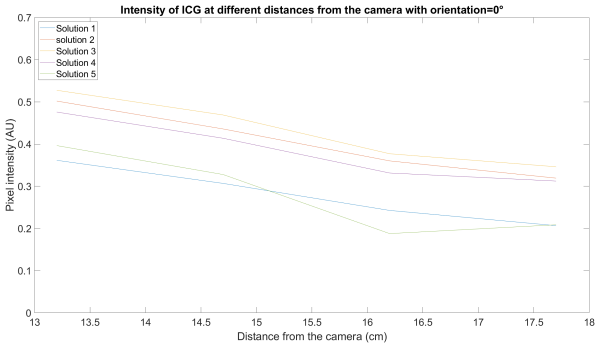

FIGURE 5.19: The pixel intensity for all solutions at α= 0°

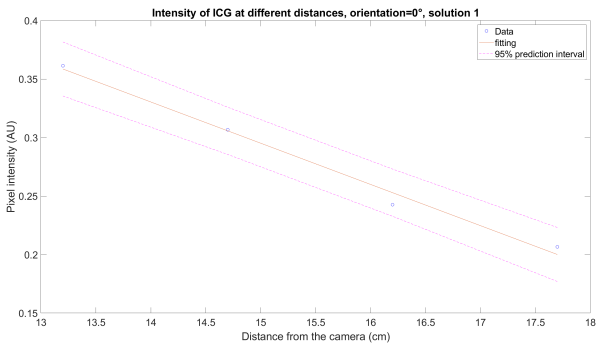

FIGURE 5.20: The linear fitting for solution 1 at a fixed distance and different orientations
This figure shows the linear fitting including the 95% confidence interval of the pixel intensity related to the distance at a stable orientation, the mse was 0.0001175.

TABLE 5.4: The mse values for different configurations

Solution	**Variables**	**mse**
Solution 1	Distance variable, orientation 0°	0.0001175
	Distance 17.7 cm, orientation variable	0.0002499
Solution 2	Distance variable, orientation 0°	0.0001932
	Distance 17.7 cm, orientation variable	0.0007266
Solution 3	Distance variable, orientation 0°	0.0004771
	Distance 17.7 cm, orientation variable	0.0003752
Solution 4	Distance variable, orientation 0°	0.0006081
	Distance 17.7 cm, orientation variable	0.0005514
Solution 5	Distance variable, orientation 0°	0.003522
	Distance 17.7 cm, orientation variable	0.001498

TABLE 5.5: Pearson correlation coefficient and corresponding P-value of each variable in correlation with the pixel intensity

Variable	**Correlation to pixel intensity**	**Corresponding *P*-value**
Distance	-0.7614	0.0000
Orientation	0.3066	0.0057
Concentration	-0.1999	0.0754

5.3 Discussion

The aim of this study was to research the influence of α, β, and d on the pixel intensity on screen and the possibilities of correction for these variables when using the Firefly of the Da Vinci Xi surgical robot. The hypothesis was that the software would apply an adaptive intensity. The data, especially Figures 5.15, 5.17, 5.18, and 5.19, show that the pixel intensity is influenced by α, β and, d, contradicting the hypothesis.

Table 5.3, where the inverse-square law is applied, shows small differences between the expected intensity and the actual intensity. However, when looking at Table A3 in Appendix III, five of the fifteen distances and solutions show differences of more than 10% and one even more than 30%. The inverse-square law has therefore not been confirmed in this research. The inverse-square law is based on a point source and due to its form the phantom can not be considered as a point source which might have influenced the results. Nevertheless, since some of the differences are small a second measurement must confirm this statement.

In Figure 5.15, measurement 1, all three measurements reach a similar maximum pixel intensity and end pixel intensity. Nonetheless, the start pixel intensity is different which is easily explained by the fact that the starting position of the phantom was not exactly the same at every measurement. Still, the main goal of this measurement was to register the difference in pixel intensity when moving a fluorescent object or the camera which happens often during surgery. Therefore, conclusions can still be based on these measurements and clearly show a change of intensity throughout the FOV which must be considered when using fluorescence imaging during surgery. The measurement 2 shows a difference in intensity throughout the FOV, the maximum pixel intensity is found mostly in the middle of the FOV, making it easier to account for when subjectively assessing the fluorescence. Interesting to see is that there is a slightly higher intensity in the top of the FOV which may be caused by the orientation of the 30° endoscope causing the excitation rays to have a small upward deviation despite most optimal positioning of the endoscope.

In phantom 1 and phantoms 2, natrium chloride was used to dissolve the ICG even though it is known that ICG binds to plasma proteins and lipids which induces fluorescence. Above all, the

absorption of ICG shifts when dissolved in blood compared to water or natrium chloride dilution from 780 nm in watery solutions to 805 nm when bound to plasma proteins in blood. [105] The absorption wavelength of ICG when bound to plasma proteins is the same as the excitation wavelength used with the Firefly Xi (Figure 5.1). [82] Which explains why the phantom 1 and phantoms 2 did not show fluorescence on screen. Furthermore, the material in phantom 1 showed reflection which would influence the average fluorescence intensity in a ROI. In phantoms 3, the ICG was dissolved in PBS and intralipid in five different concentrations which enabled ICG to bind to lipids and induce fluorescence at the applicable wavelengths. The Indian ink was added in phantoms 3 to induce absorbance similar to human blood, but the used concentration might have been too high, since no fluorescence was seen and these particular phantoms were not used.

Prior research considering fluorescence quantification or fluorescence phantoms has been done before. [62, 80, 91, 93, 108] Most researches ensure a stable distance, for example, Koyanagi *et al.* [93] ensure a constant distance of 20cm to the ROI using a surgeons hand. However, Nerup *et al.* [80] do not mention a constant distance which makes the results less trustworthy. Nevertheless, when looking at a relative intensity over time, which is customary in anastomosis research, a constant distance is only important within one patient and not between different patients. Van den Bos *et al.* [92] performed a similar study to the here described study in 2018 focusing on laparoscopic cholecystectomies. A fluorescence imaging system from Karl Storz was used with a 30° endoscope. They also found a correlation between the distance of the endoscope and the measured fluorescence intensity. Furthermore, they concluded the most efficient way to obtain fluorescence signals is to hold the endoscope perpendicular to the ROI. [92, 109] Recently, Meershoek *et al.* performed a similar study comparing the Firefly Si (a previous version of the Firefly) to the Firefly Xi and investigated the possibilities with multi colour imaging and the efficiency of the camera systems. The systems were perpendicularly stationed 1cm above the phantom. They also dissolved ICG in a human serum albumin medium to approximate the *in vivo* application. [84]

5.3.1 Limitations

Some limitations were encountered during this research. First of all, the fluorophore used, ICG, is an unstable fluorophore in a solution and when exposed to light due to photobleaching. Fortunately, all of the measurements were performed on the same day, minimizing the influence of photobleaching. Furthermore, ICG can be difficult to dissolve evenly influencing the actual concentration in the sample. [94] In a follow up experiment, the shortcomings of ICG might be overcome by using quantum dots which provide better photostability, however that approach might be less clinically relevant since it involves a different fluorophore which is currently not used clincally. [24] Furthermore, no control without any ICG was used. Since some concentrations did not show fluorescence on screen and confirmed the seen fluorescence in other concentrations is not the standard, it was assumed unnecessary to use a control.

Another limitation was the ambient light in the setup which is known to influence the fluorescence intensity. [110] This was minimised as much as possible but some LED-lights, for example, were impossible to turn off. To minimise the influence, the measurements were done inside a carton box. Additionally, the use of wooden blocks and wedges does not provide exact distances. Nevertheless, when translating this to a clinical setting, measurements in mm precision are not feasible. This also counts for the ambient light since the light will not be turned off during surgery and might also influence the fluorescence intensity slightly inside the abdomen. Therefore, despite using blocks and wedges and the presence of ambient light, the results found in this research remain clinically relevant.

Furthermore, when looking at the results found concerning the orientation, it is important to keep in mind that the phantom is lifted slightly when using the wedges (about 0.5cm) and is therefore closer to the camera. The results found for the orientation (the significant non-linear correlation and the change in intensity) may therefore partly be due to the decrease in distance

to the camera which is not accounted for in this research. Lastly, the images were downgraded in resolution when downloaded. The resolution of the images when downloaded was 1080p which is smaller than the resolution used in the Da Vinci surgical robot cockpit.

5.3.2 Clinical interpretation

As mentioned in Chapter 4, the current intraoperative assessment of fluorescence intensity is subjective. Based on this research, clinicians can be made aware of the operator-dependent fluorescence intensity influencing factors. The dynamic measurements emphasize this in particular. When intraoperatively interpreting the fluorescence intensity, several aspects need to be considered. This accounts for the here described novel SLN procedure but also for the frequently described anastomoses researches. Figure 5.17, 5.18, and 5.19 clearly show a decrease in pixel intensity when d is increased which also happens during surgery. This can also be concluded for α even though the influence seems smaller based on Figure 5.18. When analysing Figure 5.19 it is striking to see that solution 1 and solution 5 show similar values for the pixel intensity and no descending order is seen considering the concentrations. Furthermore, a non-significant non-linear correlation is found using the Pearson correlation coefficient (Table 5.5). This can be explained by a nonlinear fluorescence quantum yield compared to concentration and quenching, which is known to happen in higher concentrations starting at about 50 µM and decreases the fluorescence intensity. [94, 95, 110] When interpreting the eventual intensity the influence of concentration will need to be considered since these results show that a higher concentration does not automatically mean a higher intensity.

The different mse's found for the different configurations in Table 5.4 suggest a better linear fitting for the higher concentrations for both a variable orientation and distance. However, the difference within the 95% confidence intervals are often around 0.1 or more, for all configurations. Meaning a precise interpolation of the intensity might be difficult in a clinical setting. Nevertheless, the results of the Pearson correlation coefficient in Table 5.5 suggest there is a negative significant linear correlation between the distance and the fluorescence intensity meaning correction for distance may be possible. The positive correlation coefficient found for orientation is significant but does not imply a linear correlation.

If clinicians are willing to interpret the fluorescence intensity when using the Firefly Xi, the following aspects are important. Based on the FOV measurement the ROI should be in the middle of the FOV and the FOV and therewith the distance and orientation should not be changed during acquisition. When using a 30° endoscope it is important to consider the slight deviation of the excitation rays within the field. Lastly, the amount of fluorophore will not linearly change the intensity.

5.3.3 Future perspectives

The results in this research will contribute to the SLN study described in this thesis. When a sensitive and specific biomarker is found and can be coupled to a fluorophore to create a specific NIR tracer, the intensity might differ based on the amount of cancer cells present. Therefore, the intensity might provide information on the status and prognosis of the disease. If the new approach for SLN detection in CC is implemented in different medical centers there may not always be a Da Vinci surgical robot available. Therefore, it might be useful to set up a follow-up research with different NIR cameras. Above all, this would also answer the question whether the found results are typical for the Firefly Xi, for ICG or for the combination. Next to this, to create a more realistic setting, it is of use to dilute the ICG in human blood serum. This will provide intensities comparable to those found in the human body. Another option could be to mix ICG with human serum albumin to which ICG is bound in lymph, as described by Van den Bos *et al.* [92] and Meershoek *et al.* [84] or mix it with nanocolloid which should provide similar results. It can be assumed that an excess of albumin prevents quenching in higher

concentrations. The binding with albumin or nanocolloid will increase the fluorescence intensity and the hydrodynamic diameter. However, Hutteman *et al.* have showed no advantage in fluorescence imaging *in vivo* when using a combination between ICG and human serum albumin in comparison to ICG alone for the SLN procedure in breast cancer. [95] Still, these results may be doubted because of an unclear distance to the region of interest and an alternating exposure time. Based on the here described research, distance is an important variable influencing the fluorescence intensity and exposure time is also known to influence the fluorescence intensity. [94]

Another aspect, to reach more similarity to an *in vivo* situation, is to look into the influence of tissue depth. This can be done by using 'dirty' gelatin to cover the phantom, for example by adding cosmetic powder, or using beeswax plates which has similar optical properties to human tissue. [92, 96] A second option could be to use red meat or porcine offal as an extra layer between the camera and the phantom to mimic the mesenterium in the human abdomen or other tissue to see how the pixel intensity will change despite the short penetration depth of ICG. Lastly, there are numerous other variables which can be considered in future research such as the ones mentioned in Table 2.3. Many of them are related to the camera and the software, emphasizing that pixel intensity is an arbitrary unit and depends on many factors such as resolution or the manner of saving data which differs amongst camera's. [24]

5.4 Conclusion

In conclusion distance to the camera, orientation, and concentration influence the pixel intensity on screen when using the Firefly Xi. A significant linear correlation is found for the distance to the camera and the pixel intensity. A significant non-linear correlation is found concerning the orientation and the pixel intensity. These correlations may be used to create a model for correction and objective interpretation of pixel intensity in fluorescence measurements in the future.

CHAPTER 6

General conclusion

This study describes the possibilities of using a specific near-infrared tracer in a novel approach for sentinel lymph node detection in early-stage colon carcinoma during robotic surgery. Based on the findings, the sln procedure can be further enhanced and therewith the need for a hemicolectomy with the accompanying postoperative mortality and morbidity for the patient can be prevented. Chapter 3 describes a CD44v6 targeted biomarker as a sensitive biomarker to identify colon carcinoma cells with a specificity of 1. After confirmation of the findings with an enlarged dataset, the CD44v6 targeted biomarker can be used to develop a near-infrared tracer. Chapter 4 describes a reliable segmentation and quantification method for the intensity of indocyanine green in the new approach for sentinel lymph node identification with the potential of real-time quantification. Clinical use depends on future research into correction and standardisation of the procedure. Chapter 5 describes a pilot study for correction for distance, concentration, and orientation of the camera when using indocyanine green in robotic surgery with the Da Vinci Xi. A significant linear correlation between distance and the fluorescence intensity was found and should therefore be taken into consideration in the creation of a correction model.

Future outlook

The new approach for sln identification in colon carcinoma described in Chapter 4 can be enhanced using the results described in this thesis. The employment of CD44v6 as a sensitive and mainly specific biomarker in combination with a fluorophore like indocyanine green will enable colon carcinoma cell identification intraoperatively. Simultaneously quantifying the fluorescence intensity and assuming a correlation between this intensity and the number of colon carcinoma cells, can enable intraopertive prognosis and decision making.

References

[1] IKNL, "NKR Cijfers." [Online]. Available: https://www.iknl.nl/nkr-cijfers

[2] World Health Organization, "WHO mortality database," 2018. [Online]. Available: https://apps.who.int/healthinfo/statistics/mortality/whodpms/

[3] Landelijke werkgroep Gastrointestinale tumoren, "Colorectaalcarcinoom, Landelijke richtlijn, versie: 3.0," Integraal kankercentrum Nederland, Tech. Rep., 2014.

[4] RIVM, "Dikkedarmkanker — Cijfers & Context — Trends — Volksgezondheidenzorg.info." [Online]. Available: https://www.volksgezondheidenzorg.info/onderwerp/dikkedarmkanker/cijfers-context/trends#node-toekomstige-trend-dikkedarmkanker-door-demografische-ontwikkelingen

[5] M. H. Van der Pas, S. Meijer, O. S. Hoekstra, I. I. Riphagen, H. C. De Vet, D. L. Knol, N. C. Van Grieken, and W. J. Meijerink, "Sentinel lymph node procedure in colon and rectal cancer: A systematic review and meta- analysis," *The Lancet Oncology*, vol. 12, no. 6, pp. 540–550, 6 2011.

[6] B. Weixler, R. Warschkow, U. Güller, A. Zettl, U. Von Holzen, B. Schmied, and M. Zuber, "Isolated tumor cells in stage I & II colon cancer patients are associated with significantly worse disease-free and overall survival," *BMC Cancer*, vol. 16, 2016.

[7] M. Protic, A. Stojadinovic, A. Nissan, Z. Wainberg, S. Steele, D. Chen, I. Avital, and A. Bilchik, "Prognostic Effect of Ultra-Staging Node Negative Colon Cancer without Adjuvant Chemotherapy: A Prospective National Cancer Institute Clinical Trial," *Journal of the American College of Surgeons*, vol. 221, no. 3, pp. 643–785, 2015.

[8] S. Dighe, S. Purkayastha, I. Swift, P. P. Tekkis, A. Darzi, R. A'Hern, and G. Brown, "Diagnostic precision of CT in local staging of colon cancers: A meta-analysis," *Clinical Radiology*, vol. 65, no. 9, pp. 708–719, 9 2010.

[9] N. J. Harlaar, M. Koller, S. J. de Jongh, B. L. van Leeuwen, P. H. Hemmer, S. Kruijff, R. J. van Ginkel, L. B. Been, J. S. de Jong, G. Kats-Ugurlu, M. D. Linssen, A. Jorritsma-Smit, M. van Oosten, W. B. Nagengast, V. Ntziachristos, and G. M. van Dam, "Molecular fluorescence-guided surgery of peritoneal carcinomatosis of colorectal origin: a single-centre feasibility study," *The Lancet Gastroenterology and Hepatology*, 2016.

[10] R. A. Cahill, "Regional nodal staging for early stage colon cancer in the era of endoscopic resection and N.O.T.E.S." pp. 169–175, 6 2009.

[11] T. Buckle, A. C. Van Leeuwen, P. T. Chin, H. Janssen, S. H. Muller, J. Jonkers, and F. W. Van Leeuwen, "A self-assembled multimodal complex for combined pre- and intraoperative imaging of the sentinel lymph node," *Nanotechnology*, vol. 21, no. 35, 2010.

[12] J. I. Hida, M. Yasutomi, T. Maruyama, K. Fujimoto, T. Uchida, and K. Okuno, "The extent of lymph node dissection for colon carcinoma: The potential impact on laparscopic surgery," *Cancer*, vol. 80, no. 2, pp. 188–192, 7 1997.

[13] W. Wood, C. Staley, and J. Skandalakis, "Colon and Appendix," in *Anatomic basis of Tumor Surgery*, 2nd ed. St. Louis, Missouri: Springer Science & Business Media, 2010, ch. Chapter 8.

[14] W. Kelder, A. Braat, A. Karrenbeld, J. Grond, J. De Vries, J. Wolter, A. Oosterhuis, P. C. Baas, and J. Plukker, "The sentinel node procedure in colon carcinoma: a multi-centre study in The Netherlands," *International Journal of Colorectal Disease*, vol. 22, pp. 1509–1514, 2007.

[15] C. L. Willard-Mack, "Normal Structure, Function, and Histology of Lymph Nodes," *Toxicologic Pathology*, vol. 34, pp. 409–424, 2006.

[16] L. Weiss, "Normal lymph node," in *Lymph Nodes, Cambridge illustrated Surgical Pathology.* New York: Cambridge University Press, 2008, ch. 2, pp. 5 – 10.

[17] K. T. Huynh and A. J. Bilchik, "Sentinel lymph node biopsy and nodal ultrastaging in colorectal cancer," pp. 11–16, 2 2015.

[18] A. Bilchik, D. Nora, R. Tollenaar, C. Van de Velde, T. Wood, R. Turner, D. Hoon, and D. Morton, "Ultrastaging of early colon cancer using lymphatic mapping and molecular analysis," *European Journal of Cancer*, vol. 38, no. 7, pp. 977 – 985, 2002.

[19] E. Gould, T. Winship, P. Philbin, and H. Kerr, "Observations on a "sentinel node" in cancer of the parotid," *Cancer*, vol. 13, no. 1, pp. 77–78, 1 1960.

[20] R. Cabanas, "An approach for the treatment of penile carcinoma," *Cancer*, vol. 39, no. 2, pp. 456 – 466, 1977.

[21] D. Winchester, "The positive Sentinel Node," *Journal of Surgical Oncology*, vol. 103, no. 4, pp. 326–329, 2011.

[22] E. Hartmans, V. Orian-Rousseau, A. Matzke-Ogi, A. Karrenbeld, D. J. A. de Groot, S. de Jong, G. M. van Dam, R. S. Fehrmann, and W. B. Nagengast, "Functional genomic mRNA profiling of colorectal adenomas: Identification and in vivo validation of CD44 and splice variant CD44v6 as molecular imaging targets," *Theranostics*, vol. 7, no. 2, pp. 482–492, 2017.

[23] L. M. Crane, G. Themelis, K. Buddingh, T. Buddingh, N. J. Harlaar, R. G. Pleijhuis, A. Sarantopoulos, A. G. Van Der Zee, N. Vasilis, and G. M. Van Dam, "Multrispectral Real-time Fluorescence Imaging for Intraoperative Detection of the Sentinel Lymph Node in Gynecologic Oncology," *Journal of visualized experiments*, 2019.

[24] M. Koch, P. Symvoulidis, and V. Ntziachristos, "Tackling standardization in fluorescence molecular imaging," *Nature Photonics*, vol. 12, no. September, 2018.

[25] S. Goineau, P. Guillaume, and G. Froget, "Safety Pharmacology II-CV, GI, Respiratory and Renal Safety," in *Reference Module in Biomedical Sciences.* Elsevier, 2014.

[26] K. Alitalo and P. Carmeliet, "Molecular mechanisms of lymphangiogenesis in health and disease," *Cancer cell*, vol. 1, no. 3, pp. 219–227, 4 2002.

[27] M. Hoffman, "Picture of the Human Colon Anatomy & Common Colon Conditions." [Online]. Available: https://www.webmd.com/digestive-disorders/picture-of-the-colon#1

[28] W. F. Boron and E. L. Boulpaep, *Medical Physiology*, 2nd ed., E. O'Grady, A. Hall, P. Tannian, J. Casey, and S. Stave, Eds. Philadelphia: Elsevier Saunders, 2012.

[29] J. Y. Kim, "The lymphatic spread of colon cancer," in *Surgical Treatment of Colorectal Cancer*. Springer Singapore, 5 2018, pp. 241–249.

[30] S. Podgrabinska and M. Skobe, "Role of lymphatic vasculature in regional and distant metastases," *Microvascular Research*, vol. 95, no. 1, pp. 46–52, 2014.

[31] A. Adrouny, "Who gets Colon Cancer and Why," in *Understanding Colon Cancer*. Mississippi: University press of Mississippi, 2002, ch. chapter 1, pp. 1 –18.

[32] L. Durko and E. Malecka-Panas, "Lifestyle Modifications and Colorectal Cancer," *current colorectal cancer reports*, vol. 10, pp. 45 – 54, 2014.

[33] W. Willett, "The search for the causes of breast and colon cancer," pp. 389–394, 1989.

[34] S. G. Thrumurthy, S. S. Thrumurthy, C. E. Gilbert, P. Ross, and A. Haji, "Colorectal adenocarcinoma: Risks, prevention and diagnosis," *BMJ (Online)*, vol. 354, 2016.

[35] "Colon cancer staging - Wikiwand." [Online]. Available: https://www.wikiwand.com/en/Colon_cancer_staging

[36] M. H. G. M. Van Der Pas, M. Ankersmit, H. B. A. C. Stockmann, R. Silvis, N. C. T. Van Grieken, H. Bril, and W. J. H. J. Meijerink, "Laparoscopic Sentinel Lymph Node Identification in Patients with Colon Carcinoma Using a Near-Infrared Dye: Description of a New Technique and Feasibility Study," *Journal of laparoendoscopic & advanced surgical techniques*, vol. 23, no. 4, pp. 367 – 371, 2013. [Online]. Available: www.liebertpub.com

[37] M. Ankersmit, M. Van der Pas, D. Van Dam, and W. Meijerink, "Near infrared fluorescence lymphatic laparoscopy of the colon and mesocolon," *colorectal disease*, vol. 13, pp. 70–73, 2011.

[38] B. Duong and Medtruth, "Adaptive Radiotherapy: Cancer Treatment May Be Safer, More Accessible." [Online]. Available: https://medtruth.com/articles/research-and-findings/adaptive-radiotherapy-cancer-treatment-may-be-safer-less-aggressive/

[39] freepik.com, "Artsen chirurgische operatie in clean room illustratie." [Online]. Available: https://nl.freepik.com/premium-vector/artsen-chirurgische-operatie-in-clean-room-illustratie_2638004.htm

[40] ——, "Man met pijn." [Online]. Available: https://nl.freepik.com/premium-vector/man-met-pijn-ziekte-bij-mannen-pijnlijke-plekken-migraine-hoofdpijn-en-buikpijn-pijnlijke-pijn-zones-cartoon-vector-illustratie-set_9827994.htm

[41] Stichting stop Darmkanker Nederland, "Colonoscopie." [Online]. Available: https://www.stopdarmkanker.nl/darmkanker/colonoscopie

[42] Maag Darm Lever Centrum Leiden, "Bevolkingsonderzoek darmkanker." [Online]. Available: https://mdlcentrumleiden.nl/poliklinieken/bevolkingsonderzoek-darmkanker.html

[43] Imelda ziekenhuis, "CT-Onderzoek van de volledige buik (Abdomen)." [Online]. Available: https://www.imelda.be/zorgaanbod/medische-specialismen/medische-beeldvorming/ct-scan/ct-onderzoek-van-de-volledige-buik

[44] N. Dogan, S. Dogan, G. Favero, C. Köhler, and P. Dursun, "The Basics of Sentinel Lymph Node Biopsy: Anatomical and Pathophysiological Considerations and Clinical Aspects," *Journal of Oncology*, 2019.

[45] M. Kusano, Y. Tajima, K. Yamazaki, M. Kato, M. Watanabe, and M. Miwa, "Sentinel node mapping guided by indocyanine green fluorescence imaging: A new method for sentinel node navigation surgery in gastrointestinal cancer," *Digestive Surgery*, vol. 25, no. 2, pp. 103–108, 2008.

[46] P. W. Hamilton, P. Bankhead, Y. Wang, R. Hutchinson, D. Kieran, D. G. McArt, J. James, and M. Salto-Tellez, "Digital pathology and image analysis in tissue biomarker research," *Methods*, vol. 70, no. 1, pp. 59–73, 2014.

[47] T. Wood, S. Saha, D. Morton, G. Tsioulias, D. Rangel, W. Hutchinson, L. Foshag, and A. Bilchik, "Validation of Lymphatic Mapping in Colorectal Cancer: In Vivo, Ex Vivo, and Laparoscopic Techniques," *Annals of Surgical Oncology*, vol. 8, no. 2, pp. 150–157, 3 2001.

[48] M. Ong and J. Schofield, "Assessment of lymph node involvement in colorectal cancer," *World J Gastrointest Surg*, vol. 8, no. 3, pp. 179–192, 2016.

[49] A. E. Merrie, L. V. Phillips, K. Yun, and J. L. McCall, "Skip metastases in colon cancer: Assessment by lymph node mapping using molecular detection," *Surgery*, vol. 129, no. 6, pp. 684–691, 6 2001.

[50] H. S. Andersen, A. Louise, B. Bennedsen, S. K. Burgdorf, J. Ravn Eriksen, S. Eiholm, A. Toxvaerd, . Lene, B. Riis, J. Rosenberg, and I. Gögenur, "In vivo and ex vivo sentinel node mapping does not identify the same lymph nodes in colon cancer," *International Journal of Colorectal Disease*, vol. 32, pp. 983 – 990, 2017.

[51] T. Vo-Dinh, "Optical properties of tissue," in *Biomedical photonics*. Oak Ridge, Tennessee: CRC PRESS LLC, 2003.

[52] M. A. Ansari and E. Mohajerani, "Mechanisms of Laser-Tissue Interaction : I . Optical Properties of Tissue," *Journal of lasers in medical sciences*, vol. 2, no. 3, pp. 119–125, 2011.

[53] J. T. Bushberg, J. A. Seibert, E. M. Leidholdt, and J. M. Boone, "Radiation and the atom," in *The Essential Physics of Medical Imaging*, 2nd ed. Philadelphia: Lippincott Williams & Wilkins, 2012, ch. 2.

[54] S. Keereweer, P. B. A. A. V. Driel, T. J. A. Snoeks, J. D. F. Kerrebijn, R. J. Baatenburg De Jong, A. L. Vahrmeijer, H. J. C. M. Sterenborg, and C. W. G. M. L€ Owik, "Optical Image-Guided Cancer Surgery: Challenges and Limitations," *Clin Cancer Res*, vol. 19, no. 14, 2013.

[55] G. Themelis, J. S. Yoo, K.-S. Soh, R. Schulz, and V. Ntziachristos, "Real-time intraoperative fluorescence imaging system using light-absorption correction," *Journal of Biomedical Optics*, vol. 14, no. 6, p. 064012, 2009.

[56] P. A. Valdés, F. Leblond, V. L. Jacobs, B. C. Wilson, K. D. Paulsen, and D. W. Roberts, "Quantitative, spectrally-resolved intraoperative fluorescence imaging," *scientific reports*, vol. 798, no. 2, 11 2012. [Online]. Available: www.nature.com/scientificreports

[57] T. Vo-Dinh, "Light-Tissue Interactions," in *Biomedical Photonics*. Oak Ridge, Tennessee: CRC PRESS LLC, 2003, ch. 3.

[58] ——, "Fluorescence spectroscopy for biomedical diagnostics," in *Biomedical Photonics*. Oak Ridge, Tennessee: CRC PRESS LLC, 2003, ch. 28.

[59] F. Woolfe, M. Gerdes, M. Bello, X. Tao, and A. Can, "Autofluorescence removal by non-negative matrix factorization," *IEEE Transactions on Image Processing*, vol. 20, no. 4, pp. 1085–1093, 2011.

[60] P. Choyke, "Science to practice: Is it possible to quantify fluorescence during optical endoscopy?" *Radiology*, vol. 245, no. 2, pp. 307–308, 2007.

[61] E. Towle, L. Richards, S. Shams Kazmi, D. Fox, and A. Dunn, "Comparison of Indocyanine Green Angiography and Laser Speckle Contrast Imaging for the Assessment of Vasculature Perfusion," *Neurosurgery*, vol. 71, no. 5, 2012.

[62] R. P. Judy, J. J. Keating, E. M. Dejesus, J. X. Jiang, O. T. Okusanya, S. Nie, D. E. Holt, S. P. Arlauckas, P. S. Low, E. J. Delikatny, and S. Singhal, "Quantification of tumor fluorescence during intraoperative optical cancer imaging," *Nature Publishing Group*, 2015.

[63] B. protyniak, A. Dinallo, W. Boyan jr., R. Dressner, and M. Arvanitis, "Intraoperative Indocyanine Green Fluorescence Angiography - An objective Evaluation of Anastomotic Perfusion in Colorectal Surgery," *The American Surgeon*, vol. 81, no. 6, pp. 580–584, 6 2015.

[64] S. Blankenberg and T. Zeller, "Standard and Novel Biomarkers," in *Chronic Coronary Artery Disease: A Companion to Braunwald's Heart Disease*. Elsevier, 2018, ch. 9, pp. 98–113.

[65] E. De Boer, N. J. Harlaar, A. Taruttis, W. B. Nagengast, E. L. Rosenthal, V. Ntziachristos, and G. M. Van Dam, "Optical innovations in surgery," *British Journal of Surgery*, vol. 102, no. 2, 2015.

[66] A. Garouniatis, A. Zizi-Sermpetzoglou, S. Rizos, A. Kostakis, N. Nikiteas, and A. G. Papavassiliou, "FAK, CD44v6, c-Met and EGFR in colorectal cancer parameters: Tumour progression, metastasis, patient survival and receptor crosstalk," *International Journal of Colorectal Disease*, vol. 28, no. 1, pp. 9–18, 1 2013.

[67] L. Ma, L. Dong, and P. Chang, "CD44v6 engages in colorectal cancer progression," *Cell death and Disease*, vol. 10, no. 30, 2019.

[68] A. Afify, B. Durbin-Johnson, A. Virdi, and H. Jess, "The expression of CD44v6 in colon: From normal to malignant," *Annals of Diagnostic Pathology*, vol. 20, pp. 19–23, 2 2016.

[69] I. D. Nagtegaal and P. Quirke, "Colorectal tumour deposits in the mesorectum and pericolon; a critical review," *Histopathology*, vol. 51, pp. 141–149, 2007.

[70] D. Coppola, M. Hyacinthe, L. Fu, A. B. Cantor, R. Karl, J. Marcet, D. L. Cooper, S. V. Nicosia, and H. S. Cooper, "CD44V6 Expression in Human Colorectal Carcinoma," *Human pathology*, vol. 29, no. 6, pp. 627 – 635, 1998.

[71] Y.-J. Guo, G. Liu, X. Wang, D. Jin, M. Wu, J. Ma, and M.-S. Sy, "Potential Use of Soluble CD44 in Serum as Indicator of Tumor Burden and Metastasis in Patients with Gastric or Colon Cancer," *Cancer research*, vol. 54, no. 1, pp. 422 – 426, 1994.

[72] M. C. Boonstra, B. Tolner, B. E. Schaafsma, L. S. Boogerd, H. AJM Prevoo, G. Bhavsar, P. J. Kuppen, C. F. Sier, B. A. Bonsing, J. V. Frangioni, C. J. van de Velde, K. A. Chester, and A. L. Vahrmeijer, "Pre-clinical evaluation of a novel CEA-targeting near-infrared fluorescent tracer delineating colorectal and pancreatic tumors HHS Public Access," *Int J Cancer*, vol. 137, no. 8, pp. 1910–1920, 2015.

[73] T. Ishida, "Immunohistochemical Expression of the CD44 Variant 6 in Colorectal Adenocarcinoma," *Surgery Today*, vol. 30, pp. 28 – 32, 2000.

[74] H. Liu, L. Lv, and H. Shen, "Intratumoral heterogeneity of CD44v6 in rectal cancer," *Clinical and Translational Oncology*, vol. 19, no. 4, pp. 425–431, 2016.

[75] X. D. Li, M. Ji, J. Wu, J. T. Jiang, and C. P. Wu, "Clinical significance of CD44 variants expression in colorectal cancer," *Tumori*, vol. 99, no. 1, pp. 88–92, 2013.

[76] P. Minoo, I. Zlobec, M. Peterson, L. Terracciano, and A. Lugli, "Characterization of rectal, proximal and distal colon cancers based on clinicopathological, molecular and protein profiles." *International Journal of Oncology*, vol. 37, pp. 707 – 718, 2010.

[77] M. Koller, S. Q. Qiu, M. D. Linssen, L. Jansen, W. Kelder, J. de Vries, I. Kruithof, G. J. Zhang, D. J. Robinson, W. B. Nagengast, A. Jorritsma-Smit, B. van der Vegt, and G. M. van Dam, "Implementation and benchmarking of a novel analytical framework to clinically evaluate tumor-specific fluorescent tracers," *Nature Communications*, vol. 9, no. 1, pp. 1–11, 2018.

[78] M. Chand, D. S. Keller, H. M. Joshi, L. Devoto, M. Rodriguez-Justo, and R. Cohen, "Feasibility of fluorescence lymph node imaging in colon cancer : FLICC," *Techniques in Coloproctology*, 2018.

[79] T. Burghgraef, A. Zweep, D. Sikkenk, M. van der Pas, P. Verheijen, and E. Consten, "In vivo sentinel lymph node identification using fluorescent tracer imaging in colon cancer: a systematic review and meta-analysis," *Critical Reviews in Oncology/Hematology*, vol. 158, no. April 2020, p. 103149, 2020. [Online]. Available: https://doi.org/10.1016/j.critrevonc.2020.103149

[80] N. Nerup, H. S. Andersen, R. Ambrus, R. B. Strandby, M. B. S. Svendsen, M. H. Madsen, L. B. Svendsen, and M. P. Achiam, "Quantification of fluorescence angiography in a porcine model," *Langenbeck's Archives of Surgery*, vol. 402, no. 4, pp. 655–662, 6 2017.

[81] I. Berg van den, "The quantification of fluorescence images during the creation of anastomoses and sentinel lymph node identification using indocyanine green," University of Twente, Tech. Rep., 2020.

[82] F. Laenen, "Expert Intuitive."

[83] T. B. Manny, L. S. Krane, and A. K. Hemal, "Indocyanine Green cannot predict malignancy in partial nephrectomy: Histopathalogic correlation with fluorescence pattern in 100 patients." *journal of endourology*, vol. 27, no. 7, pp. 918–921, 7 2013.

[84] P. Meershoek, G. H. KleinJan, D. M. van Willigen, K. P. Bauwens, S. J. Spa, F. van Beurden, E. J. van Gennep, A. M. Mottrie, H. G. van der Poel, T. Buckle, F. W. van Leeuwen, and M. N. van Oosterom, "Multi-wavelength fluorescence imaging with a da Vinci Firefly—a technical look behind the scenes," *Journal of Robotic Surgery*, 2020.

[85] F. Patin, "An Introduction To Digital Image Processing," 2003. [Online]. Available: http://yov408.free.fr

[86] I. the Mathworks, "Understanding Color Spaces and Color Space Conversion - MATLAB & Simulink - MathWorks Benelux." [Online]. Available: https://nl.mathworks.com/help/images/understanding-color-spaces-and-color-space-conversion.html

[87] Y. M. Gao, J. C. Wei, P. U. Mak, M. I. Vai, M. Du, and S. H. Pun, "Development of a calibration strip forimmunochromatographic assay detection systems," *Sensors (Switzerland)*, vol. 16, no. 7, pp. 8–14, 2016.

[88] S. Sural, G. Qian, and S. Pramanik, "Segmentation and histogram generation using the HSV color space for image retrieval," *IEEE International Conference on Image Processing*, vol. 2, pp. 589–592, 2002.

[89] World Health Organization, "Nutrition - Body mass index - BMI." [Online]. Available: https://www.euro.who.int/en/health-topics/disease-prevention/nutrition/a-healthy-lifestyle/body-mass-index-bmi

[90] American Society of Anesthesiologists, "ASA Physical Status Classification System — American Society of Anesthesiologists (ASA)." [Online]. Available: https://www.asahq.org/standards-and-guidelines/asa-physical-status-classification-system

[91] B. Seeliger, V. Agnus, P. Mascagni, M. Barberio, F. Longo, A. Lapergola, D. Mutter, A. S. Klymchenko, M. Chand, J. Marescaux, and M. Diana, "Simultaneous computer-assisted assessment of mucosal and serosal perfusion in a model of segmental colonic ischemia," *Surgical Endoscopy*, 2019.

[92] J. van den Bos, F. P. Wieringa, N. D. Bouvy, and L. P. Stassen, "Optimizing the image of fluorescence cholangiography using ICG: a systematic review and ex vivo experiments," *Surgical Endoscopy*, vol. 32, no. 12, pp. 4820–4832, 2018.

[93] K. Koyanagi, S. Ozawa, J. Oguma, A. Kazuno, Y. Yamazaki, Y. Ninomiya, H. Ochiai, and Y. Tachimori, "Blood flow speed of the gastric conduit assessed by indocyanine green fluorescence: New predictive evaluation of anastomotic leakage after esophagectomy," *Medicine (United States)*, vol. 95, no. 30, 7 2016.

[94] J. T. Alander, I. Kaartinen, A. Laakso, T. Pätilä, T. Spillmann, V. V. Tuchin, M. Venermo, and P. Välisuo, "A Review of Indocyanine Green Fluorescent Imaging in Surgery," *International Journal of Biomedical Imaging*, vol. 2012, 2012.

[95] M. Hutteman, J. Sven, D. Mieog, J. R. Van Der Vorst, G.-J. Liefers, H. Putter, C. W. G. M. Löwik, J. V. Frangioni, J. H. Van De Velde, and A. L. Vahrmeijer, "Randomized, double-blind comparison of indocyanine green with or without albumin premixing for near-infrared fluorescence imaging of sentinel lymph nodes in breast cancer patients," *Breast Cancer Res Treat*, vol. 127, no. 1, pp. 163–170, 2011.

[96] A. M. Almarhaby, J. E. Lees, S. L. Bugby, M. S. Alqahtani, L. K. Jambi, W. R. Mcknight, and A. C. Perkins, "Characterisation of a near-infrared (NIR) fluorescence imaging systems intended for hybrid gamma-NIR fluorescence image guided surgery," *Journal of Instrumentation*, vol. 14, 2019.

[97] A. Kim, M. Khurana, Y. Moriyama, and B. C. Wilson, "Quantification of in vivo fluorescence decoupled from the effects of tissue optical properties using fiber-optic spectroscopy measurements," *Journal of Biomedical Optics*, vol. 15, no. 6, p. 067006, 2010.

[98] F. van Leeuwen-van Zaane, U. A. Gamm, P. B. A A van Driel, T. J. A Snoeks, H. S. de Bruijn, A. van der Ploeg-van den Heuvel, I. M. Mol, C. W. G M Löwik, H. J. C M Sterenborg, A. Amelink, D. J. Robinson, M. Schouten, H. J. Sterenborg, S. C. Kanick, and

M. Carlo, "In vivo quantification of the scattering properties of tissue using multi-diameter single fiber reflectance spectroscopy," *Biomed. Opt. Express*, vol. 2, no. 6, pp. 1838–1840, 2011.

[99] S. J. De Jongh, F. J. Voskuil, I. Schmidt, A. Karrenbeld, G. Kats-Ugurlu, G. J. Meersma, J. Westerhof, M. J. H. Witjes, G. M. Van Dam, D. J. Robinson, and W. B. Nagengast, "C-Met targeted fluorescence molecular endoscopy in Barrett's esophagus patients and identification of outcome parameters for phase-I studies," *Theranostics*, vol. 10, no. 12, pp. 5357–5367, 2020.

[100] B. Seeliger, M. K. Walz, P. F. Alesina, V. Agnus, R. Pop, M. Barberio, A. Saadi, M. Worreth, J. Marescaux, and M. Diana, "Fluorescence-enabled assessment of adrenal gland localization and perfusion in posterior retroperitoneoscopic adrenal surgery in a preclinical model," *Surgical Endoscopy*, vol. 34, no. 3, pp. 1401–1411, 3 2020.

[101] M. Lualdi, A. Colombo, B. Farina, S. Tomatis, and R. Marchesini, "A phantom with tissue-like optical properties in the visible and near infrared for use in photomedicine," *Lasers in Surgery and Medicine*, vol. 28, no. 3, pp. 237–243, 2001.

[102] B. W. Pogue and M. S. Patterson, "Review of tissue simulating phantoms for optical spectroscopy, imaging and dosimetry," *Journal of Biomedical Optics*, vol. 11, no. 4, p. 041102, 2006.

[103] R. Pleijhuis, A. Timmermans, J. De Jong, E. De Boer, V. Ntziachristos, and G. Van Dam, "Tissue-simulating phantoms for assessing potential near-infrared fluorescence imaging applications in breast cancer surgery," *Journal of Visualized Experiments*, no. 91, 2014.

[104] M. Anastasopoulou, M. Koch, D. Gorpas, A. Karlas, U. Klemm, P. B. Garcia-Allende, and V. Ntziachristos, "Comprehensive phantom for interventional fluorescence molecular imaging," *Journal of Biomedical Optics*, vol. 21, no. 9, p. 091309, 2016.

[105] S. Yoneya, T. Saito, Y. Komatsu, I. Koyama, K. Takahashi, and J. Duvoll-young, "Binding Properties of Indocyanine Green in Human Blood," *Investigative ophthalmology and visual science*, vol. 39, no. 7, pp. 1286–1290, 1998.

[106] Rapid Tables, "RGB to HSV conversion — color conversion." [Online]. Available: https://www.rapidtables.com/convert/color/rgb-to-hsv.html

[107] N. Otsu, "A Threshold Selection Method from Gray-Level Histograms," *IEEE Transactions on systems, man, and cybernetics*, vol. 9, no. 1, pp. 62–66, 1 1979. [Online]. Available: http://webserver2.tecgraf.puc-rio.br/~mgattass/cg/trbImg/Otsu.pdf

[108] A. J. Ruiz, E. P. M. Larochelle, V. Ntziachristos, T. J. Pfefer, B. W. Pogue, A. J. Ruiz, M. Wu, E. P. M. Larochelle, D. Gorpas, V. Ntziachristos, J. Pfefer, and B. W. Pogue, "Indocyanine green matching phantom for fluorescence-guided surgery imaging system characterization and performance assessment," *Journal of Biomedical Optics*, vol. 25, no. 5, 2020.

[109] Y. Kono, T. Ishizawa, K. Tani, N. Harada, J. Kaneko, A. Saiura, Y. Bandai, and N. Kokudo, "Techniques of Fluorescence Cholangiography During Laparoscopic Cholecystectomy for Better Delineation of the Bile Duct Anatomy," *Medicine*, vol. 94, no. 25, 2015.

[110] M. Hellan, G. Spinoglio, A. Pigazzi, and J. Lagares-Garcia, "The influence of fluorescence imaging on the location of bowel transection during robotic left-sided colorectal surgery," *Surgical Endoscopy*, vol. 28, p. 1695–1702, 2014.

Appendix I: Staining protocol for a CD44v6 targeted biomarker.

IHC protocol for a CD44v6 targeted biomarker (ab254174)

Dewaxing and rehydration:

- Dewax in xylene (2 times, 10 minutes).
- Rinse in 100% alcohol.
- Rinse in 96% alcohol.
- Rinse in 70% alcohol.
- Rinse in distilled water.

Antigen retrieval:

- Buffer: Tris/EDTA pH 9.0.
- Preheat buffer in microwave.
- Tissue in buffer: 15 minutes at 500 watt.
- Cool down for 15 minutes.
- Rinse using PBS 3 times for 5 minutes.

Staining:

- Blocking endogenous peroxidase by using 0.5mL of 30% H_2O_2 in 50mL PBS for 30 minutes.
- Rinse using PBS 3 times for 5 minutes.
- Dry around tissue.
- Incubate with first antibody, ab254174, 1:200 in PBS and 1% bovine serum albumin (BSA) for 1 hour.
- Rinse using PBS 3 times for 5 minutes.
- Incubate with second antibody, RAM-HRP 1:100 in PBS and 1% BSA for 30 minutes.
- Rinse using PBS 3 times for 5 minutes.
- Incubate with third antibody, GAR-HRP 1:100 in PBS and 1% BSA for 30 minutes.
- Rinse using PBS 3 times for 5 minutes.
- Dilute 50mL 3,3'-Diaminobenzidine (DAB) in 50mL PBS and rinse for 10 minutes, then add 50µL H_2O_2.

- Rinse in distilled water 10 times for 5 minutes.

Counter staining:

- Stain with haematoxyline for 2 minutes.
- Rinse using tap water.

Dehydrate and embedding:

- Rinse in 70% alcohol.
- Rinse in 96% alcohol.
- Rinse in 100% alcohol.
- Air dry for a minium of 30 minutes.
- embed the tissue.

Appendix II: H-scores of the CD44v6 staining

TABLE A1: The H-scores, complete results

The resulting H-scores concerning the CD44v6 staining of the different slices. T is tumour, N+ is positive lymph node, N- is negative lymph and TD is tumour deposit.

Patient	**Tissue**	**Percentage 0**	**Percentage 1+**	**Percentage 2+**	**Percentage 3+**	**H-score**	**Tumour stage**	**Neoadjuvant treatment**
1	T	50%	45%	5%	0%	55	T_2	No
1	N-	100%	0%	0%	0%	0	T_2	No
1	N+	45%	55%	0%	0%	55	T_2	No
1	Polyp	40%	10%	50%	0%	110	T_2	No
2	T	0%	50%	50%	0%	150	T_4	No
2	N+	0%	45%	55%	0%	155	T_4	No
2	N-	100%	0%	0%	0%	0	T_4	No
2	N+	0%	100%	0%	0%	100	T_4	No
2	N+	0%	0%	85%	15%	215	T_4	No
3	N-	100%	0%	0%	0%	0	T_4	No
3	N+	0%	10%	50%	40%	230	T_4	No
3	T	50%	50%	0%	0%	50	T_4	No
3	TD	50%	50%	0%	0%	50	T_4	No
4	T	40%	10%	0%	50%	160	T_2	Yes
4	N+	40%	10%	50%	0%	110	T_2	Yes
4	N-	100%	0%	0%	0%	0	T_2	Yes
5	T	35%	65%	0%	0%	65	T_3	Yes
5	N-	100%	0%	0%	0%	0	T_3	Yes
5	T	0%	50%	50%	0%	150	T_3	Yes
5	N+	0%	70%	30%	0%	130	T_3	Yes
6	T	0%	0%	40%	60%	260	T_3	No
6	N-	100%	0%	0%	0%	0	T_3	No
6	T	10%	35%	35%	20%	165	T_3	No
6	N+	10%	90%	0%	0%	90	T_3	No
7	T	90%	0%	0%	10%	30	T_3	No
7	N-	100%	0%	0%	0%	0	T_3	No
7	N+	80%	0%	10%	10%	50	T_3	No
8	T	0%	50%	40%	10%	160	T_4	No
8	N-	100%	0%	0%	0%	0	T_4	No
8	T	0%	60%	20%	0%	100	T_4	No
8	N+	20%	40%	40%	0%	120	T_4	No
9	T	0%	0%	30%	70%	270	T_4	No
9	N+	0%	0%	0%	100%	300	T_4	No
10	N-	100%	0%	0%	0%	0	T_4	No
10	N+	80%	10%	10%	0%	30	T_4	No
10	T	30%	70%	0%	0%	70	T_4	No
10	TD	0%	100%	0%	0%	100	T_4	No
11	T	10%	20%	70%	0%	160	T_4	Yes
11	N+	0%	100%	0%	0%	100	T_4	Yes
12	T	90%	10%	0%	0%	10	T_4	Yes

Continued on next page

Patient	**Tissue**	**Percentage 0**	**Percentage 1+**	**Percentage 2+**	**Percentage 3+**	**H-score**	**Tumour stage**	**Neoadjuvant treatment**
13	T	10%	70%	20%	0%	110	T_4	No
13	N+	20%	80%	0%	0%	80	T_4	No
14	T	80%	20%	0%	0%	20	T_3	No
14	N+	90%	10%	0%	0%	10	T_3	No
15	T	80%	20%	0%	0%	20	T_3	Yes
15	TD	100%	0%	0%	0%	0	T_3	Yes
16	TD	80%	20%	0%	0%	20	T_4	Yes
16	T	0%	40%	60%	0%	160	T_4	Yes
17	T	0%	0%	0%	100%	300	T_3	Yes
17	N+	0%	50%	50%	0%	150	T_3	Yes
18	T	0%	100%	0%	0%	100	T_3	Yes
18	TD	0%	100%	0%	0%	100	T_3	Yes
19	T	0%	0%	80%	20%	220	T_4	No
19	N+	0%	0%	80%	20%	220	T_4	No
20	T	0%	80%	20%	0%	180	T_4	No
20	N+	0%	100%	0%	0%	100	T_4	No
21	T	0%	0%	20%	80%	280	T_4	No
21	N+	0%	0%	0%	100%	300	T_4	No

Appendix III: Extensive results of the static measurements

TABLE A2: The resulting intensities in the phantoms with the different orientation (α), camera distance (d) and concentration of ICG (β)

		d = 17.7cm	d = 16.2cm	d = 14.7cm	d = 13.2cm
Solution 1	$\alpha = 0°$	0.2066	0.2427	0.3067	0.3614
	$\alpha = 8°$	0.2012	0.2375	0.3192	0.3912
	$\alpha = 16°$	0.2406	0.2849	0.3623	0.4526
	$\alpha = 32°$	0.2503	0.3095	0.4086	0.4948
Solution 2	$\alpha = 0°$	0.3192	0.3601	0.4357	0.5018
	$\alpha = 8°$	0.3130	0.3803	0.4556	0.5310
	$\alpha = 16°$	0.3346	0.3920	0.4958	0.5584
	$\alpha = 32°$	0.3906	0.4703	0.5436	0.6148
Solution 3	$\alpha = 0°$	0.3461	0.3770	0.4688	0.5274
	$\alpha = 8°$	0.3374	0.3725	0.4708	0.5584
	$\alpha = 16°$	0.3522	0.4492	0.5144	0.5990
	$\alpha = 32°$	0.3882	0.4723	0.5456	0.6240
Solution 4	$\alpha = 0°$	0.3122	0.3313	0.4137	0.4758
	$\alpha = 8°$	0.2880	0.3531	0.4301	0.5138
	$\alpha = 16°$	0.3177	0.3966	0.4610	0.5560
	$\alpha = 32°$	0.3402	0.4281	0.4963	0.5982
Solution 5	$\alpha = 0°$	0.2086	0.1877	0.3277	0.3963
	$\alpha = 8°$	0.1890	0.2839	0.3574	0.4371
	$\alpha = 16°$	0.2436	0.3192	0.3908	0.4800
	$\alpha = 32°$	0.1888	0.3300	0.4328	0.5268

Pixel intensities at different orientations and distances.

These figures allow comparison between the different concentrations at fixed distances or orientations.

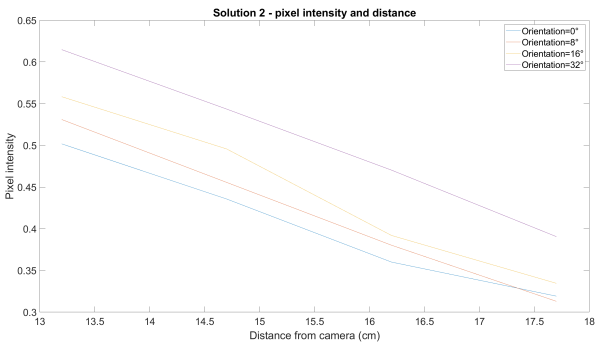

FIGURE A1: The pixel intensity using solution 2 *For different orientations at different distances from the camera.*

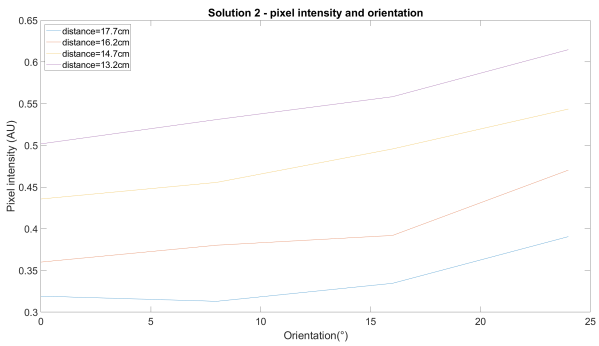

FIGURE A2: The pixel intensity using solution 2 *For different distances from the camera at different orientations.*

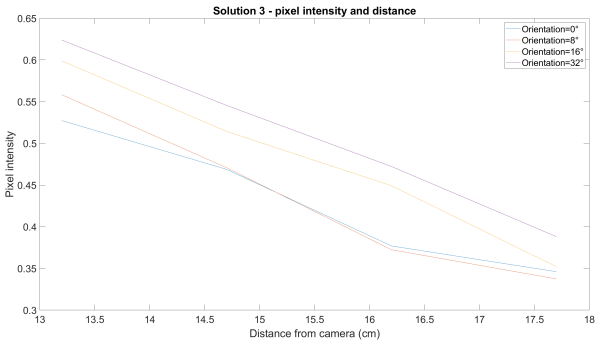

FIGURE A3: The pixel intensity using solution 3 *For different orientations at different distances from the camera.*

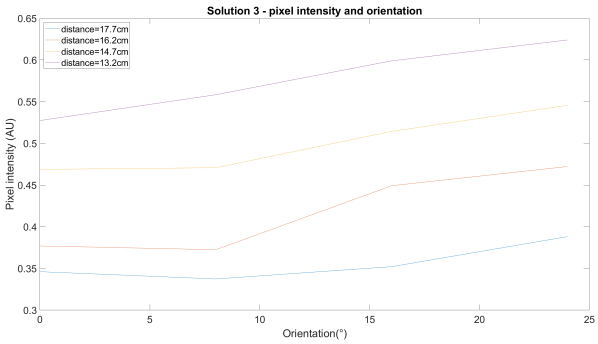

FIGURE A4: The pixel intensity using solution 3 *For different distances from the camera at different orientations.*

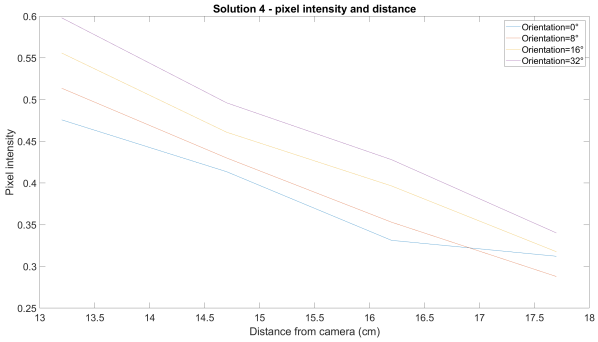

FIGURE A5: The pixel intensity using solution 4 *For different orientations at different distances from the camera.*

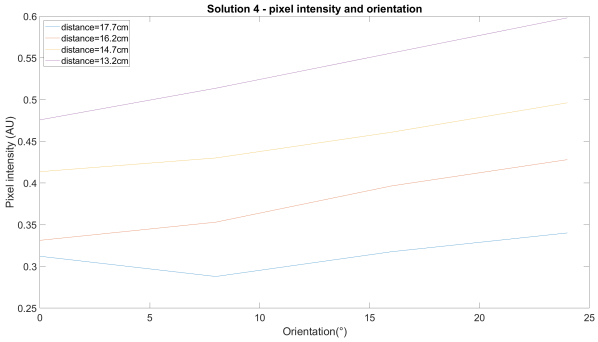

FIGURE A6: The pixel intensity using solution 4 *For different distances from the camera at different orientations.*

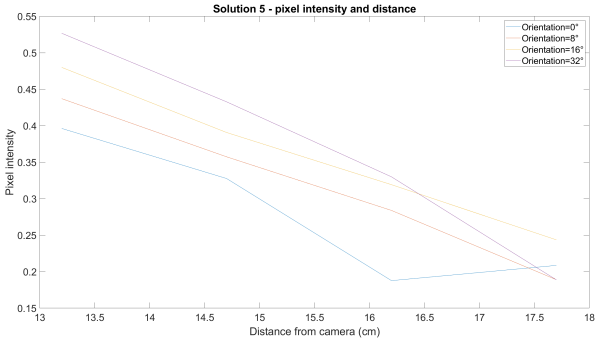

FIGURE A7: The pixel intensity using solution 5 *For different orientations at different distances from the camera.*

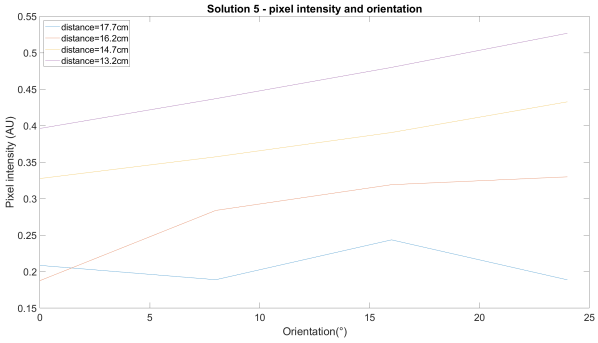

FIGURE A8: The pixel intensity using solution 5 *For different distances from the camera at different orientations*

The inverse-square law

This table shows the results of the inverse-square law. The values were calculated to investigate the way the firefly Xi holds true to this law.

TABLE A3: The inverse-square law applied for the intensities found for solutions 2, 3, 4, and 5
The estimated values were calculated using the inverse-square law.

		Measured pixel intensity (AU)	**Estimated pixel intensity (AU)**	**Difference (%)**
Solution 2	Distance = 17.7cm	0.3192	-	-
	Distance = 16.2cm	0.3601	0.3810	-5.825
	Distance = 14.7cm	0.4357	0.4628	-6.206
	Distance = 13.2cm	0.5018	0.5739	-14.46
Solution 3	Distance = 17.7cm	0.3461	-	-
	Distance = 16.2cm	0.3770	0.4132	-9.605
	Distance = 14.7cm	0.4688	0.5018	-7.040
	Distance = 13.2cm	0.5274	0.6224	-18.01
Solution 4	Distance = 17.7cm	0.3122	-	-
	Distance = 16.2cm	0.3313	0.3727	-12.49
	Distance = 14.7cm	0.4137	0.4527	-9.435
	Distance = 13.2cm	0.4758	0.5614	-17.99
Solution 5	Distance = 17.7cm	0.2086	-	-
	Distance = 16.2cm	0.1877	0.2490	-32.64
	Distance = 14.7cm	0.3277	0.3024	7.704
	Distance = 13.2cm	0.3963	0.3751	5.3616

Comparison of the different concentrations

These figures allow comparison between the different concentrations at set distances or orientations.

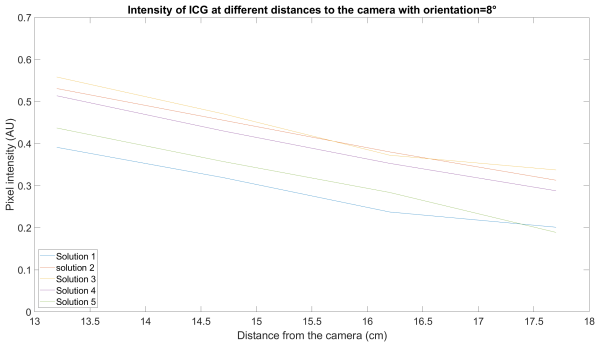

FIGURE A9: The pixel intensity for all solutions at $\alpha = 8°$

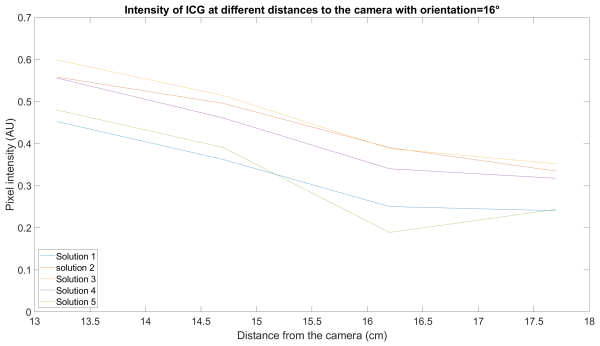

FIGURE A10: The pixel intensity for all solutions at $\alpha = 16°$

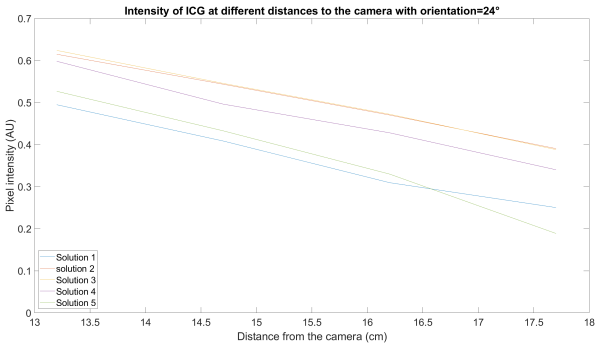

FIGURE A11: The pixel intensity for all solutions at $\alpha = 24°$

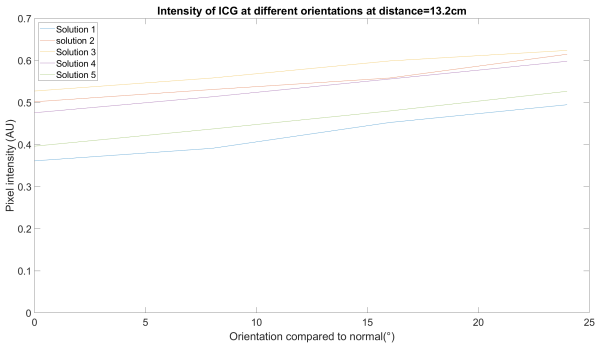

FIGURE A12: The pixel intensity for all solutions at d=13.2cm

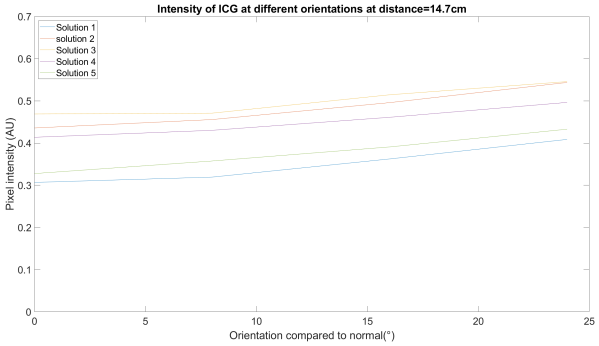

FIGURE A13: The pixel intensity for all solutions at d=14.7cm

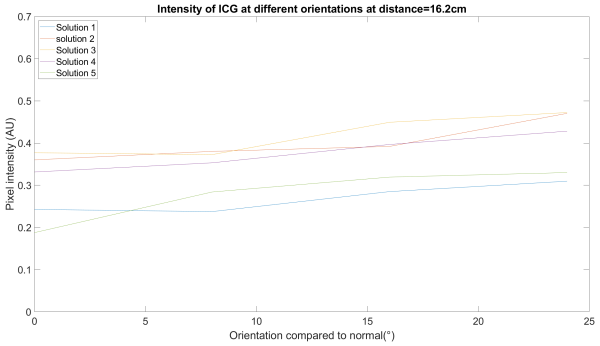

FIGURE A14: The pixel intensity for all solutions at d=16.2cm

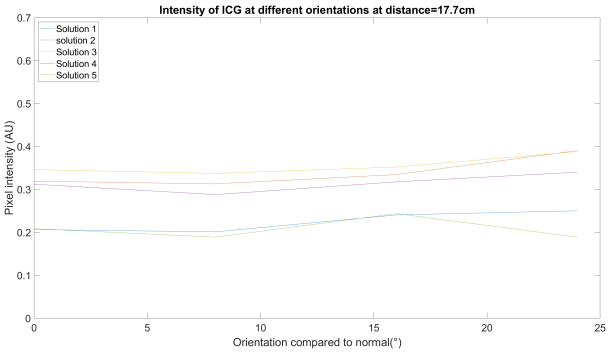

FIGURE A15: The pixel intensity for all solutions at d=17.7cm

The linear fittings

The figures in this section show the linear fitting of the different solutions and the orientation or distance. When looking at the distance the orientation was 0° and when looking at the orientation the distance was the furthest from the camera; 17.7cm.

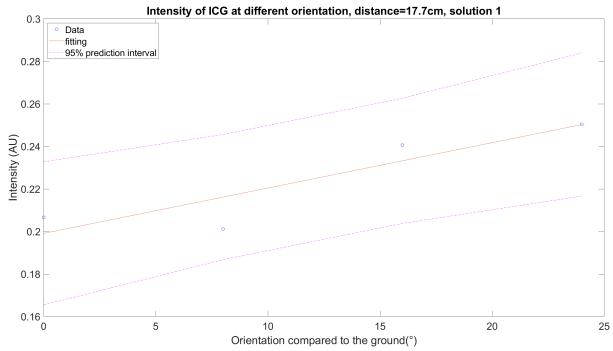

FIGURE A16: The linear fitting for solution 1 at a fixed distance and different orientations
This figure shows the linear fitting including the 95%confidence interval of the pixel intensity related to the orientation at a stable distance the mse was 0.0002499

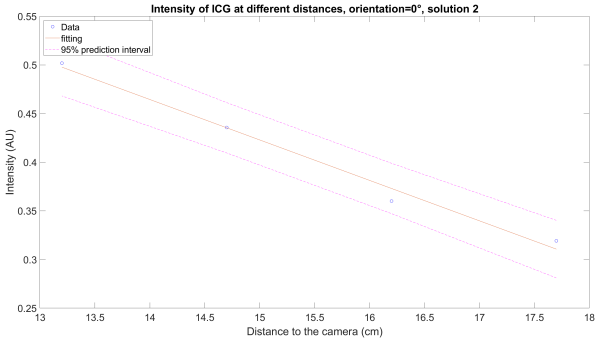

FIGURE A17: The linear fitting for solution 2 at a fixed orientation and different distances
This figure shows the linear fitting including the 95%confidence interval of the pixel intensity related to the distance at a stable orientation, the mse was 0.0001932

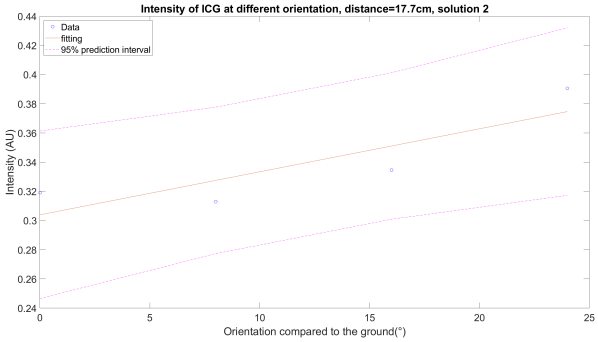

FIGURE A18: The linear fitting for solution 2 at a fixed distance and different orientations
This figure shows the linear fitting including the 95%confidence interval of the pixel intensity related to the orientation at a stable distance the mse was 0.0007266

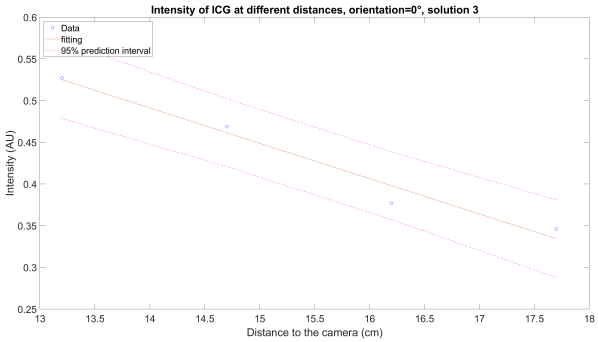

FIGURE A19: The linear fitting for solution 3 at a fixed orientation and different distances
This figure shows the linear fitting including the 95%confidence interval of the pixel intensity related to the distance at a stable orientation, the mse was 0.0004771

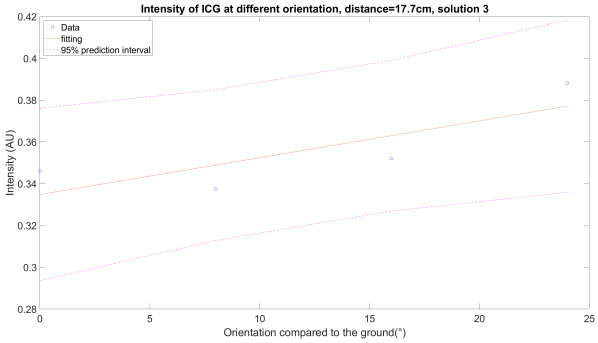

FIGURE A20: The linear fitting for solution 3 at a fixed distance and different orientations
This figure shows the linear fitting including the 95%confidence interval of the pixel intensity related to the orientation at a stable distance, the mse was 0.0003752

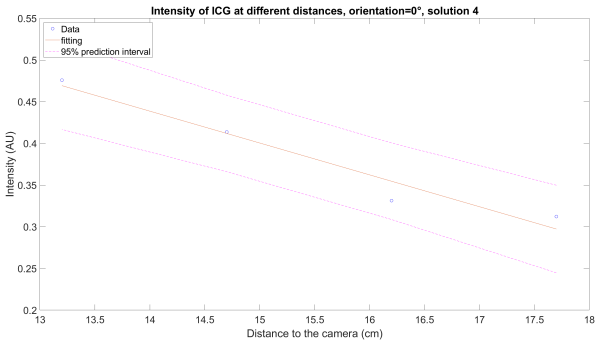

FIGURE A21: The linear fitting for solution 4 at a fixed orientation and different distances
This figure shows the linear fitting including the 95%confidence interval of the pixel intensity related to the distance at a stable orientation, the mse was 0.0006081

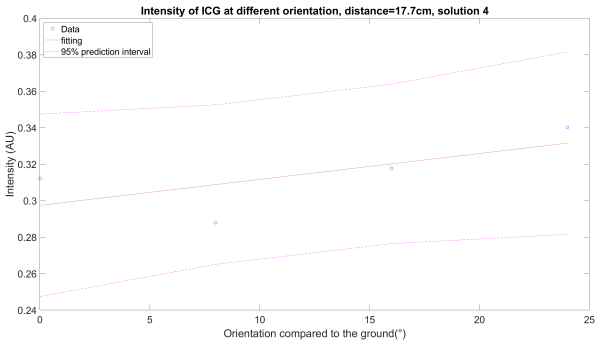

FIGURE A22: The linear fitting for solution 4 at a fixed distance and different orientations
This figure shows the linear fitting including the 95%confidence interval of the pixel intensity related to the orientation at a stable distance, the mse was 0.0005541

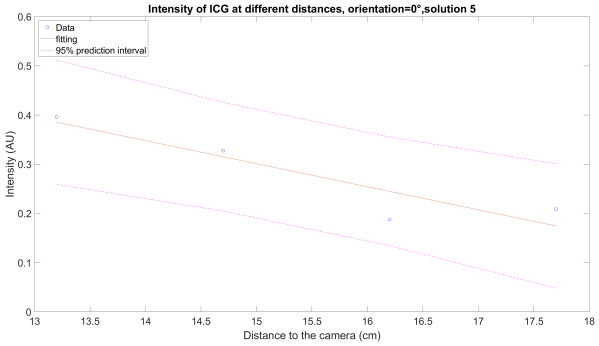

FIGURE A23: The linear fitting for solution 5 at a fixed orientation and different distances
This figure shows the linear fitting including the 95%confidence interval of the pixel intensity related to the distance at a stable orientation, the mse was 0.003522

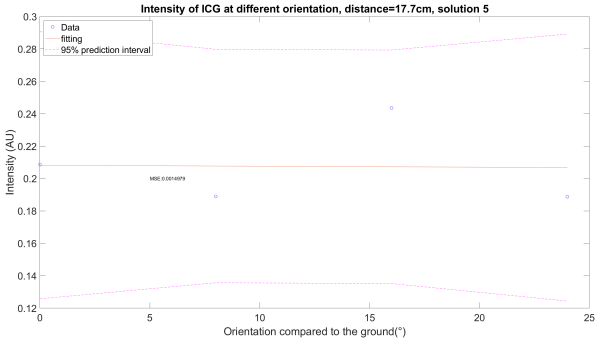

FIGURE A24: The linear fitting for solution 5 at a fixed distance and different orientations
This figure shows the linear fitting including the 95%confidence interval of the pixel intensity related to the orientation at a stable distance, the mse was 0.001498